^{108}Sn studied with intermediate-energy Coulomb excitation

Dissertation zur Erlangung des Grades
"Doktor
der Naturwissenschaften"

am Fachbereich Physik
der Johannes Gutenberg-Universität
in Mainz

Leontina Adriana Banu
born in Zimnicea, Romania
Mainz, den 2005

Tag der mündlichen Prüfung: 21.07.2005

Abstract

In this doctoral thesis the unstable neutron-deficient ^{108}Sn isotope has been studied in inverse kinematics by intermediate-energy Coulomb excitation. Previously the method has been applied to measure the energy of the first excited 2^+ state and its E2 decay rate in nuclei with $Z < 30$ only, ^{108}Sn being the highest-Z nucleus studied with this method. The purpose of the in-beam gamma-spectroscopy measurement described in the thesis was to measure the unknown reduced transition probability $B(E2; 0^+_{\text{g.s.}} \rightarrow 2^+_1)$ in ^{108}Sn. The extracted B(E2) value of 0.230 (57) e^2b^2 has been determined relative to the known value in the stable ^{112}Sn isotope.

The experiment has been carried out at GSI with the newly RISING/FRS experimental set-up, developed within the framework of the RISING project. Secondary beams of interest (^{108}Sn, ^{112}Sn) at energies of around 150 MeV/nucleon impinged on a ^{197}Au target of 386 mg/cm^2 thickness. The projectile fragments were selected and identified using the fragment separator (FRS) and its associated particle detectors. The calorimeter telescope (CATE) was used behind the target for the channel selection as well as for measuring the scattering angle of the outgoing fragments. Gamma rays in coincidence with projectile residues were detected by the RISING Germanium-Cluster detectors.

At intermediate energies, Coulomb excitation is an experimental challenge because of intense atomic background radiation and relativistic Doppler effects that have to be accounted for. With respect to these challenges, the Sn isotopes having large transition energies and short lifetimes provide a new methodological benchmark.

The experimental $B(E2; 0^+_{\text{g.s.}} \rightarrow 2^+_1)$ value in ^{108}Sn, measured for the first time, is in agreement with recent large scale shell model calculations performed with realistic effective interactions, and can be understood phenomenologically within a generalized seniority scheme model. This thesis work can be considered as bringing more insight into the investigation of E2 correlation related to core polarization studied in the vicinity of ^{100}Sn.

Contents

Chapter 1

Introduction

The structure of nuclei far from β-stability is currently a key topic of research, both experimentally and theoretically. The emphasis is put on phenomena such as shell evolution, proton-neutron interaction, and changes of collective properties. A burning question in nuclear structure physics is whether the shell closures known close to the valley of stability are preserved when approaching the limits of nuclear existence. Due to the softening of the neutron potential and decoupling of neutrons from protons [Gra2003], topics like shell quenching, new shell closures and new collective modes are of main interest towards the neutron drip line. On the other hand, towards the proton drip line due to the confinement of protons by the Coulomb barrier and/or the vicinity of the $N = Z$ line, such drastic changes are not expected neither in shell structure nor in collective properties. Here phenomena like core polarization as studied in spin (M1) [Gad1997] and shape (E2) response, proton-neutron pairing and isospin-symmetry are appealing nuclear structure investigations.

Indeed, in nuclear physics the electromagnetic interaction plays a particular important role, and this is because the experimental and theoretical study of the interaction of the atomic nucleus with electromagnetic fields has been contributing more than any other phenomenon to the understanding of the structure of nuclei. There are two main reasons for that: first, the electromagnetic interaction is by far the best understood of all the four fundamental interactions (strong, electromagnetic, weak, gravitational) and second, the strength of the electromagnetic interaction is sufficiently large to cause observable effects of the charge and the current distributions in a nucleus, and yet it is weak enough compared with the strong hadronic interaction such that perturbation theory can be applied for the analysis of the observed effects. Historically, the possibility of exciting atomic nuclei by means of the electromagnetic field of impinging charged particles was realized already in the 1930s [Bie1965] in the early stages of the study of nuclear reactions. Particularly for incident energies so low that the Coulomb repulsion prevents the particles from penetrating into the nucleus, such excitation processes could be studied without interference from more complicated nuclear interactions. However, it was not before 1952 that the process was experimentally confirmed [McC1953] to be in good agreement with the semi-classical theory of K. Ter-Martirosyan [TM1952], which led to simple quantitative

expressions for the excitation cross sections by applying a classical treatment of the trajectory of the bombarding particle. Thus, the excitation cross section was derived as a function of the energy, charge, and mass of the projectile. In the following years the discovery of the process, which became known under the name *Coulomb excitation*, was developed into an important tool for the investigation of low-lying (excitation energies up to about 1 MeV) rotational and vibrational nuclear states, but later, with the use of higher bombarding energies, it became possible also to explore excitations of higher energy.
In the early Coulomb excitation experiments light ions (protons, deuterons, or α particles) were used as projectiles and the electromagnetic forces acting on the target were then so weak, that only a few nuclear states could be populated. The construction of accelerators for heavy ions opened up the possibilities of performing much more effective and complex Coulomb excitation experiments [FS1959]. Through the strong electromagnetic field from heavy projectiles the target nucleus may absorb several quanta and thus many nuclear states can be populated [Ald1966]. Such multiple Coulomb excitation processes offer a wide variety of experiments by which one may study the electromagnetic properties of nuclear states.

For a long time a principal constraint for gaining more insight into nuclear physics was the confinement of both beam and target species to the β-stability line. Over a decade back, a new era began in nuclear research with the advent of reactions induced by radioactive ion beams (RIB) [Tan1999]. This has opened the possibility of studying experimentally how the structure of nuclei evolves from the valley of stability to the nuclear driplines, where the binding energy between the nucleons vanishes. The challenge here is related to properties of the radioactive beams, which are generally several orders of magnitude less intense than stable beams and have energies of 30-300 A·MeV much above the Coulomb barrier, when prepared by in-flight separation technique [Mün1992]. The experimental method of *intermediate-energy Coulomb excitation* was developed to take advantage of these higher beam energies and to obtain nuclear structure information even with low secondary-beam intensities [Gla1998]. Intermediate-energy Coulomb excitation allows simultaneous measurements of the energy of excited bound states in nuclei with respect to the ground state and of the Coulomb-excitation cross section to excite these states. Photons emitted in-flight from the projectile residues can be easily distinguished by their Doppler broadening from γ-rays originating in the target. The measured Coulomb-excitation cross section is a direct function of the electromagnetic $E\lambda$ or $M\lambda$ matrix elements characterizing the γ transition between the ground state and an excited state. The electromagnetic field can be expanded in multipoles of either electric ($E\lambda$) or magnetic ($M\lambda$) type. The probability of emission of radiation of a given multipole is proportional to the matrix element of the multipole operator. The total decay rate per second is given by [Boh1969]

$$T(\sigma\lambda; I_i \rightarrow I_f) = \frac{8\pi(\lambda+1)}{\lambda[(2\lambda+1)!!]^2}(1+\alpha)\frac{1}{\hbar}\Big(\frac{E_\gamma}{\hbar c}\Big)^{2\lambda+1} B(\sigma\lambda; I_i \rightarrow I_f),$$

where the σ is the multipole type (electric or magnetic), λ is the multipole order, the $I_{i,f}$ are total angular momenta of initial and final nuclear states, respectively,

connected by a γ-ray of energy E_γ given in MeV, and the total internal conversion coefficient is denoted by α. The reduced transition probability

$$B(\sigma\lambda; I_i \rightarrow I_f) = \frac{1}{2I_i + 1} |\langle \psi_f \| O(\sigma\lambda) \| \psi_i \rangle|^2$$

is defined by the reduced transition matrix element between initial and final states with $\psi_{i,f}$ nuclear wavefunctions, where the $O(\sigma\lambda)$ is electromagnetic transition operator of order λ.

In the following, estimates for the electromagnetic properties of transitions between nuclear levels are presented in connection with simple nuclear models, such as the independent particle model (shell model) [Boh1969], and the rotational and vibrational models (collective models) [Boh1975]. By comparing the measured quantities (i.e., the excitation energy of an excited state or the corresponding electromagnetic transition matrix element $B(\sigma\lambda)$) with the corresponding model predictions, it is quite often possible to decide which model is closest to the nature of the nucleus under investigation. These model predictions are very useful for estimating the size of an effect to be measured in a proposed γ-ray experiment.

One of the great success of the independent particle model is the prediction of level sequences for nuclei near closed shells, in particular odd mass nuclei. Of course, most nuclei have more then one valence nucleon. In treating multivalence particle nuclei, a number of different approaches are used. In vicinity of closed shells an extension of the independent particle model that includes residual interactions among the valence nucleons has been very successful [Cas2000]. In the case of the shell model, it is often considered a coupling scheme in which each nucleon has a given total angular momentum j. The coupling of these individual j values leads to the final J for the state in question. The energy of such a state depends on the residual interactions among the nucleons in these orbits.

In the context of the shell model, the behavior of magic nuclei is fairly simple. Doubly magic nuclei (e.g., ^{48}Ca, ^{208}Pb) are especially rigid to excitation. The lowest lying states are often of negative parity, representing particle-hole excitations across major shells. Semi-magic nuclei are likewise simple. They often reflect the properties of the seniority scheme, which show the constant excitation energies and inverted parabolic behavior of $B(E2; 0^+_{\text{g.s.}} \rightarrow 2^+_1)$ values typical of this scheme (for more details see Chapters 2 and 6). As soon as we depart from magic numbers, spectra begin to change when both valence protons and valence neutrons are present. Collectivity and softness towards deformation go hand in hand as valence nucleons are added beyond closed shells. A schematic view of such a structural evolution is illustrated in Figure 1.1. A typical structural sequence is: **"shell model" (rigid spherical) → vibrator → transitional → rotor.**

What is typical for nuclei in the vicinity of closed shells is that all have 0^+ ground states, first excited levels with $J^\pi = 2^+$, and mostly even-parity low-lying excitations. In particular for semi-magic nuclei, they show two interesting features: relatively high-lying first excited states and a compression of positive-parity energy levels as J increases. Both features contrast with "collective" nuclei characteristics.

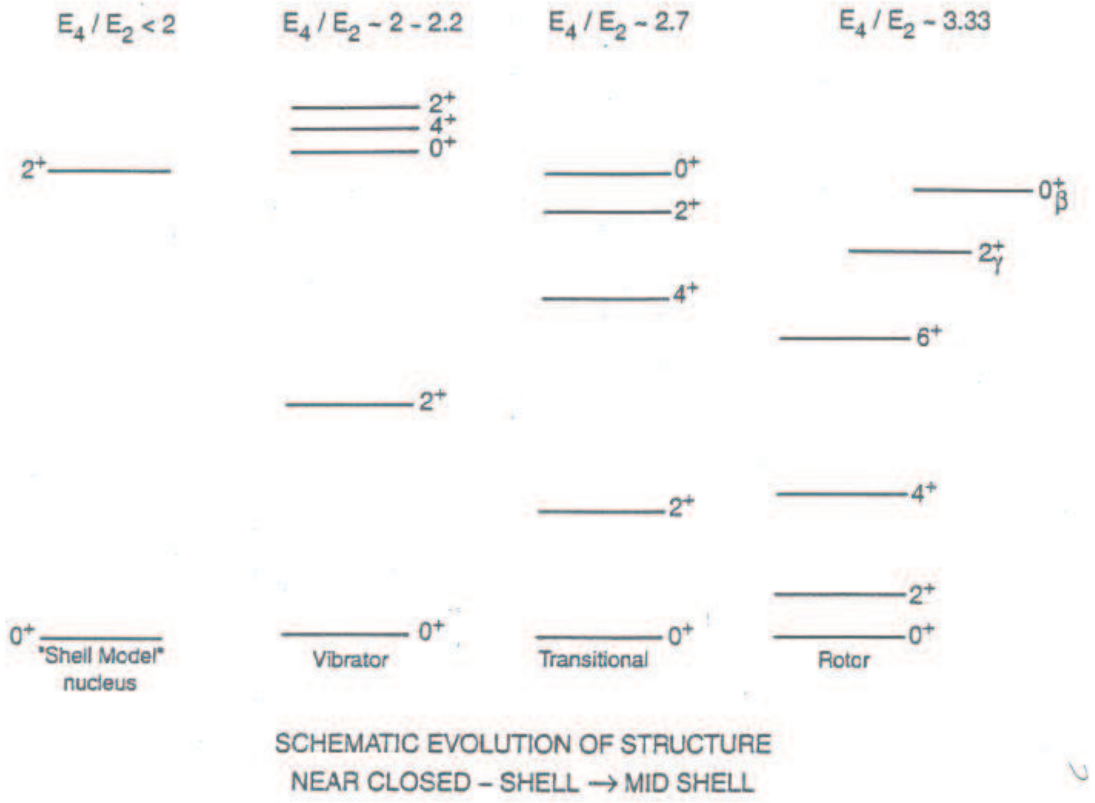

Figure 1.1: A typical sequence of level and nuclear structures types from a near closed shell region to a well deformed midshell nucleus [Cas2000].

These features persist in the Sn isotopes even when there are many valence neutrons. In nuclei far from closed shells where the shell model is not reliable, other theoretical frameworks are more appropriate. One of the most significant of these theoretical frameworks is called *geometrical* or *collective models*, which is a more macroscopic approach of assigning a specific *shape* to the nucleus and examining the rotations and vibrations of such a shape.

A more direct way to illustrate both the collective behavior of nuclei far from closed shells and the evolution of structure is to examine systematics.

Figure 1.2 shows the first excited 2^+ states in even-even nuclei throughout the periodic table. As aforementioned, near closed shells $E_{2_1^+}$ is rather high lying (typically 1 to 2 MeV), while in collective nuclei the 2_1^+ state can be described as either a vibrational or rotational excitation and occurs at much lower energy.

In Figure 1.3 it is plotted one of the most important structural signatures — the energy ratio of the energy of the 4_1^+ state to the 2_1^+ state in even-even nuclei. The absolute value of this ratio is directly meaningful, the $E_{4_1^+}/E_{2_1^+}$ tending to fall into three ranges: values below 2.0 near magic nuclei, between 2.0 and 2.4 a little fur-

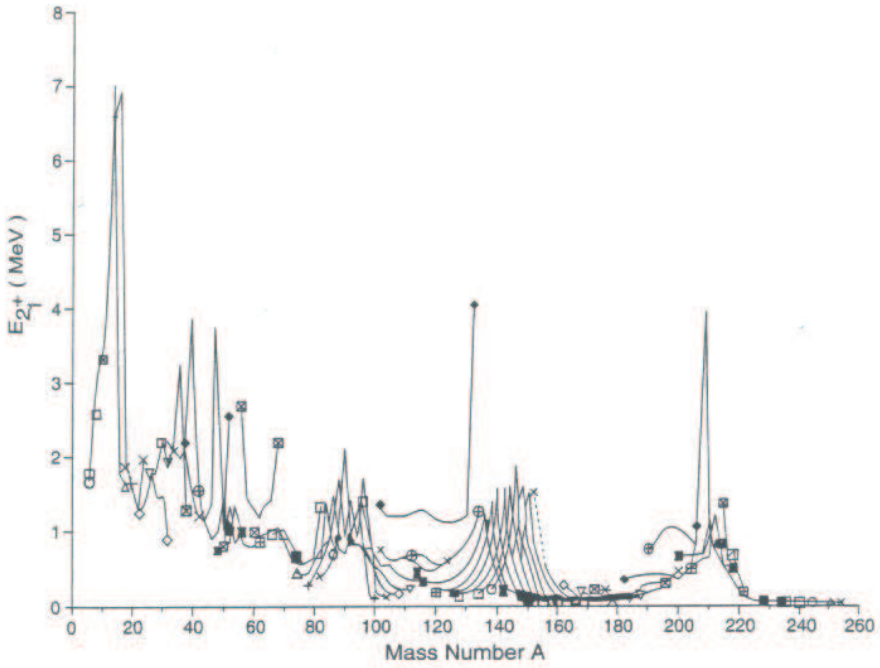

Figure 1.2: $E_{2_1^+}$ values for all even-even nuclei [Cas2000].

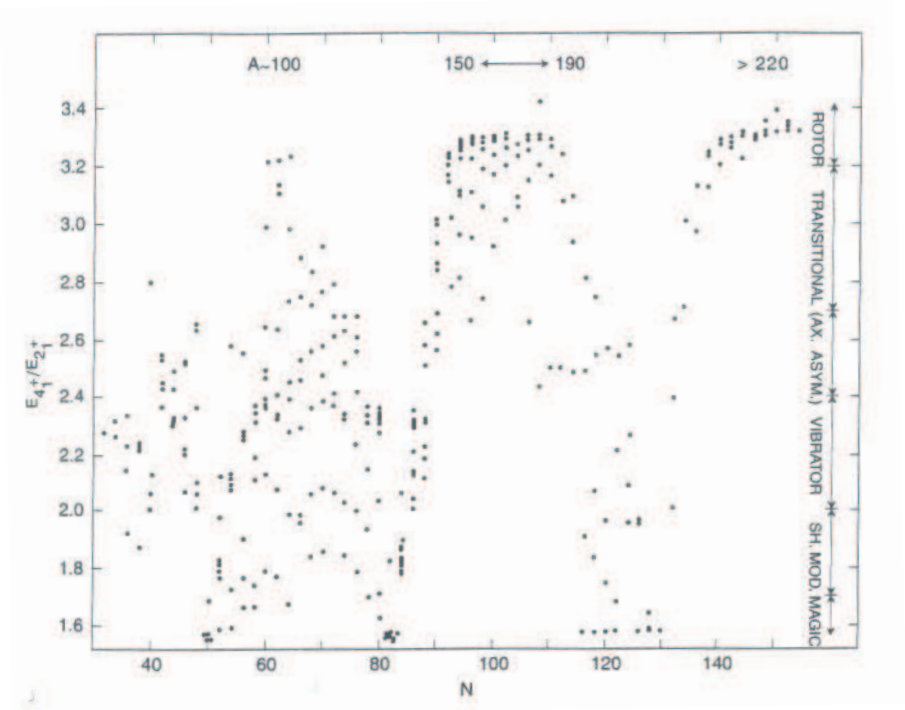

Figure 1.3: $E_{4_1^+}/E_{2_1^+}$ values plotted against N for the nuclei with $N \geq 30$ [Cas2000].

ther away from magic numbers, and values very close to 3.33 in midshell regions corresponding to rotational motion.

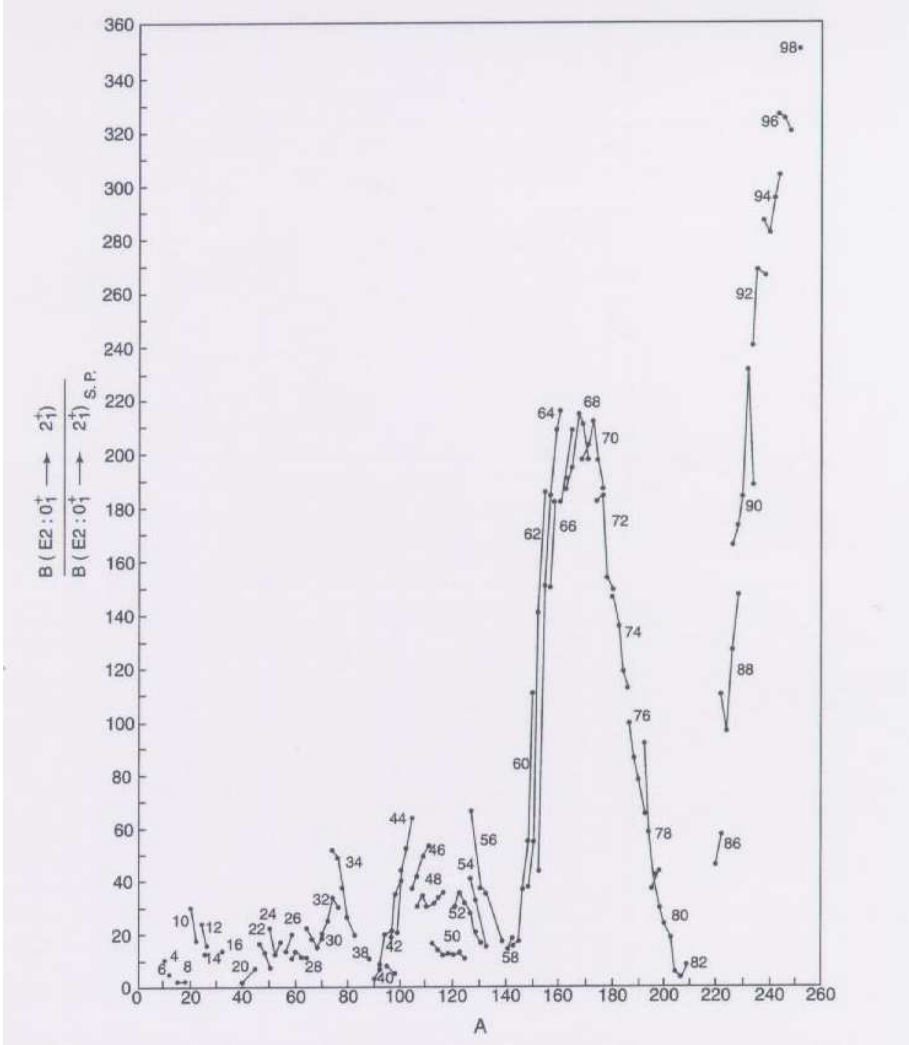

Figure 1.4: $B(E2;0_1^+ \rightarrow 2_1^+)$ values for even-even nuclei in units of a *single particle* value defined as $B(E2;0_1^+ \rightarrow 2_1^+)_{\text{s.p.}} = 0.00003A^{4/3}\text{e}^2\text{b}^2$ [Cas2000].

Figure 1.4 shows the systematics of $B(E2;0_1^+ \rightarrow 2_1^+)$ values across the nuclear chart. The typical pattern in the data is reflected by relatively small values near closed shells and enormous values in midshell regions.

Based on the nuclear systematics illustrated above, an interesting correlation between the $E_{2_1^+}$, $E_{4_1^+}/E_{2_1^+}$ and the $B(E2;2_1^+ \rightarrow 0_1^+)$ values is given in [Cas2000], as follows:

Near closed shells low values of $E_{4_1^+}/E_{2_1^+}$ correlate with low values of $B(E2;2_1^+ \rightarrow 0_1^+)$ and high values of $E_{2_1^+}$. As one proceeds through a major shell, $E_{4_1^+}/E_{2_1^+}$ rises slightly above 2 and the B(E2) values begin also to increase, while far from magic numbers $E_{2_1^+}$ drops dramatically becoming asymptotically constant, $E_{4_1^+}/E_{2_1^+}$ reaches the value of 3.33, and the B(E2) values increase rapidly towards their peak values.

Hence, a nuclear structural evolution can be characterized as evolving from spherical

nuclei near closed shells ($E_{4_1^+}/E_{2_1^+} < 2$) towards spherical, but vibrational, nuclei and culminates in a phase transition to strongly deformed nuclei with low-lying rotational states.

This doctoral thesis looks into the structural evolution of the Sn nuclei. Here the neutrons are filling the subshells between the magic numbers 50 and 82 offering thus an unique opportunity for examining how *rigid* is the doubly-magic core as valence neutrons are being added. The investigation of E2 correlations related to the core polarization effect studied in the vicinity of ^{100}Sn is the physics case of this work, which is described in detail in Chapter 2.
The tin isotope of main scope for the present work is unstable neutron-deficient ^{108}Sn, which has been studied in inverse kinematics by intermediate-energy Coulomb excitation. A presentation of the Coulomb excitation at intermediate energies is given in Chapter 3, where the process is described both theoretically and with emphasis on several experimental aspects. Detailed information about the experimental techniques applied to produce, select, identify and finally excite ^{108}Sn is provided in Chapter 4. Data analysis and the experimental result, which is the measurement of the reduced transition probability $B(E2; 0_{\text{g.s.}} \rightarrow 2_1^+)$ in ^{108}Sn, are presented in Chapter 5. The unknown *B(E2) value* was determined relative to the known value in stable ^{112}Sn, which was also measured as calibration point. The experimental result is compared with large-scale shell model calculations and theoretical interpretations are given in Chapter 6.

Chapter 2

Nuclear structure towards N = Z = 50 shell closure

2.0.1 Introductory remarks

Towards the proton drip line due to the presence of a high Coulomb barrier in atomic nuclei and the vicinity of the $N = Z$ line, changes in shell structure as well as collectivity are expected to be driven exclusively by the monopole drift [Ots2001] of single-particle states and the proton-neutron interaction between identical shell model orbitals [Naz1995]. In this respect, the heaviest $N = Z$ doubly-magic nucleus $^{100}_{50}Sn_{50}$, which is located close to the proton drip line and stable against ground-state proton decay, is a principle test ground. Information on quadrupole polarization of the magic core could be inferred from the energy of the first excited 2^+ state and its E2 transition rate to the ground state. However, although its existence has already been confirmed experimentally [Lew1994, Sch1994], the nuclear properties of this nucleus are only indirectly known from studies of its very close neighbours (for e.g., [Gor1997, Bla2004, Lip1998, Gor1998]). To gain more insight into its structure, the nuclei in its vicinity are being studied.

Between the magic numbers 50 and 82, the Sn isotopes provide the longest chain of semi-magic nuclei accessible to nuclear structure studies, both in the neutron valence space of a full major shell and with emphasis on excitations of the $Z = 50$ proton core. Thus it is possible to investigate how well the proton-shell closure is holding up as valence neutrons are being added, how collective features are developing, etc. In the previous chapter we discussed the fact that the addition of particles to the closed shells brings a breakdown of spherical symmetry, and that this leads to the existence of rotational states. However, this is not the case of the semi-magic Sn nuclei, which are considered as spherical "shell model" nuclei described fairly well by the strong paring part of the isospin $T = 1$ effective shell-model interaction [Cas2000]. Consequently, the lowest-lying excited states in semi-magic Sn isotopes are rather interpreted in terms of a broken-pair model like *generalized seniority scheme* introduced next.

2.0.2 Generalized seniority scheme

The everlasting problem in shell-model calculations for medium and heavy nuclei is the large size of the configuration spaces. Even if calculations are restricted to semi-closed shell nuclei, for which only one kind of particle is active, the dimensions of the configuration spaces are easily of the order of several millions or more for the $J = 2$ states near the middle of the shell. In order to simplify the calculation, Talmi [Sha1963] proposed a model which is a generalization of the seniority scheme — from involving only one single $j-$orbital, the model is generalized to involve a group of $j-$orbitals within a major shell.
As far back as 1943, Racah introduced for atomic spectroscopy the idea of nucleon pairing in terms of seniority quantum number. He was looking for an additional quantum number to characterize uniquely states with the same quantum numbers like S, L and J. Thus he found a way to classify states according to the number of $J = 0$ pairs, the seniority number[1] (usually denoted by ν) being the number of unpaired particles in a state of angular momentum J in a j^n configuration of like-nucleons. From such states one can construct other states with the same ν number of unpaired nucleons in j^n configurations by adding $(n - \nu)/2$ pairs. The state of a single j nucleon has $\nu = 1$ and there are states with $J = j$, $\nu = 1$ in all j^n configurations with n odd. The vacuum state has seniority $\nu = 0$ and so has the $J = 0$ state in the j^2 configuration. In all other j^n configurations with n even there are $J = 0$ states with $\nu = 0$. The discussion will not go here into more details, instead the main features of the seniority scheme will be summarized.

For any Hamiltonian which is diagonal in the seniority scheme, spacing of energy levels are independent of n. In particular, the spacing of the $\nu = 0$, $J = 0$ and $\nu = 2$, $J = 2, 4, ...$ levels in j^n configurations, for even n, are equal to those in the j^2 configuration.

An operator that changes the state of one nucleon cannot break more than one pair. Thus, the quadrupole operator whose matrix elements determine E2 transition strengths can connect the $\nu = 0$, $J = 0$ ground state only with the $\nu = 2$, $J = 2$ state and not with other $J = 2$ states with higher seniority.

The generalized seniority scheme[2] is suitable for describing semi-magic nuclei where pairing plays an important role. In particular, the Sn isotopes have been used as one of the major test cases.

In the following the concepts of pairing and seniority in Sn isotopes will be described in brief.

[1] The smallest value of n that produces a given J. Denoting this value by ν, it is clear that there can be no particles coupled in pairs to $J = 0$ in the configuration $j^\nu J$.

[2] It has been shown that the generalized seniority concept generally provides a valid truncation scheme of the full-model basis, in the sense that a calculation in a much smaller basis using the same interaction gives essentially the same excitation energies for the first few levels of each spin.

2.0.3 Pairing and seniority in Sn isotopes

A typical seniority level scheme in a j^n configuration characterizing even Sn isotopes is shown in Figure 2.1 (top panel), in the case of the $1g_{7/2}$ orbital. First of all, the only allowed J states for identical fermions in *equivalent* orbits are those with even total angular momentum $J = 0, 2, 4, ...(2j-1)$ [Cas2000]. In the ground state, all valence particles are paired to angular momentum $J = 0$ ($\nu = 0$). How one can understand the structure of excited states is illustrated in Figure 2.1 (bottom panel) in the view of a simplistic geometrical picture of the δ-function[3] as residual interaction. It can be shown that a δ-interaction in a j^n configuration is equivalent to an odd tensor interaction which is diagonal in the seniority scheme [Cas2000]. Such interactions are particulary useful for treating multiparticle configurations, since many important results can be reduced to the two-particle case.
A short presentation of the δ-interaction in $|j_1 j_2 J\rangle$ configurations is given here for the specific case of equivalent orbits $j_1 = j_2 = j$. We can write the δ-interaction as

$$V_{12} = -V_0 \delta(\mathbf{r_1} - \mathbf{r_2}).$$

Using the polar coordinates and performing angular momentum algebra calculations (see [Cas2000] for details) we obtain in a semiclassical approximation the shifts of different J states for the δ-interaction between two identical particles in equivalent orbits

$$\Delta E(j^2 J) \approx \frac{|V_0| F_R}{\pi} \tan\frac{\theta}{2} \qquad (T = 1,\ J \text{ even}),$$

where θ is the angle between the two orbits. Here it should be noted the relationship between the energy spacing and the angle θ which implies a gradual reduction of the spacing the higher the total angular momentum J of a certain excited state is. Hence, the least bound bound state in the seniority level scheme corresponds to the minimum possible[4] angle between the two equivalent orbits. This state is considered to be an isomeric state as it corresponds to the minimum energy spacing.[5] One can explain thus the existence of isomeric states in Sn isotopes. As an example, in Figure 2.2 it is plotted the level and isomeric systematics for $^{108-124}$Sn isotopes.

Within the formalism of the seniority scheme model it can be demonstated that transition probabilities are proportional to the number of pairs in the j-shell of a j^n configuration (see e.g. [Sha1963]). The collective effect is therefore most pronounced in the middle of closed shells, which are shells half-filled with particles, half-filled with holes. This is in agreement with the experimental finding that the quadrupole transition probabilities for nuclei in the middle of closed shells are enhanced with respect to their pure shell model values. For nuclei between closed shells, the energetically most favoured configuration will be the one in which all nucleons are

[3] The reason for choosing a δ-function residual interaction is not only because is mathematically simple to deal with but it also has the short-range character of a nuclear interaction.

[4] Two identical nucleons cannot be 'aligned' at 0° because of the Pauli principle.

[5] An isomeric state is considered a state with a long lifetime, hence with a small γ-decay probability. Since the decay transition probability is proportional with the energy of the γ transition (as shown in Chapter 1), the smaller the decay probability, the smaller the γ-transition energy is.

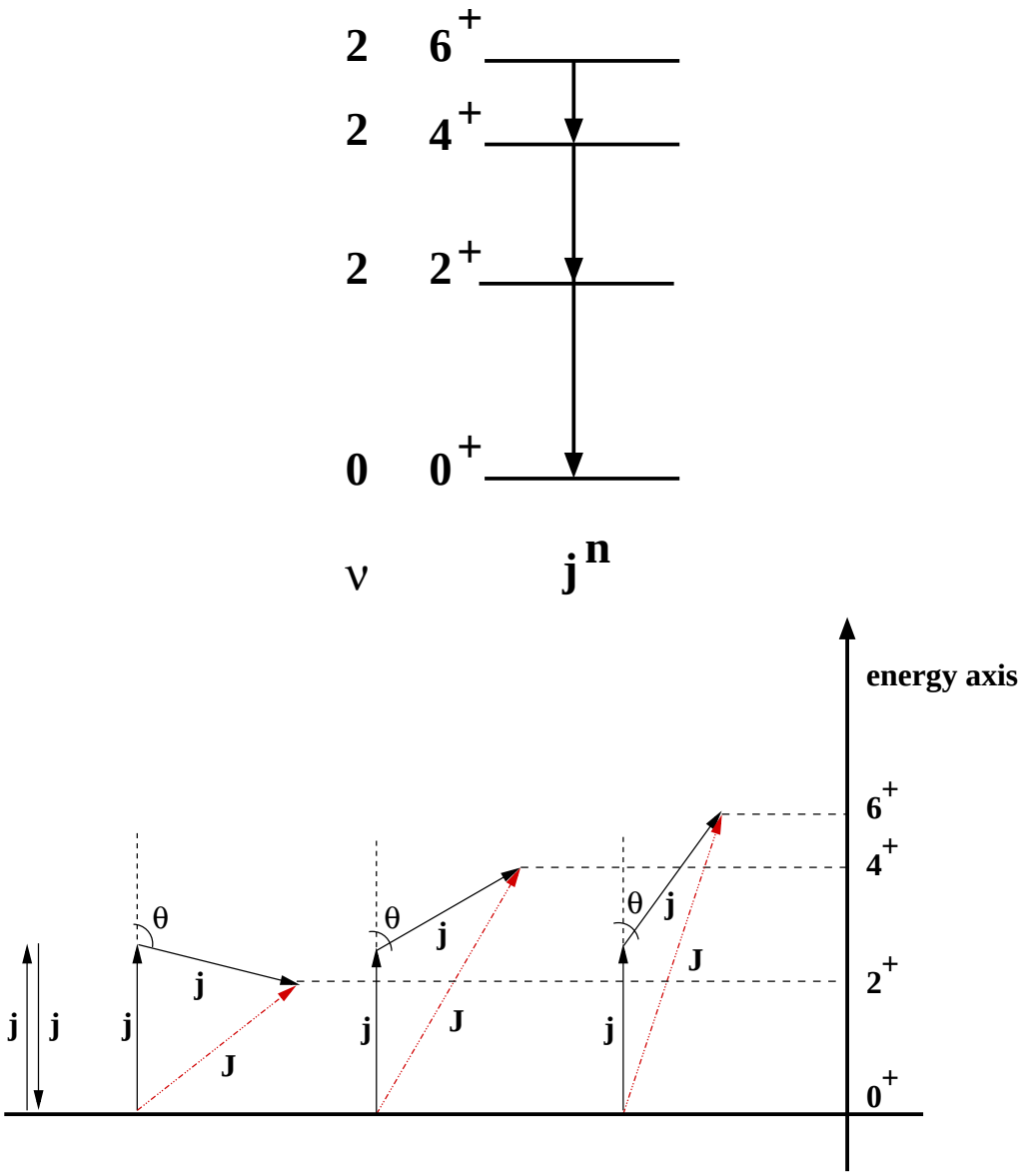

Figure 2.1: Typical seniority level scheme for even-even near closed shell nuclei in a j^n configuration with j=7/2. The ground state is interpreted as a state with nucleons paired off to seniority $\nu = 0$, while the excited states are interpreted as one broken pair configurations of seniority $\nu = 2$ (*top*). Schematic illustration in the geometrical interpretation of the short-range δ-residual interaction acting between two identical nucleons with an angular momentum j coupled to a total angular momentum J, characterizing the excited states in the seniority level scheme above (*bottom*).

paired off. To excite even-even nuclei, therefore, at least one pair has to be broken. Since the binding energy of a pair is of the order 1-2 MeV, the energy spacing between the ground and the first excited state in even-even nuclei is thus qualitatively explained (see Figure 2.2). The existence of $(J = 0)$-pairs favours a spherical nuclear shape since no direction is preferred. Nuclei in the neighbourhood of closed

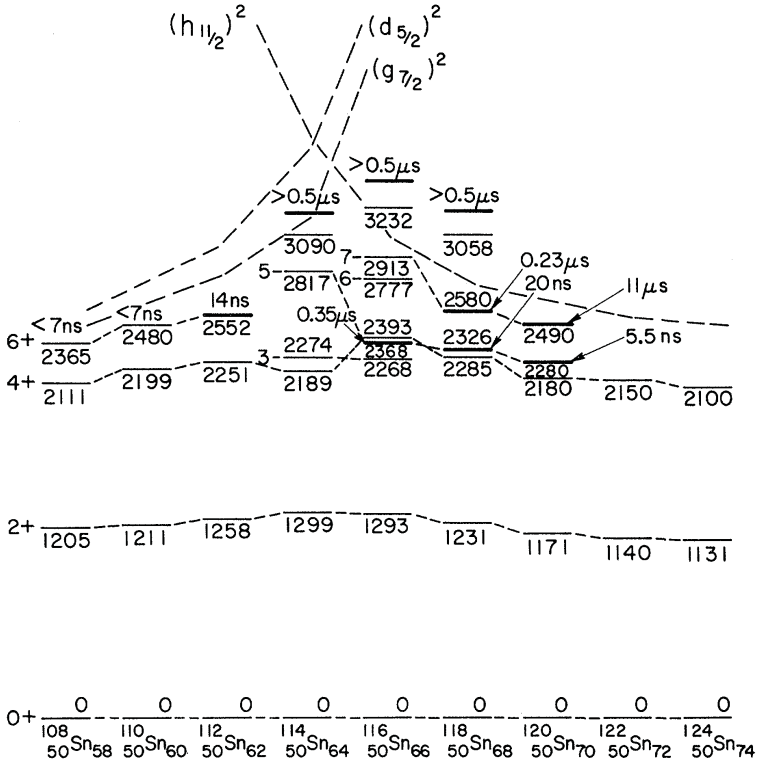

Figure 2.2: The energy level and seniority isomer systematics in $^{108-124}$Sn isotopes.

shells will therefore still have spherical symmetry, the influence of the pairing force overcoming the tendency towards deformation. Further away from the closed shells one has the opposite situation. However, this depends strongly on the strength of the pairing force versus the long-range *particle-hole* force [Cas2000]. Closely connected is the existence of low-lying 2^+ levels for open shell even-even nuclei. Nuclei in the neighbourhood of closed shells that are still spherical can easily be excited to shape vibrations around their spherical equilibrium position, since the restoring force, which is the difference between pairing and deformation effects, is rather small. The nucleus will therefore become deformed into an ellipsoid and vibrate about its spherical shape with a low quadrupole oscillation frequency.

2.0.4 Core polarization

An interesting fact about the observed quadrupole moments of odd-mass nuclei is that very often a nucleus with an odd neutron is found to have a significant quadrupole moment. Initially this was not so easy to imagine in odd-mass nuclei, where the nuclear properties are described by the valence particle, because the odd neutron is electrically neutral. The question was why the quadrupole moment, which reflects electric charge/current distributions in nuclei, has a non-zero value in this case? The answer is that the quadrupole moment must entirely arise from the protons inside the core of the odd-mass nucleus. However, the core has an even

number of protons, therefore its wavefunction has an angular momentum zero too, and hence a zero quadrupole moment. The explanation for this apparent paradox is given in [Boh1969]: the observed quadrupole moments in odd-neutron nuclei can be simply understood as a consequence of the nonspherical field generated by the extra particle. The orbit of each proton in the closed-shell core is thus slightly distorted and acquires an extra quadrupole moment, the total induced quadrupole moment being of the order

$$Q_{pol} = \frac{Z}{A} Q_{sp},$$

which roughly corresponds to the magnitude of the observed effect (Q_{sp} being the quoadrupole moment of a single proton in the core). Hence, the effect is expected to be additive in the case of configurations involving several particles outside of closed shells. This effect can be regarded as a polarization of the core protons by the valence protons or neutrons (there is no reason why such effect should not be induced by a valence proton) and is often referred to as the "core-polarization" effect[6]. In association with the core-polarization effect one speaks about an effective charge for the valence particle,

$$e_{eff} = e\Big(\frac{1}{2} + t_z\Big) + e_{pol},$$

where in the isospin notation $t_z = 1/2$ for protons and -1/2 for neutrons.
Polarization charges e_{pol} required to explain the observed transition probabilities in the vicinity of doubly-magic nuclei are generally between 0.5 and 1.5e [Lip1998].

Coming back to ^{100}Sn case, the effective charge can be related to the degree of rigidity of the spherical equilibrium shape of the closed-shell nucleus and, thus, is especially sensitive to the excitation energy and decay rate of the lowest 2^+ state of the doubly-magic core.

Figure 2.3 shows the measured reduced transition probabilities $B(E2; 2_1^+ \rightarrow 0^+_{\text{g.s.}})$ and the excitation energies of the first excited 2^+ states for the even Sn isotopes between $N = 50$ and 82 shell closures. The almost constant excitation energy of the 2_1^+ states along the whole isotopic chain is the classical example for the generalized seniority scheme aforementioned in this chapter. This indicates that the 2_1^+ states may be described as one broken pair upon a ground state condensate of 0^+ pairs. The corresponding reduced transition probability is the most sensitive to the details of shell structure and quadrupole collective effects and thus represents a relevant probe to study the E2 correlations related to core polarization especially

[6]There is a fundamental difference, both experimentally and theoretically, between the core-*polarization* effect for odd-mass nuclei, whose normal equilibrium shape is spherical, and the core-*deformation* effect of these nuclei in the rotational region. Experimentally, the latter nuclei are found to have quadrupole moments that are two orders of magnitudes larger than the single-particle value predicted theoretically. In the case of odd-mass nuclei in the spherical region, the experimental values differ appreciably from the single-particle estimate but never by two orders of magnitude.

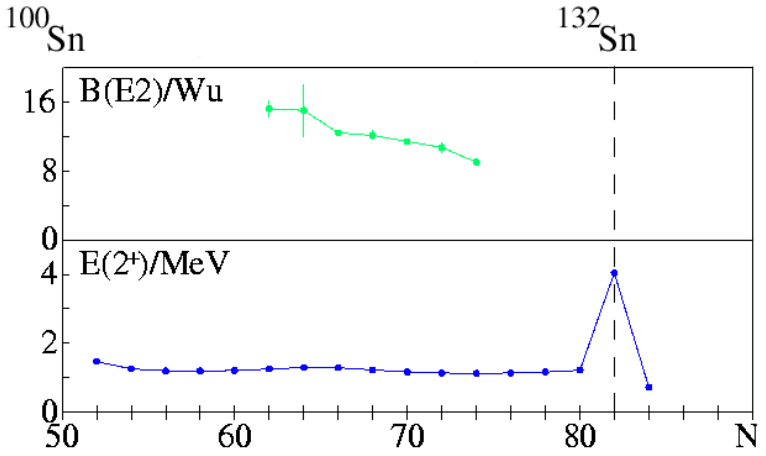

Figure 2.3: Systematics of the excitation energy of the first excited 2^+ state and the E2 strength $B(E2; 2_1^+ \rightarrow 0_{\text{g.s.}}^+)$ for the even Sn isotopes between $N = 50$ and 82 shell closures. The B(E2) values here are expressed in Weisskopf unit (W.u.), $1W.u. = (5.94 \times 10^{-6})A^{4/3}e^2b^2$.

among the light neutron-deficient tin isotopes towards ^{100}Sn. Until recently the $B(E2; 2_1^+ \rightarrow 0_{\text{g.s.}}^+)$ values were measured only in stable $^{112-124}$Sn [Ram2001].

The measurement of the $B(E2; 2_1^+ \rightarrow 0_{\text{g.s.}}^+)$ values in unstable Sn isotopes would have been almost impossible over a decade ago when a fusion-evaporation reaction mechanism has been the only possibility to produce radioactive tin isotopes. The problem with this method is that high spin yrast states are populated first. For Sn isotopes this is problematic due to the existence of higher-lying isomeric states, which hampers a direct measurement of the lifetime of the 2_1^+ states by standard methods like Doppler shift attenuation method (DSAM) or recoil distance method (RDM). The very short lifetimes of the 2_1^+ states (less than 1 ps) also make it difficult to apply electronic timing methods to measure the $B(E2; 2_1^+ \rightarrow 0_{\text{g.s.}}^+)$ values. Therefore, a Coulomb excitation measurement is the only way to obtain this important piece of nuclear structure information. With the world wide uprising radioactive beam facilities, unstable Sn isotopes can be easily produced nowadays either in projectile fragmentation reactions followed by in-flight separation or via ISOL techniques (see Chapters 3 and 4). In either case they are at the end studied in inverse kinematics with intermediate-energy Coulomb excitation in the former case or in subbarrier reactions in the latter, in order to measure the $B(E2; 2_1^+ \rightarrow 0_{\text{g.s.}}^+)$ values.

Chapter 3

Relativistic Coulomb excitation

3.1 General description

The excitation of a nucleus by means of electromagnetic interaction with another nucleus is known as *Coulomb excitation*, which is an inelastic scattering process. In the past, this process has been extensively used to study the first excited 2^+ states in even-even nuclei. Traditionally, stable targets of the nuclei to be studied are prepared and bombarded with heavy ions at energies so low that the Coulomb repulsion prevents the particles from touching the nucleus, assuring thus a pure Coulomb interaction process without nuclear contribution. However, this technique is not applicable anymore to study so-called "exotic nuclei". These are nuclei far from the valley of stability which cannot be formed into targets due to their short lifetimes. Yet such nuclei can be investigated by Coulomb excitation in *inverse kinematics* at energies below or above the Coulomb barrier depending on their production mechanism. The idea is to scatter exotic beam particles off a stable target and to detect them in coincidence with γ rays, tagging an inelastic scattering process.

The radioactive ion beams are produced nowadays by two complementary techniques [Mün1992] — chemical separation followed by postacceleration (ISOL technique) and in-flight projectile fragmentation. There are certain advantages and disadvantages that one encounters in these two approaches.
One of the advantage of using the ISOL radioactive beams for Coulomb excitation studies is, besides their high intensities, just the energy below the Coulomb barrier at which they are produced, ensuring thus that for all impact parameters the nuclear excitation is excluded.
On the contrary, the projectile fragment beams are produced at energies much above the Coulomb barrier (up to hundreds A·MeV) and with low intensities. The large secondary beam energies allow the use of very thick targets, partially offsetting the low beam intensities. However, with respect to relativistic Coulomb excitation studies, one definitely needs an impact parameter selection to discriminate between nuclear excitation contributions and Coulomb excitation. Slowing the high energy beams down to Coulomb barrier energy regimes reduces their quality and yield.

Since this work is an in-beam γ-ray spectroscopy measurement via the experimental technique of intermediate-energy Coulomb excitation, it is this mechanism that is elaborated here.

By Coulomb excitation at intermediate energies ($T \sim 100$ A·MeV) one can study low-lying energies of 2^+ excited states in exotic nuclei and correspondingly the γ-ray yields which are measures of Coulomb-excitation cross sections. The measured excitation cross sections are directly proportional to the E2 electromagnetic matrix elements that can be determined through the theory of the Coulomb excitation, as discussed next.

3.2 Theoretical description

In a collision between two heavy ions the electromagnetic interaction depends on the electromagnetic multipole moments of both nuclei, thus during the collision one or both nuclei may be excited. For a pure Coulomb excitation process, where the charge distributions of the two nuclei do not overlap at any time during the collision, the excitation cross section can be expressed in terms of the same electromagnetic multipole matrix elements characterizing the electromagnetic decay process.

In the following, the Coulomb excitation cross section is determined from a semi-classical theoretical approach.

3.2.1 Basic parameters and approximations

In the classical treatment of the Coulomb excitation process, it is a very good approximation to consider the projectile as point like charge moving along a hyperbolic orbit in the repulsive Coulomb field of a target nucleus. However, the motion of the projectile is described correctly by a wave packet moving along the orbit as illustrated in Figure 3.1.

Sommerfeld parameter

The motion of the projectile in the Coulomb field of the target nucleus is essentially characterized by the dimensionless parameter η defined by

$$\eta = \frac{a}{\lambda/2\pi} = \frac{Z_p Z_t e^2}{\hbar v_p},$$

where a[1] is half the distance of closest approach in a head-on collision, λ is the wavelength of the projectile, v_p its velocity at large distance and Z the charge number with subscripts p and t referring to projectile and target nuclei, respectively.

[1] $a = \frac{Z_p Z_t e^2}{m_0 v_p^2}$, where m_0 is the reduced mass of the projectile and the target nucleus.

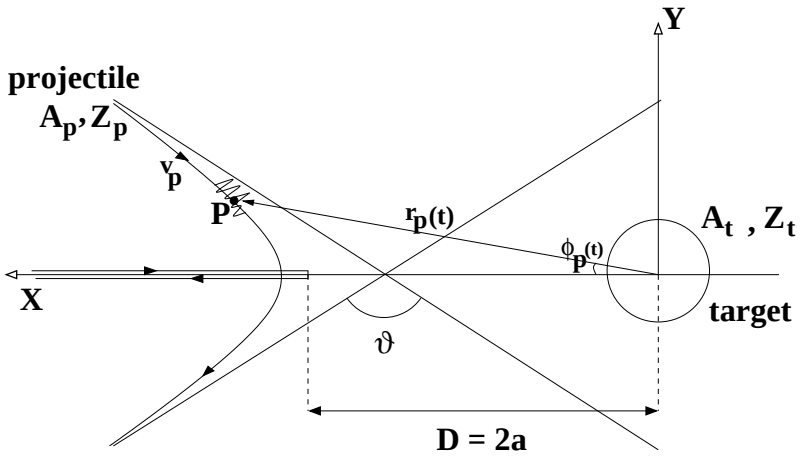

Figure 3.1: The hyperbolic orbit of the projectile P viewed as a wave packet is shown in the frame of reference in which the nuclear mass center is at rest. The position and velocity of the projectile are denoted by Φ_p, r_p, and v_p, respectively, and the deflection angle by ϑ. The distance of closest approach D is also illustrated in connection with the sketch of a head-on collision.

If the Sommerfeld parameter is significantly larger than unity,

$$\eta \gg 1,$$

one may describe the relative motion of the projectile and target nuclei in terms of wavepackets of dimensions small compared to the dimensions of the classical hyperbolic orbit, which follow the hyperbola quite accurately. In the case of ^{108,112}Sn investigated here, typical values for $\eta \approx 58$ justify the use of the semiclassical approach.

Adiabaticity parameter

The probability for Coulomb exciting a nuclear state $|f\rangle$ from an initial state $|i\rangle$ becomes larger the longer the transition time $t_{if} = \frac{\hbar}{(E_f - E_i)} = \frac{1}{w_{if}}$ is by comparison with the collision time $t_{coll} = \frac{a}{v_p}$, defined as the time during which the projectile is in the vicinity of the target. Otherwise, the nucleus responds adiabatically to the interaction. That it, the cross section for Coulomb excitation is large if the *adiabaticity parameter* satisfies the condition

$$\zeta = \frac{t_{coll}}{t_{fi}} = \omega_{if} \frac{a}{v_p} < 1.$$

At very high energies one has to take into account the relativistic contraction by means of the Lorentz factor

$$\gamma = (1 - v_p^2/c^2)^{-1/2},$$

with c being the velocity of light. In this case, the shortest distance at which the nuclei still interact electromagnetically is of the order of the sum of the nuclear radii,

$R = R_p + R_t$. Hence, in a collision with impact parameter R, the interaction time is of the order of $R/\gamma v_p$. For such a collision the adiabaticity condition becomes

$$\xi(R) = \frac{w_{fi} R}{\gamma v_p} < 1.$$

For $v_p \sim 0.5c$ and $b \sim 15$ fm, as it is the case here for ^{108,112}Sn, it follows that

$$\xi \sim \frac{\Delta E}{13 \text{ MeV}}.$$

Since ξ should be smaller than unity for excitations to occur, states in the giant resonance region with excitation energies of 10 - 20 MeV can readily be excited. Figure 3.2 shows the Coulomb excitation cross section as a function of beam energy for low-lying collective states and giant dipole and quadrupole resonance states corresponding to a ^{112}Sn projectile beam impinging on a ^{197}Au target.

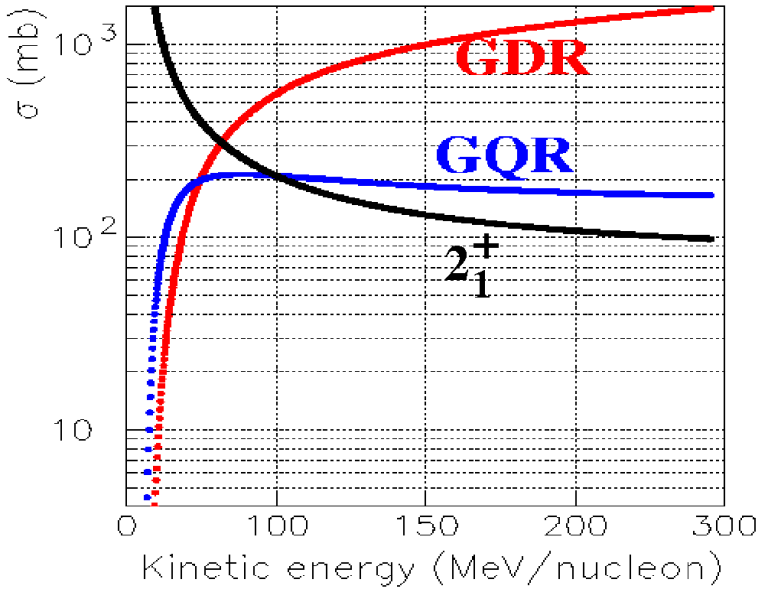

Figure 3.2: Cross sections for Coulomb excitation of the first excited state (2^+), the giant dipole resonance (GDR), and the giant quadrupole resonance (GQR) versus the beam energy, for a ^{112}Sn beam incident on a ^{197}Au target.

Straight-line approximation

In the semiclassical theory of Coulomb excitation the nuclei are assumed to follow classical trajectories. At low energies one assumes Rutherford trajectories for the relative motion, while at high energies one assumes a straight-line motion.
For the relativistic case, the projectile deflection angle in the laboratory reference frame is given by

$$\theta_{\text{lab}} = \frac{2 Z_p Z_t e^2}{\gamma m_p v_p^2} b^{-1}.$$

The straight-line motion is characterized by impact parameters equal in magnitude with the distance of closest approach at the nuclear interaction radius [Wol2005].

For ^{108,112}Sn studied here, that is $Z_p = 50$, $Z_t = 79$, $\gamma \approx 1.2$, $v_p \approx 0.5c$, $m_p \backsimeq A_p u$, and $b \sim 15$ fm, small defection angles as $\approx 2^\circ$ are obtained. Hence, the assumption of a straight-line trajectory is justified.

3.2.2 Coulomb excitation cross section

In this section, the theoretical calculation of the relativistic electromagnetic excitation is outlined. There are several theoretical papers on relativistic excitation which the reader is referred to for a further detailed description of the process, [Ald1975], [Win1979], [Ber1988], [Ale1989], just to mention a few of them.

In the following we shall only consider excitation of the target nucleus. However, the excitation of the projectile is entirely analogous to the excitation of the target apart from the magnitudes of the exciting fields, which are proportional to Z_t and Z_p, respectively.

As a starting point, in the theory of relativistic Coulomb excitation recoil effects on the trajectory are neglected (one assumes straight-line motion), so that the nuclear center of mass may be taken as the fixed origin of the coordinate system. Furthermore, the energy loss of the projectile is small compared to the bombarding energy, thus the effect of the excitation on the particle motion can be neglected, too. In such a treatment, the nuclear excitation is a result of the time dependent electromagnetic field of the projectile acting on the target nucleus. If the effect of this field is small, it may be treated by first-order quantum-mechanical perturbation theory.

In a semiclassical treatment, the differential elastic scattering cross section is given by the Rutherford formula

$$\frac{d\sigma_R}{d\Omega} = \frac{1}{4} a^2 \sin^{-4}(\vartheta/2),$$

where ϑ is the scattering angle in the center-of-mass system and a half the distance of closest approach in a head-on collision, aforementioned.
Since it has been assumed that the orbit of the particle is not appreciably affected by the excitation, the differential excitation cross section is given by

$$\frac{d\sigma_{i\to f}}{d\Omega} = \frac{d\sigma_{Ruth}}{d\Omega} P_{i\to f},$$

where $\mathrm{P}_{i\to f}$ is the probability that the target nucleus is excited in a collision in which the particle is scattered into the solid angle $\mathrm{d}\Omega$.
One may evaluate $\mathrm{P}_{i\to f}$ in the perturbation theory,

$$P_{i\to f} = (2I_i + 1)^{-1} \sum_{M_i M_f} |a_{i\to f}|^2,$$

with the excitation amplitude

$$a_{i\to f} = \frac{1}{i\hbar}\int_{-\infty}^{\infty} dt e^{i\omega_{fi}t}\langle f|V(\mathbf{r}(t))|i\rangle,$$

where I_i is the spin of the initial nuclear state and M_i, M_f are the magnetic quantum numbers of the initial and final states.

Cross section

From the excitation amplitude derived in Appendix A, one finds the following total cross section for exciting the nuclear state of spin I_f in collisions with impact parameters larger than R,

$$\begin{aligned}\sigma_{i\to f} &= 2\pi\int_R^\infty \rho d\rho (2I_i+1)^{-1}\sum_{M_iM_f}|a_{i\to f}|^2 \\ &= \Big(\frac{Z_p e^2}{\hbar c}\Big)^2 \sum_{\lambda\mu} k^{2(\lambda-1)}(B_t(E\lambda, I_i\to I_f)/e^2)\Big|G_{\lambda\mu}\Big(\frac{c}{v_p}\Big)\Big|^2 g_\mu(\xi(R)),\end{aligned}$$

where

$$B_t(E\lambda, I_i\to I_f) = \sum_{M_f\mu}|\langle I_fM_f|M_2(\lambda\mu)|I_fM_f\rangle|^2$$

is the reduced transition probability and g_μ is defined by

$$g_\mu(\xi(R)) = 2\pi\Big(\frac{\omega}{v_p\gamma}\Big)^2\int_R^\infty \rho d\rho |K_\mu(\xi(\rho))|^2 = 2\pi\int_\xi^\infty |K_\mu(x)|^2 x dx.$$

This integral can be evaluated in terms of modified Bessel functions ($\mu \geq 0$)

$$g_\mu(\xi) = g_{-\mu}(\xi) = \pi\xi^2\Big[|K_{\mu+1}(\xi)|^2 - K_\mu(\xi)|^2 - \frac{2\mu}{\xi}K_{\mu+1}(\xi)K_\mu(\xi)\Big].$$

Details about a full calculation of the total target Coulomb excitation cross section one finds in [Win1979]. Here only the final expression is given,

$$\sigma_{i\to f} = \sum_\lambda \sigma_\lambda,$$

with

$$\sigma_\lambda = \Big(\frac{Z_p e^2}{\hbar c}\Big)^2 \frac{B_t(E\lambda, I_i\to I_f)}{e^2R^{2\lambda}}\pi R^2 \frac{8\pi(2\lambda)!}{\lambda^2(\lambda-1)[(2\lambda+1)!!]^2} \qquad \text{for } \lambda \geq 2$$

The cross section for projectile excitation is given by the same formula with $B_t(E\lambda, I_i\to I_f)$ substituted by $B_p(E\lambda, I_i\to I_f)$ and Z_p by Z_t.

This result highlights the kind of proportionality relationship existing between the cross section and the reduced transition probability,

$$\sigma_{i\to f} \sim B(E\lambda, I_i\to I_f),$$

which can be exploited experimentally to extract directly basic nuclear structure information.

3.3 Experimental considerations

An accurate measurement of pure Coulomb excitation cross section requires that the collision process must be free of nuclear force. At intermediate energies, the nuclear contribution cannot be avoided. In this case, the easiest way to ensure the dominance of Coulomb excitation as compared to nuclear excitation is to limit the scattering angle of the residue projectiles to small angles. This means that only events are considered in which the impact parameter is larger than a certain minimum distance defined by the maximum scattering angle. It was shown in the previous section that straight-line trajectories are a good approximation, and therefore the distance of closest approach is nearly equal to the impact parameter. The later has to be larger than the sum of the two nuclear radii plus 2-4 fm [Ben1989] to ensure the dominance of Coulomb excitation,

$$D \approx b \leq R_t + R_p + \Delta_s \text{ with } \Delta_s \sim 2 - 4 \text{ fm}.$$

The nuclear radii can be estimated as $R = 1.25 \text{ fm} A^{1/3}$, where A is the mass number of the nucleus. A minimum distance can be ensured experimentally by limiting the scattering angle of the projectile to be below a certain maximum scattering angle,

$$\theta \leq \theta_{max} \;\Rightarrow\; b \geq b_{min}(\theta_{max}).$$

Above it was discussed how one can experimentally assure in the intermediate energy regime that the electromagnetic process is the dominant excitation mechanism. In the following we shall focus on few aspects of the electromagnetic process itself.

Measuring the Coulomb excitation cross section by counting de-excitation γ-rays requires also precise knowledge of the γ angular[2] correlations and distributions. The excitation process does not populate the magnetic substates of the excited state evenly. The population of magnetic substates depends on the multipolarity λ of the γ transition, the minimum impact parameter b_{min} and the beam energy. Hence, the angular distribution of emitted photons will be *anisotropic*. In order to determine the γ detection efficiency, which is required in a Coulomb excitation cross section measurement, the anisotropy of the γ angular distribution has to be accounted for. The general formula for the γ-ray angular distribution is given by [Mat1974]

$$W(\theta_\gamma) = \sum_k A_k P_k(cos\theta_\gamma),$$

where $W(\theta_\gamma)$ is the γ-ray intensity measured at the angle θ_γ between the direction of the incident beam and the γ quantum, k are even numbers less than or equal to $2l$ (l-photon angular momentum), $P_k(cos\theta_\gamma)$ are Legendre polynomials, and A_k are the angular distribution coefficients depending on the substate or m-population

[2]Usually one refers to a γ-ray experiment performed in coincidence with one or more of the reaction products as a γ-ray *angular correlation* measurement in contrast to a γ-ray *angular distribution* measurement in case the γ-rays are detected without any coincidence requirement.

distribution and the values of the initial and final state spins.
The γ angular correlation measured in the laboratory frame (lab) is a convolution of the intrinsic angular distribution of the photons in the projectile frame (Rest) and the Lorentz boost from the projectile frame into the laboratory frame. Hence, what one actually measures in a Coulomb excitation experiment is the double differential cross section obtained as a product between the particle (p) differential Rutherford scattering cross section (Ruth) and the particle-γ angular correlation distribution,

$$\frac{d^2\sigma}{d\Omega_p^{lab} d\Omega_\gamma^{lab}} = \frac{d\sigma_{Ruth}}{d\Omega_p^{cm}} \frac{d\Omega_p^{cm}}{d\Omega_p^{lab}} \times \frac{dW_{(\gamma_{f\rightarrow i})}}{d\Omega_\gamma^{Rest}} \frac{d\Omega_\gamma^{Rest}}{d\Omega_\gamma^{lab}}.$$

For heavy-ion collisions at bombarding energies above 100 A·MeV, as was discussed in the previous section in regard to the adiabaticity parameter, states in the giant resonance region with excitation energies of 10-20 MeV can readily be excited. In this connection is the so-called *feeding* pattern, which implies a possible de-excitation of those high-lying excited states to the ground state via the first excited 2^+ state contributing thus to the strength of the 2^+ state. This is an important issue for the measurement of the $B(E2; 0^+_{\text{g.s.}} \rightarrow 2^+_1)$ value that one should take into account and correct it for. To tag such a multi-step de-excitation process, $\gamma - \gamma$ coincidences with considerable statistics are required.

In general, an absolute cross section measurement is a challenge because every experimental detail matters, and therefore needs to be known precisely.
In the case of the experiment presented in this thesis, the reduced transition probability of the first excited 2^+ state in the unstable neutron-deficient ^{108}Sn isotope could have been determined directly from an absolute measurement of the Coulomb excitation cross section. Thus effects such as nuclear excitation, particle-γ angular correlations or feeding contributions from higher-lying 2^+ states would have to be considered. As it will be revealed at length later on in this work, due to limited statistics these pieces of information were not available for the data analysis. Therefore here it is discussed the experimental result of a relative measurement of the $B(E2; 0^+_{\text{g.s.}} \rightarrow 2^+_1)$ value in ^{108}Sn. The stable ^{112}Sn isotope with a known $B(E2; 0^+_{\text{g.s.}} \rightarrow 2^+_1)$ value [Ram2001] was also measured with Coulomb excitation at intermediate energy as to calibrate the measurement on the isotope of interest, ^{108}Sn. A relative measurement is justified in our case since the two Coulomb excitation measurements were performed under similar experimental conditions (see Section 4.9). The unknown feeding pattern is thus cancelled out (assuming similar nuclear structure in both ^{108}Sn and ^{112}Sn), as well as the remaining nuclear contribution not removed by the scattering angle condition.

Chapter 4

The experiment

4.1 Overview

In this chapter, the first relativistic Coulomb excitation experiment performed on the ^{108,112}Sn isotopes is discussed. The experiment was carried out at GSI with the newly RISING/FRS experimental set-up, developed within the framework of the RISING project [Wol2005]. Secondary beams of interest (^{108,112}Sn isotopes) at energies of around 150 A·MeV impinged on a gold target of 386 mg/cm^2 thickness. The radioactive ^{108}Sn and the stable ^{112}Sn fragments were selected and identified using the fragment separator (FRS) and its associated particle detectors. The calorimeter telescope (CATE) was used behind the target for the channel selection as well as for measuring the scattering angle of the outgoing fragments. Gamma rays in coincidence with projectile residues were detected by the RISING Ge-Cluster detectors. In Figure 4.1 the experimental set-up is shown.

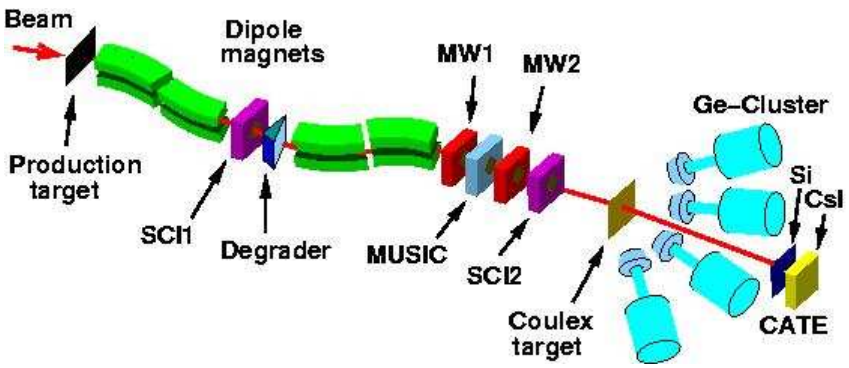

Figure 4.1: Schematic layout of the RISING set-up at the fragment separator (FRS). The particle detector set-up consists of two multiwire proportional chambers (MW1 and MW2), an ionization chamber (MUSIC), two scintillation detectors (SCI1 and SCI2), and the calorimeter telescope CATE. The γ rays are measured with an array of Ge-Cluster detectors.

Coulomb excitation at relativistic energies is an experimental challenge. In the

next sections the experiment analyzed in this work is described in detail, from the production of the nuclei of interest until the detection of the photons corresponding to the γ lines of interest.

4.2 Production of radioactive beams at GSI

The accelerator facility at GSI consisting of a linear accelerator (UNILAC), a heavy ion synchrotron (SIS), and an experimental storage ring (ESR) can deliver any element among the stable nuclei from hydrogen till uranium up to an energy that varies from 1 to 4.5 A·GeV depending on the element.
Secondary beams of radioactive isotopes can be produced at SIS/FRS by fragmentation of a stable primary beam or by fission of a ^{238}U beam on a ^{9}Be or ^{208}Pb target (with typical thickness of 1-4 g/cm^2) placed at the entrance of the fragment separator FRS. The fragments separated in-flight (see Section 4.3) can be studied directly at the final focal plane of FRS.

Relativistic heavy-ion collisions exhibit a large variety of signatures which range from the electromagnetic excitation of the nucleus to its full disintegration. The beam energy, the impact parameter and the mass of the interacting ions are decisive for the excitation energy of the fragmenting nuclear system.
In the following, the two main reaction mechanisms employed at GSI for the production of secondary radioactive beams will be briefly described.

Projectile fragmentation

When heavy-ion projectiles interact with a target nucleus, depending on the actual energy of the bombarding ions and their impact parameter, different reaction regimes are possible.
At low energies ($T < 20$ A·MeV) there are several interaction processes, i.e. Coulomb scattering, transfer reaction, and fusion evaporation reaction. Reactions occurring at much higher energies ($T > 200$ A·MeV) are considered to be "pure" fragmentation [Gol1978]. In this energy regime depending on the impact parameter, projectile fragmentation occurs in the case of peripheral collisions, while multifragmentation takes place in the case of central collisions.
The "pure" projectile fragmentation is a two-step process well described by the abrasion-ablation model [Gai1991]. Figure 4.2 shows a schematic view of the two-step reaction. The overlapping areas of the target and projectile trajectories contain the nucleons that actually interact in the collision. For a given impact parameter, the nucleons which lie in the geometrical overlap are called *participants*. Outside the interacting region the nucleons are called *spectators*. After the abrasion, most of the participants leave the collision region and only the spectators remain. The target spectator is nearly at rest. The projectile spectators constitute the *prefragments* which undergo further statistical evaporation (known as "ablation") of particles, light particle clusters or fission fragments. At the end the final fragment is created

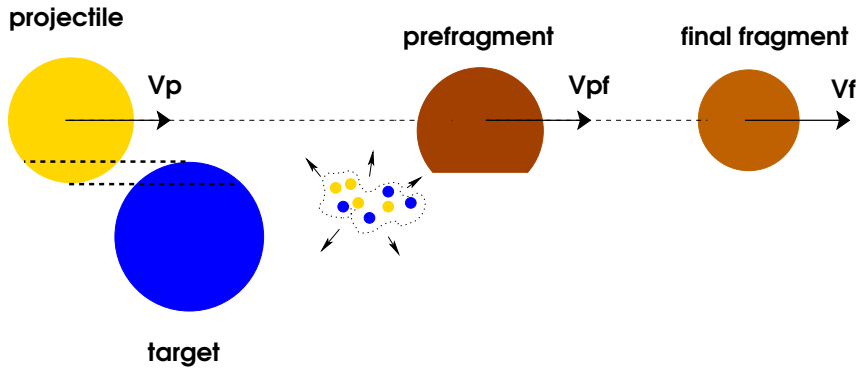

Figure 4.2: Projectile fragmentation at relativistic energies ($T > 200$ A·MeV). The overlapping interaction region is the region between the two dashed lines crossing the projectile and the target nucleus, respectively.

and moves at almost the projectile fragment velocity.

There is a feature of the fragmentation process related to the prefragment momentum distribution which is very important in designing experiments with radioactive nuclear beams.
The momentum distribution of the prefragments can be understood by a simple model introduced by Goldhaber [Gol1974] based on Fermi momentum of removed nucleons inside the projectile nucleus. Within the framework of the Goldhaber model it is shown that the dependence of the longitudinal momentum distribution on the fragment mass may be described as follows:

$$\sigma_{||}^2 = \sigma_0^2 A_F (A_P - A_F)/(A_P - 1),$$

where A_F is the fragment mass, A_P is the projectile mass, and σ_0 is the reduced width related to the Fermi momentum, with $\sigma_0 \approx 90$ MeV/c.
Several features have been experimentally observed indicating that this model is unable to account for:

- differences in widths associated with nuclides of the same mass;
- reduction of the velocity relation between fragment and projectile at low energies ($E/A < 100$ MeV);
- occurrence of an exponential tail in the fragment momentum distributions in reactions at low energies.

A new phenomenological model called "Universal parametrization" was developed by Tarasov [Tar2004], which describes fragment momentum distributions as a function of the projectile energy. The *Universal parametrization* is based on a 3-step projectile fragmentation model. Apart of the abrasion and ablation steps described earlier, the model accounts additionally for an intermediate step, *friction*, between

projectile spectator and participant. If the shape of prefragment momentum distribution is assumed to be Gaussian in the abrasion phase, an exponential attenuation characterizes the friction due to kinetic energy loss, exchange of nucleons, and transformation into the internal degrees of freedom, while in the final ablation phase of the fragmentation process model a broadening of the momentum distribution is expected.

In-flight fission

Nuclear fission is a well-known process equivalent to the disintegration of heavy nuclei near uranium into two large fragments. For secondary beam production, fission is induced by neutrons, energetic protons, or heavy ions. Recently, Coulomb fission of relativistic uranium projectile was found to play an important role in the production of exotic nuclei [Gei1995].
At relativistic energies, fission of ^{238}U projectiles in collision with Pb- or Be-nuclei occurs depending on the collision impact parameter. In the case of the U/Pb-system (see Figure 4.3) for large impact parameters ($b > R + r$), fission is induced mainly by dissociation in the electromagnetic field (interaction via the virtual photon field between the collision partners). Well above the fission-barrier, the ^{238}U nucleus excited in the domain of the giant resonances ($\sim$ 12 MeV) de-excites by emission of up to three neutrons or by fission [Aum1995]. At this low excitation energy, the ^{238}U projectile splits predominantly into a heavier and a lighter fragment, as symmetric fission is suppressed due to shell effects [Ben2002].

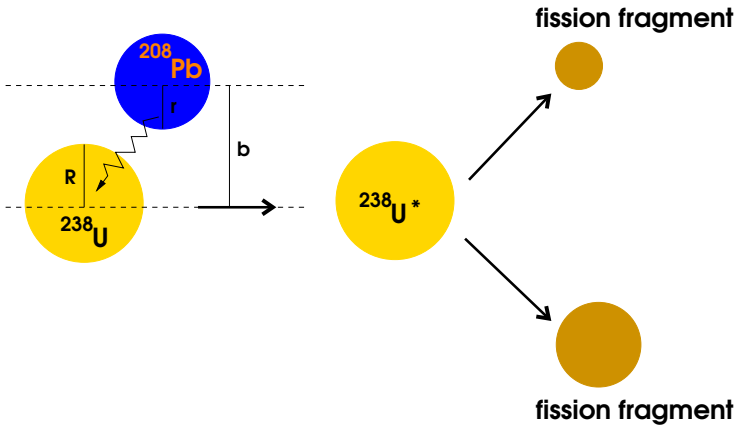

Figure 4.3: Low energy fission process induced by dissociation in the electromagnetic field for the U/Pb-system. The uranium projectile fissions into asymmetric fragments due to shell effects.

Another fission mechanism, characterizing the U/Be-system (see Figure 4.4), is the fission induced by peripheral nuclear interactions at small impact parameters ($b < R+r$). The description of such reactions can be divided into three main stages: first, the collision takes place leading to a prefragment, then thermal equilibrium is established, and finally, the resulting equilibrated system decays in a competition of

particle emission and fission. The shape of the prefragment is almost not distorted, and its mean excitation energy is given by the number of the nucleons abraded. It was found experimentally [Sch1993] that on the average 27 MeV excitation energy per nucleon abraded is induced. Thus, due to the fact that the shell effects are supposed to wash out with excitation energy [Ign1979], the prefragment fissions into two fragments of similar masses. This is the case of high-energy or symmetric fission.

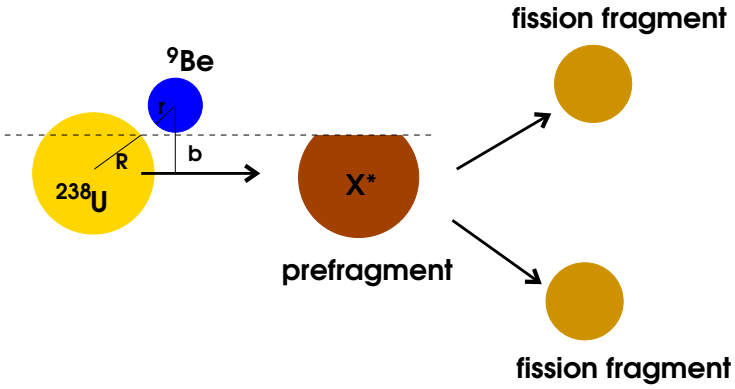

Figure 4.4: Schematic plot of the high-energy or symmetric fission induced by peripheral nuclear interactions for the U/Be-system. See text for details.

At GSI, both projectile fragmentation and in-flight fission were proved to be suitable for the production of exotic nuclei [Enq1999], depending on which part of the nuclidic chart and what properties of the exotic nuclei one wants to study. While by nuclear fragmentation of relativistic heavy ions, exotic beams are produced over the entire periodic table up to uranium, nuclear fission populates the neutron-rich side of the nuclear table as the fragments profit from the neutron excess of the heavy ions [Mün1992].

An important parameter for the physics with exotic nuclei is the yield of their production. The present maximum beam intensity from the SIS synchrotron is $\backsim 10^9$ s^{-1} for medium heavy nuclei, i.e. ^{129}Xe, and $\backsim 2 \times 10^8$ s^{-1} for ^{238}U. The intensity of particular secondary beam species can be estimated from the luminosity and the production cross section. For fragmentation reactions the production cross sections are rather well known; they are taken from the empirical EPAX parametrization based mainly on radiochemical data of proton-induced target spallation [Süm1990], [Süm2000]. For nuclear and electromagnetic fission yields experimental data are available [Ber1994], [Eng1995], [Ber1997], [Don1998], [Sch1998b], [Ben1998].

Figure 4.5 shows by comparison the cross sections for tin isotopes from fragmentation of ^{129}Xe and ^{124}Xe respectively, on a ^{27}Al target, and fission of ^{238}U on a ^{208}Pb target.

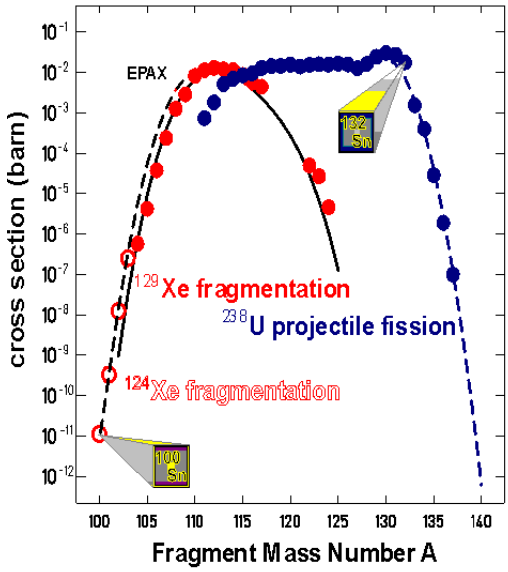

Figure 4.5: Comparison of the cross sections for tin isotopes from fragmentation of ^{129}Xe and ^{124}Xe respectively, on a ^{27}Al target, and fission of ^{238}U on a ^{208}Pb target. (Courtesy Dr. K. Sümmerer)

The exotic nuclei studied by this work are the neutron-deficient tin isotopes ^{108}Sn and ^{112}Sn. From all that was mentioned in this section, it is clear that the projectile fragmentation is the most suitable method for producing neutron-deficient nuclei, and hence producing the tin isotopes of interest. Moreover, Figure 4.5 shows that fragmentation of ^{124}Xe is the optimum choice in our case. Thus, ^{108}Sn and ^{112}Sn were produced by fragmentation reaction of a ^{124}Xe primary beam on a 4 g/cm^2 ^{9}Be target.

If until now the discussion was focused on radioactive ion production, the next section describes the technique used at GSI in isotope separation.

4.3 In-flight separation using the Fragment Separator (FRS)

The GSI projectile fragment separator (FRS) is a versatile magnetic spectrometer for relativistic heavy ions, designed to spatially separate the nuclear reaction products from the primary beam and to perform an efficient isotopic separation for selected projectile fragments. About the FRS, one can find a full description in [Gei1992]. In the following only a general presentation of the device is given.

The FRS is an achromatic magnetic forward spectrometer (see Figure 4.6). The system has four independent stages, each consisting of a 30° dipole magnet and a set of quadrupoles before and after the dipole to fulfill first-order focussing condi-

tions. While the quadrupole magnets in front of the dipole magnets are adjustable to illuminate the field volume of the bending magnets to achieve a high momentum resolving power, the quadrupoles behind the dipole magnets determine the ion-optical conditions at the four focal planes F1 to F4 as indicated in Figure 4.6. The ion-optical system can be corrected for second-order aberrations by using sextupole magnets placed in front of and following each dipole magnet.
In the achromatic mode of operation point-to-point images in x direction, i.e the direction of dispersion, are required at all four focal planes; the momentum dispersions of the first and the second dipole stages are cancelled by that of the third and the fourth, so that the overall system from target to F4 is achromatic.

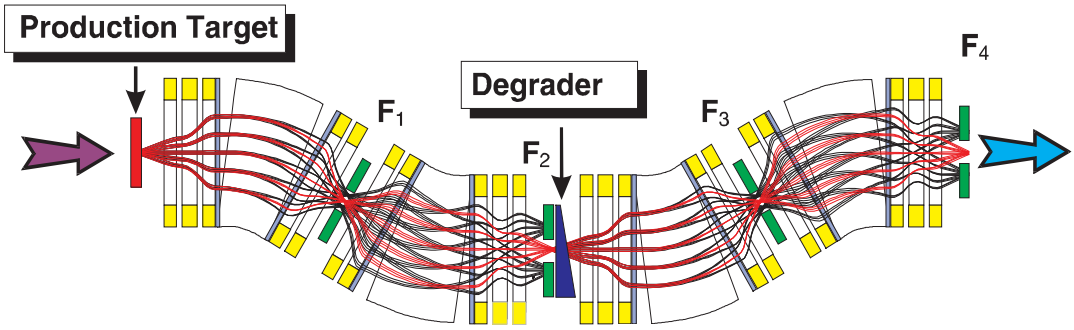

Figure 4.6: FRS in achromatic mode with a shaped energy degrader at the dispersive focal plane F2. Slits (drawn in green) are available at each focal plane. (Courtesy Dr. M. Winkler)

The particle detection in the FRS is performed by using multiwire proportional chambers installed at all focal planes, being used to analyze the primary beam or reaction products with respect to position, angle, and Bρ value. Particle identification with respect to A and Z is achieved by coincidence measurements of the energy loss (ΔE) in an ionization chamber (MUSIC) placed at the final focal plane, the magnetic-rigidity (Bρ) analysis at dispersive focal plane F2, and the velocity determination with two time-of-flight (TOF) detectors placed at F2 and F4, as shown in Figure 4.1 at the beginning of the chapter. The flight path of the particles between F2 and F4 is of roughly 35 m.

For experiments with secondary beams it is necessary that the selected radioactive beam is separated from all the other reaction products. The principle of separation employed at the FRS is based on a combination of magnetic rigidity analysis and atomic energy loss of the fragments in matter, the so-called Bρ-ΔE-Bρ method.

4.3.1 Bρ-ΔE-Bρ separation method

The keys to isotopic separation are an achromatic ion-optical system and a shaped energy degrader placed at the dispersive focal plane F2, which preserves the achromatism of the spectrometer (see Figure 4.6).

The energy degrader is a wedge of aluminum with adjustable slope and thickness [Han1990]. The mean thickness of the wedge together with the Bρ-settings of both magnetic separator stages in front of and behind the energy degrader define the nuclear charge Z and the atomic mass number A of the fragment to be selected.

According to the fundamental principle of dynamics, the motion of a particle with charge q and mass m moving in a magnetic field with a velocity v, is described by the following equation :

$$\frac{d}{dt}(m \cdot \vec{v}) = \vec{F}_{Lorentz} \equiv q \cdot \vec{v} \times \vec{B} \tag{4.1}$$

If one applies the above equation to the case of the FRS dipole magnets where $\vec{B}$ and $\vec{v}$ are uniform and perpendicular to each other, and the *Lorentz force* acts like a centripetal force ($|\vec{F}_{Lorentz}| = \frac{mv^2}{\rho}$), the equation (4.1) results into the equality :

$$B\rho = \frac{p}{q}, \tag{4.2}$$

where ρ is the bending radius of the trajectory. The ratio $\frac{p}{q}$ $(= B\rho)$ is called *magnetic rigidity* and it is a characteristic of a particle with a certain mass, charge and velocity.

At relativistic energies, the projectile fragments are fully stripped ($q = Ze$) and their momentum is defined by the relation $p = \beta\gamma Auc$. Hence, the equation (4.2) transforms to :

$$B\rho = \beta\gamma c\frac{Au}{Ze}, \tag{4.3}$$

with the relativistic parameters β and γ, the speed of light c, the elementary charge e and the atomic mass unit u.

Keeping in mind the equation (4.3), which one may interpret as a fundamental relation for isotopic identification, the separation of the fragment products at the FRS can be achieved in two phases :
i) the first two dipole stages of the FRS provide a momentum selection $B\rho_1$.
Since the reaction mechanism approximately conserves the velocity of the projectile fragments, this selection is mainly sensitive to $\frac{A}{Z}$; ($B\rho_1 \propto \frac{A}{Z}$). Thus, the fragments with the same magnetic rigidity or $\frac{A}{Z}$ ratio are focused on the same position of the energy degrader.
ii) after the first two dipole stages the selected ions undergo a slowing down in the degrader and lose momentum differently according to their A and Z. This momentum loss is exploited by the second half of the FRS to provide a second separation inside the subset of fragments having $\frac{A}{Z} \approx$ constant. The different atomic energy loss of the ions penetrating the degrader provides the additional selection criterion needed for the separation of a selected nuclide ($B\rho - \Delta E - B\rho$ method).

As a direct application of the Bρ-ΔE-Bρ separation method, the effect of the intermediate focal plane energy-shaped degrader on the isotopic separation was investigated. Three cases were studied with a 700 A·MeV ^{124}Xe primary beam impinging on a 4 g/cm^2 ^{9}Be target. The fragment chosen to be on the optical axis of the separator was ^{112}Sn in all the three cases corresponding to an Al degrader thickness of 2 g/cm^2, 3 g/cm^2, and 4 g/cm^2 respectively, which was placed at the intermediate focal plane of the FRS. The experimental results are illustrated in Figure 4.7. This investigation indicates that a relatively thick degrader has to be mounted in order to optimize the separation of the fragment of interest. Thus a degrader with thickness of 4.59 g/cm^2 and 4.83 g/cm^2 for the ^{108}Sn and ^{112}Sn fragment settings, respectively, was used in the experiment. This allowed an optimized separation of the fragment of interest amounting in both cases to $\backsimeq$ 60% of the secondary beam cocktail (see Chapter 5).

4.3.2 Fragment identification

It was aforementioned that the fragments separated in-flight by the FRS can be studied directly at the final focal plane of the separator with the help of a detector system for identification in A and Z of the fragments. Following these are the detectors we shall focus our attention on.

The MUSIC detector — nuclear charge *Z* information

The MUSIC detector is a **MU**ltiple **S**ampling **I**onization **C**hamber with eight anode strips (Figure 4.8). It is operated as counting gas with pure CF_4 at room temperature and atmospheric pressure. Each anode strip is read out with an optimized charge sensitive preamplifier and shaper combination for particle rates up to 200 kHz. Since the number of generated electrons in the counting gas is roughly proportional to the square of the charge of the penetrating particle, the output of the shaper is a measure of the atomic number of the particle. More information concerning the MUSIC detector employed in the RISING experiments can be found in [Sto2000], including its electronical read-out scheme.

Determination of the projectile fragment nuclear charge Z : The MUSIC detector can deliver energy loss and time information from each of its eight anodes. The total energy loss information can be in principal extracted as a geometrical average of the eight anode energy loss data.
When traversed by an ionizing particle, the gas inside the detector generates a cloud of electrons and ions along the particle trajectory, and the eight anodes produce a signal proportional to the number of the stripped electrons collected. Therefore, the ionization chamber measures the stopping power of the fragments, which is expressed by the Bethe-Bloch formula as

$$-\frac{dE}{dx} = k\frac{Z^2}{\beta^2}\frac{\widetilde{Z}}{\widetilde{A}}\left(\frac{1}{2}ln\frac{2m_e c^2\beta^2\gamma^2 T_{max}}{I^2} - \beta^2 - \frac{\delta}{2}\right),$$

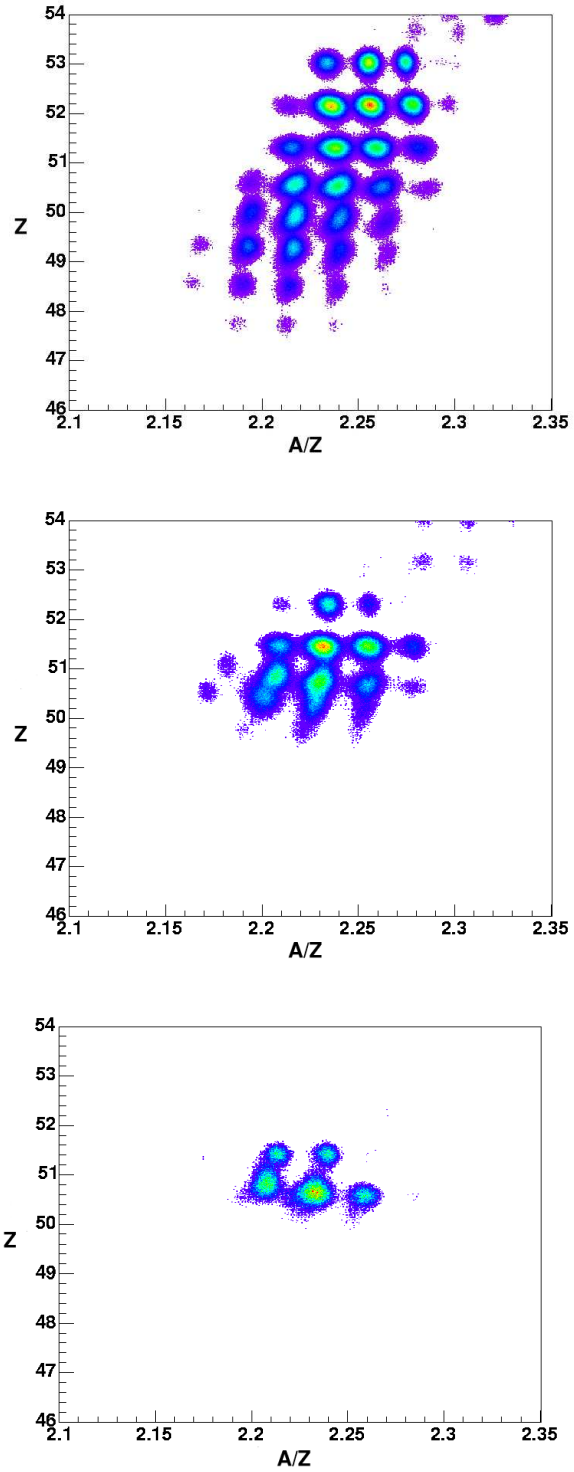

Figure 4.7: Isotopic separation at the final focal plane corresponding to a different degrader thickness, respectively, 2 g/cm^2 (top), 3 g/cm^2 (middle) and 4 g/cm^2 (bottom).

where I is the mean excitation potential (eV), T_{max} is the maximum energy transfer in a single collision, δ is the density effect correction to ionization energy loss, $\widetilde{Z}$, $\widetilde{A}$

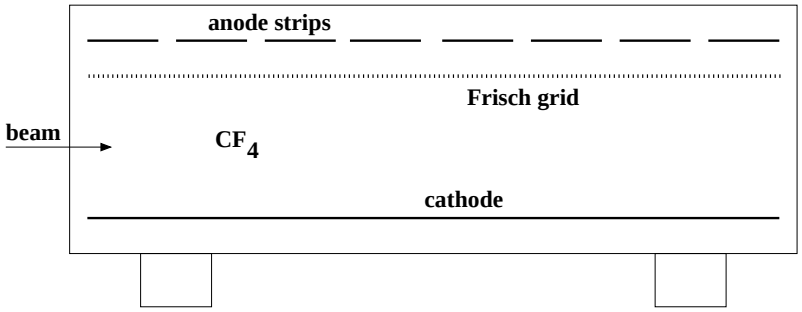

Figure 4.8: Schematic layout of the RISING eight-fold multiple sample ionization chamber (MUSIC).

are the atomic number and the mass number of the detector gas, and Z and β are the atomic number and the velocity factor of the ionizing particle, respectively.
For particles in the same material medium, the Bethe-Bloch formula reduces to

$$-\frac{dE}{dx} = Z^2 f(\beta),$$

where $f(\beta)$ is a function of the particle velocity only.
Thus, the energy loss in a given material is dependent only on charge and velocity of the particle. In practice, the measured pulse height signal from the ionization chamber depends on other factors as well. For example, the stripped electrons, falling towards the anodes, could recombine in the gas of the ionization chamber causing a dependence on the distance from the interaction point of the ionizing fragments to the anodes. This dependence can be investigated by plotting the average energy loss against the position measured in the drift direction of the electrons. Another factor that sometimes has to be taken into account is the density of the gas in the detector that can vary with time due to changes in the atmospheric conditions, i.e. temperature and pressure.
Coming back to the position dependence, this was investigated carefully by simultaneously illuminating the MUSIC detector and the MWPC detectors with defocused ^{124}Xe primary beam. As aforementioned, the MUSIC detector was mounted at the final focal plane F4 in between the two MWPC detectors. Thus, with the help of the tracking information provided by the two MWPC detectors, one can determine on an event-by-event basis the position of the fragments inside the ionization chamber. By plotting the average energy loss as a function of this position, and fitting the dependence with a polynominal of at least second order, the coefficients of the polynomial correction can be determined and used to remove the position dependence. The results of this operation are shown in the figure below.

The position of the fragments inside the ionization chamber can be derived by tracking of the fragment trajectories with the two MWPC detectors or can be provided by the MUSIC detector itself depending on which direction the drift voltage is applied. In the case of the ionization chamber used in RISING, the drift voltage is applied vertically, thus the electron drift time information could be used to extract the y-positions only. However, this is of less interest since the beam is well focused

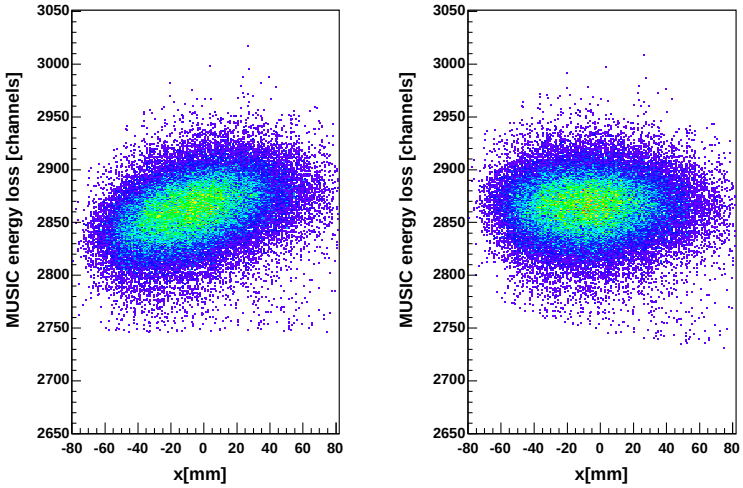

Figure 4.9: Illustrative plots of (left) the position dependence of the "raw" average energy loss, and (right) the average energy loss corrected for the position dependence.

on the y direction. The time signals therefore are not usually considered and consequently the position dependence mainly caused by electron recombination cannot be investigated properly. In this case, one can still correct the average energy loss with respect to position dependence by considering the x-position in the direction of the dispersion as illustrated in Figure 4.9. Such x-position dependence is rather weak and, as a matter of fact, inexplicable since the detector should be symmetric in the x direction.

The MUSIC energy resolution before position-dependence correction was found to be 2.3 %, while after the x-position correction 2.0 % (Figure 4.10).

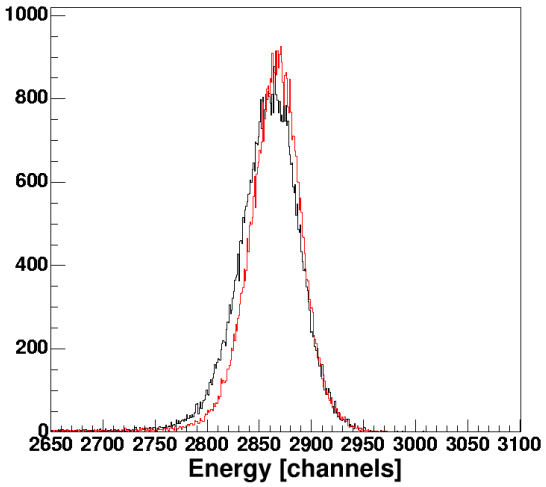

Figure 4.10: Comparison between the MUSIC energy resolution before (black histogram) and after (red histogram) the position-dependence correction. Primary beam was defocused at the final focal plane F4.

Within the framework of the Bethe-Bloch formalism described earlier, one can infer *scaling laws* for dE/dx in the case of particles with the same velocity factor β in a certain material medium. Hence, if we know the dE/dx for a particle of charge Z_1, then the energy loss of a particle of charge Z_2 in the same material may be found from the value of particle 1 by scaling the energy of particle 2, i.e.

$$-\frac{dE_2}{dx}(\beta) = -\frac{Z_2^2}{Z_1^2}\frac{dE_1}{dx}(\beta).$$

Applying the scaling law for dE/dx, the fragment proton number $Z_{fragment}$ is normally calculated as the product between the primary beam proton number $Z_{primary}$ and a velocity-dependent factor, which is obtained as the ratio of the position-corrected energy loss of the fragment and that of the primary beam having the same velocity as the fragment of interest,

$$Z_{fragment} = Z_{primary}\sqrt{\frac{\Delta E^{fragment}_{position-corrected}\beta)}{\Delta E^{primary}_{position-corrected}(\beta)}}.$$

The primary beam average energy loss as function of the velocity factor β is determined during the standard FRS calibration procedure[1], when the response of the MUSIC chamber to primary beam particles at varying energies within the range of the fragment of interest energy is mapped out; typically it is expressed as a third order polynomial function, obtained by fitting the position-corrected energy loss as a function of β velocity factor,

$$\Delta E^{primary}_{position-corrected} = c_0 + c_1 \cdot \beta + c_2 \cdot \beta^2 + c_3 \cdot \beta^3.$$

Hence, the $Z_{fragment}$ of a fragment with measured velocity factor β and position-corrected energy loss, $\Delta E^{fragment}_{position-corrected}$, can be expressed as

$$Z_{fragment} = Z_{primary}\sqrt{\frac{\Delta E^{fragment}_{position-corrected}(\beta)}{c_0 + c_1 \cdot \beta + c_2 \cdot \beta^2 + c_3 \cdot \beta^3}}.$$

The time-of-flight detectors

As it was discussed in the previous sections, when it comes to identify the fragment of interest regardless whether one refers to its mass or its nuclear charge, in both cases the information on its velocity is required. For a given flight path, a velocity measurement is nothing more than a time-of-flight measurement. Therefore, in the following the two plastic scintillator detectors used in a standard FRS set-up (see Figure 4.1) are described by their characteristics and applicability which can go beyond a time-of-flight measurement being used as position sensitive detectors, if needed. More detailed information concerning these type of detectors, one can find

[1]Detailed information about the "On-line Calibrations" needed to set up any experiment at the FRS, is available on **http://www-w2k.gsi.de/frs/technical/DAQmanual/frscalib.html**

in [Vos1989]. In addition the reference [Wol2005] provides more specific description about the RISING time-of-flight detectors.

The two scintillators are named throughout this work as SCI1 and SCI2 according to their location along the FRS beam line. The first detector SCI1 is placed at the intermediate focal plane of the separator, while the second detector SCI2 at the final focal plane at the exit of the separator.
The scintillation material is of plastic type BC420[2] with high light output (64 % of anthracene) and a fast signal rise time (500 ps). The scintillation light is registered by means of fast photomultipliers (PMT) of H2431[3] type in each direction, left-right, up-down since their active area is sufficient for reading out the horizontal and vertical coordinates, respectively. These detectors with a thickness of 0.5 mm and a diameter of 250 mm have a typical intrinsic time resolution of about 200 ps (FWHM).
The anode signals of the photomultipliers are fed into constant-fraction discriminators (CFD). The digital outputs of these electronic units served to start and stop time-to-analog converters (TAC) delivering information on the position of the fragments from the time difference of the signals of each detector. The scintillator SCI1 provides only the x-position information due to restricted available space at the midplane F2, while the scintillator SCI2 provides both x- and y-position information. The analog signals corresponding to the time-to-analog converters are recorded further by analog-to-digital converters. All this is sketched in Figure 4.11.

Position information: As mentioned above, the position information is obtained by using TACs to accurately measure the time difference between the right and left PMT signals. The conversion of left-right time difference into position is done after simultaneously illuminating the two scintillators and the MWPC detectors with defocused primary beam. The position calibration coefficients are determined by fitting with a polynomial function the two-dimensional spectra representing the x-position measured by tracking with the two MWPCs versus the left-right time differences measured by each of the two scintillators.

Time-of-flight information: The time-of-flight of the fragments in the FRS is determined by measuring the time differences between the two scintillators with simultaneous readout of the right- and left-side photomultipliers. In order to compensate for differences in the path length for fragments that deviate from the ideal trajectory (the central trajectory along the beam optical axis), the final time-of-flight information is given by the arithmetic average between the right-right (TOF_{right}) and left-left (TOF_{left}) time differences.

In the following, a quantitative determination of the *absolute time-of-flight* is given.

The particle time-of-flight through FRS is the difference in time at which the parti-

[2]Bicron Corporation, Bodegraven, Netherlands
[3]Hamamatsu Photonics Deutschland GmbH, Herrsching, Germany

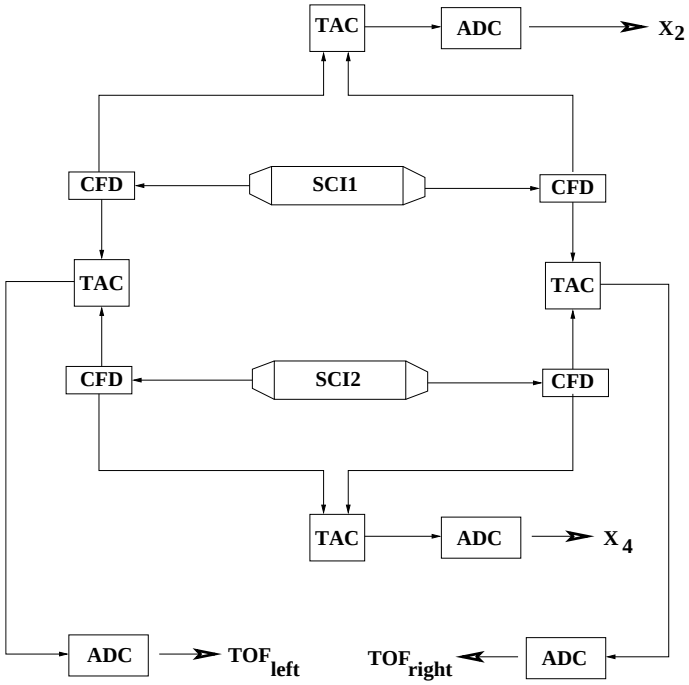

Figure 4.11: The electronic read-out scheme of the time-of-flight detectors SCI1 and SCI2, where the X_2 and X_4 correspond to the positions of the fragments at the F2 and F4 focal planes, respectively.

cle passes through the scintillator SCI2 (at the time T_2) and through the scintillator SCI1 (at the time T_1). Since on its path, the particle interacts first with the scintillator SCI1 and afterwards with the scintillator SCI2, the time T_2 is bigger than T_1 ($T_2 > T_1$). However, it is the scintillator SCI2 that triggers the data acquisition system (see Section 4.8), thus this detector should provide a signal faster than any other FRS detector. In this respect, a certain electronic delay ΔT is used to delay the signal of the scintillator SCI1 so that $T_1 + \Delta T > T_2$.
The *measured time-of-flight*, let it be named — TOF^*, is the average of the right-right (TOF_{right}) and left-left (TOF_{left}) time signals, transformed from TAC channels to picoseconds through the calibration coefficients α_L and α_R,

$$TOF^* = \frac{TOF_{left} \cdot \alpha_L + TOF_{right} \cdot \alpha_R}{2} = T_1 + \Delta T - T_2.$$

The *real time-of-flight*, let it be named — TOF_{real}, is calculated as distance divided by velocity,

$$TOF_{real} = \frac{d}{v} = T_2 - T_1,$$

where d is the flight-path through the separator, and v is the particle velocity.
From these equations, the *absolute time-of-flight* of a particle is inferred as a function of the measured TOF_{right}, TOF_{left} and the electronic delay ΔT:

$$TOF_{real} = \Delta T - TOF^* = \Delta T - \frac{TOF_{left} \cdot \alpha_L + TOF_{right} \cdot \alpha_R}{2}.$$

The electronic delay ΔT is considered to be an experiment-specific time-of-flight offset which can be determined accurately during the standard FRS calibration procedure using the primary beam. The TOF^* is measured for three or four different primary beam energies corresponding to velocity factors β. After that, the product $TOF^* \cdot \beta$ is plotted as a function of β and fitted with a linear polynominal,

$$TOF^* \cdot \beta = c_0 + c_1 \cdot \beta.$$

The coefficients c_0 and c_1 have a special physical meaning. The absolute value of the product $c_0 \cdot \beta$ is nothing but the flight-path through the separator, while c_1 represents the time-of-flight offset aforementioned. These two parameters are used later for the calculation of the mass-to-charge ratio A/Z.

A/Z determination

In Section 4.3.1, the following mathematical expression was introduced for the isotopic identification:

$$\frac{A}{Z} = \frac{e}{uc}\frac{B\rho}{\beta\gamma}.$$

Here, the velocity factor β is determined on an event-by-event basis by measuring the time-of-flight as it was described earlier ($\beta = -c_0/(c_1 - TOF^*)$). The $B\rho$ is the magnetic rigidity in the second half of the separator corresponding to the central trajectory on the beam optical axis. In reality, the particle trajectories deviate from the optical axis, deviations reflected in the measured X_2 and X_4 positions in the x-direction at the intermediate (F2) and final (F4) focal planes, respectively. Taking into account several beam optics parameters, like magnification (V_2) and dispersion (D_2), one can express the $B\rho$ magnetic rigidity on an event-by-event basis as follows

$$B\rho = B\rho_0\Big(1 - \frac{X_4 - V_2 X_2}{D_2}\Big),$$

with $B\rho_0$ the "ideal" magnetic rigidity corresponding to the central trajectory along the beam optical axis.

Combining the above expression of the magnetic rigidity in the second half of the separator with the equation (4.3), one can determine the mass-over-charge ratio A/Z for the fragment of interest depending only on its velocity and magnetic rigidity. Do not forget at this point that any inaccuracy in the β determination is as well reflected in the measured A/Z mass-over-charge ratio. A common source of systematic errors comes from the fact that already the time-of-flight is measured with a certain accuracy due to the existence of the MWPC detectors and the MUSIC ionization chamber in between the two time-of-flight detectors.

The MWPC detectors

Detailed information on multiwire proportional chambers with a two-stage gas amplification, which are sort of standard detectors for beam monitoring and experi-

ments at the SIS/FRS, one can find in [Ste1991]. A schematic layout of such a MWPC is shown in the Figure 4.12.

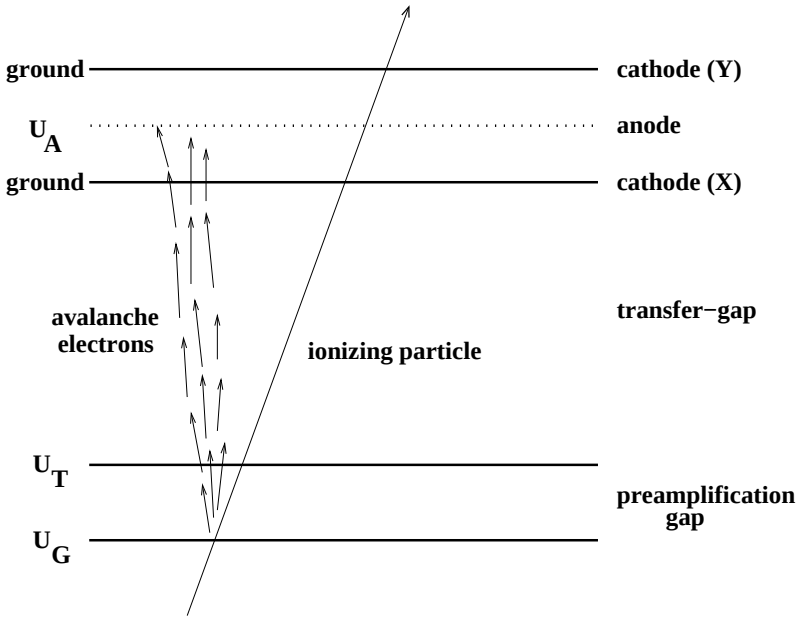

Figure 4.12: Schematic layout of a two-stage MWPC. See text for details.

The anode plane consists of wires with a pitch of 2 mm, while the cathode electrodes are made of wires with a pitch of 1 mm. The wire directions in X and Y are orthogonal to each other, the wires of the anode plane being on the diagonal direction at 45° with respect to the cathode planes. The anode-cathode spacing is 5 mm. To this ordinary MWPC a planar electrode structure is added consisting of two meshes. Typical potentials applied to these electrodes are: $U_G = -10$ kV, $U_T = -2.6$ kV, and $U_A = +2.5$ kV. The readout planes X and Y are on ground.

The two MWPC detectors used in RISING for tracking and beam position information are of a similar type. The detectors have an active area of 20 × 20 cm^2 and are filled with a mixture of Argon-CO_2 as operating gas. The readout of the X and Y planes is made with a delay line technique: the time difference between the occurrence of the event (as given by an external device or by the anode signal itself) and the detection of a signal at the ends of the delay line represents the space coordinate. With a delay line of about 1 μs, the maximum particle rate is 1 MHz, but in practice one should rely on a factor of 10 less. The position resolution of these detectors is better than 1 mm.

Position calibration : As aforementioned, the readout is done via a delay line and not by reading out single wires. Each wire corresponds to a different delay time with respect to the time reference signal (in our case the so-called "accepted trigger", see Section 4.8), which is recorded by a TDC (**T**ime-to-**D**igital **C**onvertor). The TDC channels are named XL, XR, YU, YD (X_{left}, X_{right}, Y_{up}, Y_{down}). For a good event the sums "XL + XR" and "YU +YD" should be constant. Under this

condition the positions are determined event by event from the difference of the delay corresponding to the fired wire, as follows

$$x[mm] = x_{factor} * \frac{(XL - XR)}{2} + x_{offset}$$

$$y[mm] = y_{factor} * \frac{(YU - YD)}{2} + y_{offset}$$

The x_{factor} and y_{factor} depend on the delay lines and TDCs used. They should be equal to 0.1465 mm/channel, taking into account the fact that the 200 wires spaced by 1 mm are readout each two wires by a delay chip of 4 ns and that the range of the TDCs, which corresponds to 4096 channels, is of 1200 ns. In reality, the value of 4 ns is not the same for all 100 delay chips used for each space coordinate (X or Y). Therefore, the ratio of "4ns/2mm" cannot be used to determine accurately the conversion factors x_{factor} and y_{factor}. Moreover, the TDCs show nonlinearities from channel to channel along their dynamic range that introduce deviations from the theoretical numbers. Hence, there are several approaches that can be applied to experimentally determine these conversion factors, see [Ban2004] for detailed information.

The offsets x_{offset} and y_{offset} are necessary because the MWPCs are only aligned with an accuracy of about 1 mm relative to the beam optical axis. For offset calibration one can apply a few methods: the easier one is to use a pulser signal fed into the middle of the delay line to obtain the electronic center of the detector. Another method is to align the primary beam with the current grids and look where the beam position is shown on the MWPCs. In this case the beam intensity must be decreased to several hundred particles per spill. The offsets are then determined by taking the mean value of the resulting position spectra.

4.4 Quality of secondary beams

A specific characteristic of the RISING experiments is the use of rather low beam energies ($\sim$ 100 A·MeV) at the secondary target, which deteriorates the beam quality and transmission through the FRS due to large angular and energy loss straggling in the middle focal plane degrader and detectors located in the final focal plane area before the secondary target.

By particle trajectory tracking performed with the help of the two MWPC detectors, the profile of the secondary beam can be extrapolated on the secondary target, as illustrated in Figure 4.13. The horizontal beam size amounts to 4.1 cm (FWHM).

Since the beam spot on target is quite large, tracking of the incoming/outgoing fragment trajectory is necessary in order to determine the vertex of the scattering process. This information is needed on a event-by-event basis to apply Doppler

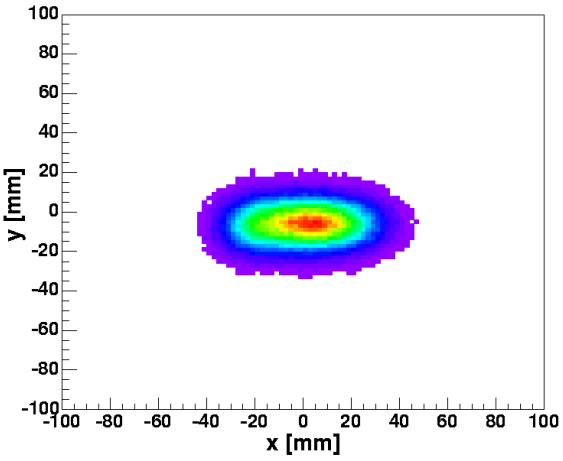

Figure 4.13: Secondary beam profile at the reaction target extrapolated with the help of the RISING tracking detectors, the two MWPSs, MW1 and MW2.

shift correction, as discussed in detail in Section 4.7.

Another factor characterizing the quality of secondary beams is the width of the beam velocity distribution. This factor plays an important role for a mass resolution measurement with the calorimeter telescope CATE [Loz2005]. The consequence of large straggling effects on the secondary beam velocity distribution due to the matter in the beam spectrometer is suggestively depicted by comparison to the primary beam velocity distribution measured without any matter in the spectrometer except the two time-of-flight detectors (see Figure 4.14).

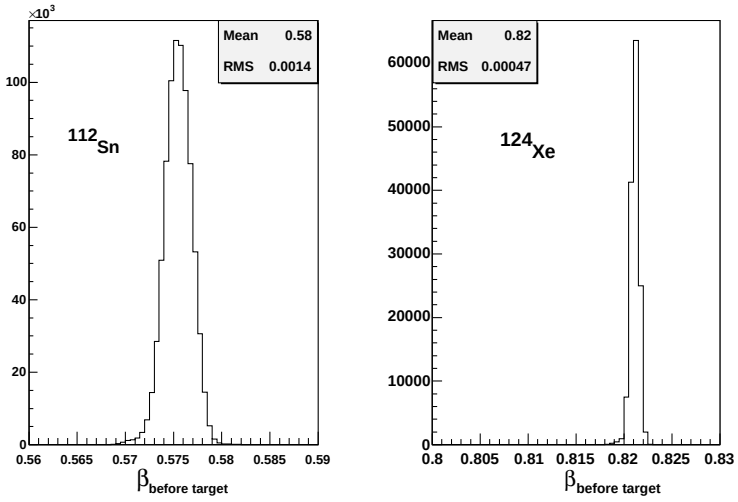

Figure 4.14: Secondary beam velocity distribution in the case of ^{112}Sn fragments measured with a resolution (RMS) of 0.24% (left) by comparison to the primary beam ^{124}Xe velocity distribution measured with a resolution (RMS) of 0.06 % (right).

4.5 Secondary target

In heavy-ion reactions with secondary beams, thick targets are used in order to partially compensate for the low beam intensities. In the case of the experiment under investigation here, a secondary ^{197}Au target with a thickness of 386 mg/cm^2 was placed at the final focal plane of the FRS.

In the following, secondary target effects like angular and energy-loss straggling as well as background radiation originating from atomic processes are discussed.

4.5.1 Angular and energy-loss straggling

There are two main atomic processes that have to be taken into account when thick targets are employed in experiments with radioactive fragment beams, namely, energy-loss straggling and angular straggling.
While the energy-loss straggling at relativistic energies has been found to be rather small (less than 1%) even for relatively thick targets (600 mg/cm^2), the angular straggling shows a strong dependence on target thickness which limits the impact parameter measurement for peripheral collisions. The corresponding angular straggling for a target thickness of 386 g/cm^2, as used in the experiment, amounts to approximately 8 mrad (see Figure 4.15). This is the equivalent of 0.5°, representing in our case the most significant contribution to the experimental uncertainty for the impact parameter measurement.

Figure 4.15 depicts the angular straggling in a gold target for Ni, Sn and Pb projectiles at 100 A·MeV as function of the target thickness [Wol2005].

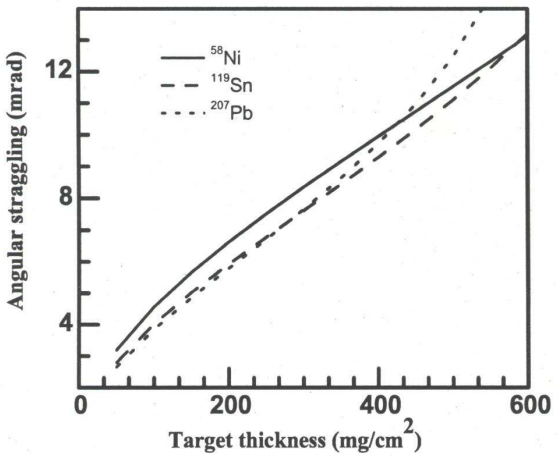

Figure 4.15: Angular straggling in a gold target as function of the target thickness for Ni(solid line), Sn (long-dashed line) and Pb projectiles (short-dashed line) at 100 A·MeV.

4.5.2 Atomic background radiation

The main source of electromagnetic background radiation encountered in relativistic heavy-ion reactions comes from atomic processes. Among these processes the strongest contributions [Anh1986] to the background are:

- emission of K and L X-rays from ionized target atoms;
- radiative electron capture of target electrons into the projectile (REC);
- emission of primary bremsstrahlung from target electrons scattering off the projectile (PB);
- emission of secondary electron bremsstrahlung from energetic knock-on electrons rescattering in the target and/or surrounding material (SEC).

The atomic cross sections of all these processes depend strongly on the atomic number of the projectile and target, in particular PB scales with $Z_p^2 Z_t$ and SEC with $Z_p^2 Z_t^2$.
The angle integrated cross section $d\sigma/dE$ is illustrated in Figure 4.16 for ^{132}Sn fragments at different beam energies on a gold target (left) and at 100 A·MeV on different target such as Be, Sn, and Au (right) [Wol2005].

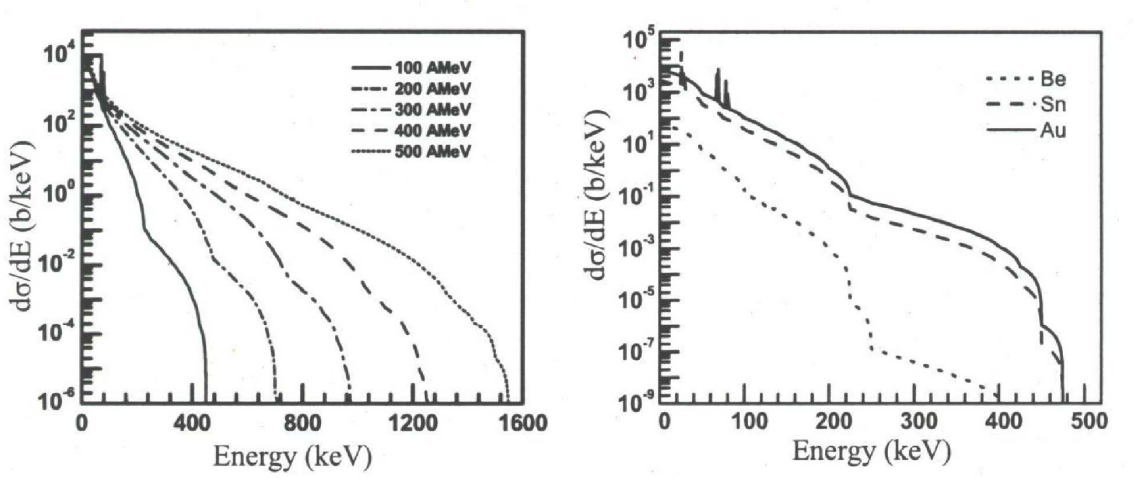

Figure 4.16: Angle-integrated cross section as a function of γ-ray energy for the atomic radiation background from ^{132}Sn on a Au target at different beam energies (left). Cross section dependence on different target materials (Be, Sn, Au) for ^{132}Sn fragments at 100 A·MeV (right).

Figure 4.16 illustrates the limitation imposed by the atomic radiation background that one has to take into consideration while performing γ-ray spectroscopy down to 400 keV energies. At these small γ-ray energies the atomic background cross sections can reach several kbarns, a number which is at least four orders of magnitude larger than typical Coulomb excitation cross sections. This is one of the reasons that played a major role in limiting the beam energy in RISING experiments to 100 A·MeV.

4.6 Reaction channel selection with the CAlorimeter TElescope (CATE)

Stacks of detectors called telescopes, measuring the energy loss and residual energy of charged particles, have been used for long time to get charge and mass identification. The identification is obtained by plotting the energy loss in one component of the detector stack versus the residual energy released in the detector in which the particle has stopped.

For the RISING project the calorimeter telescope (CATE) [Loz2003, Wol2005] was developed to identify the scattered particles and fragments following the reactions on the secondary target, as well as to measure their scattering angles.
The CATE detector array consists of 3×3 Si-CsI(Tl) modular $\Delta E - E$ telescopes covering a solid angle of 58 mrad at 1.43 m downstream from the secondary target.

4.6.1 CATE(Si)–ΔE detectors

The transmission (ΔE) Si detectors used in the experiment discussed in this work were produced by the EURISYS company (model: IPP-IPP 2D).
The geometrical size and the active area of each square shaped Silicon detector with a thickness of 300 μm are 54×54 mm^2 and 50×50 mm^2, respectively, resulting in a geometrical efficiency of 92 %. A picture of the CATE(Si) detectors mounted on the array motherboard is shown in Figure 4.17.

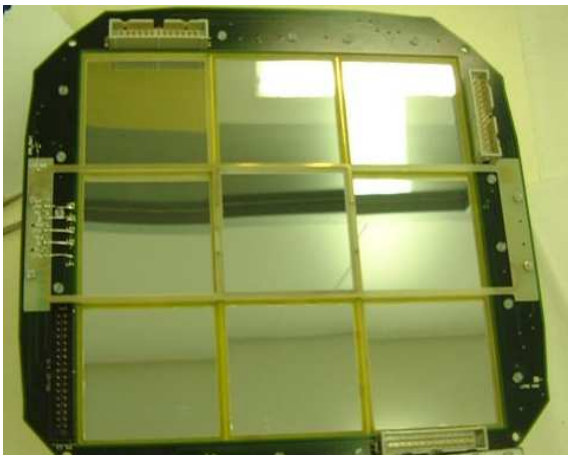

Figure 4.17: Photograph of CATE (Si) detectors attached to their motherboard.

The detectors are two-dimensional position sensitive, which can be exploited for an impact parameter measurement in Coulomb excitation scattering experiments.
The ΔE energy loss deposed in the Si detector array is measured from a contact on the rear face of each Si detector. A resistive layer with a sheet resistance of 2 kΩ on the front side of each detector module serves as a charge divider to four

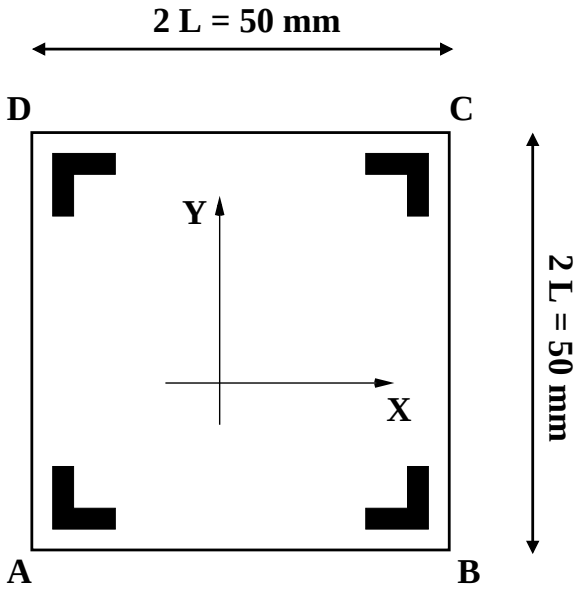

Figure 4.18: Schematic drawing of a typical two-dimensional position sensitive CATE(Si) detector module. The position of particle incidence is given by the following expressions: $X/L = [(B+C)-(A+D)]/(A+B+C+D)$ and $Y/L = [(D+C)-(A+B)](A+B+C+D)$, where A, B, C and D are pulse height signals from four output contacts and L is the half length of the squared-shape detector module.

corner contacts. The four signals from these contacts are used to extract the coordinates of the ion impinging position and in the following they are referred to as *position signals*. The Si detector prototype energy resolution obtained with α particles is 80 keV for the 5.48 MeV ^{241}Am line. Measurements with heavy ions have revealed a position resolution better than 7 mm (FWHM) [Wol2005, Doo2003].

Next it is described how the position information is reconstructed by the two-dimensional position sensitive Si detector array used in the experiment.

Position pattern reconstruction

The charge information of the four position signals does not allow in general for a straightforward determination of the incident position.
In Figure 4.18 one of the two-dimensional position sensitive CATE detectors is drawn schematically.

The two-dimensional position of ion incidence (X, Y) for a CATE(Si) detector module with a length $2L$ can be given by the following expressions:

$$X = L\frac{(B+C)-(A+D)}{A+B+C+D}, \qquad Y = L\frac{(D+C)-(A+B)}{A+B+C+D}, \tag{4.4}$$

where A, B, C and D are the pulse heights of the signals from the four positions contacts. The position expressions hold in a reference frame with the origin in the

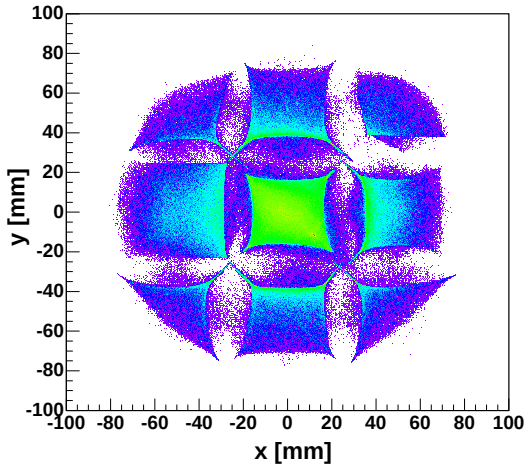

Figure 4.19: 'Pin-cushion' distortion in the position pattern obtained from the two-dimensional position expressions (eqs. 4.4). The middle detector on the left-hand side does not exhibit pin-cushion distortions being of a different type.

center of the detector and the X and Y axes parallel to the sides of the detector. However, the two-dimensional position extracted from the eqs. 4.4 exhibit a 'pin-cushion' distortion in the position pattern, as shown in Figure 4.19.

An algorithm was developed [Loz2005] to reconstruct the position pattern by applying correction to the 'raw data' position shown in Figure 4.19. Following it is described how this algorithm was applied in the data analysis of ^{108,112}Sn experiment.

A grid pattern of 11×11 points (Figure 4.21 (*top panel*)) was calculated so that it covers an area of 50×50 mm^2, with a distance interval between two adjacent points of 5 mm which fits to the detector position resolution. Another grid pattern of 11×11 points illustrated in (Figure 4.21 (*middle panel*)) is calculated [Loz2005] to reproduce the experimental 'pin-cushion' pattern. By taking the difference between

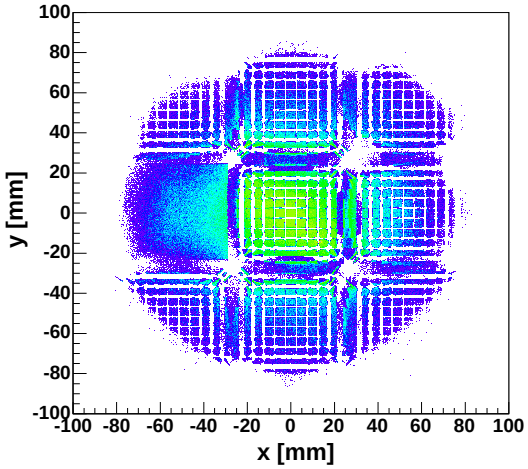

Figure 4.20: Corrected 'pin-cushion' position pattern.

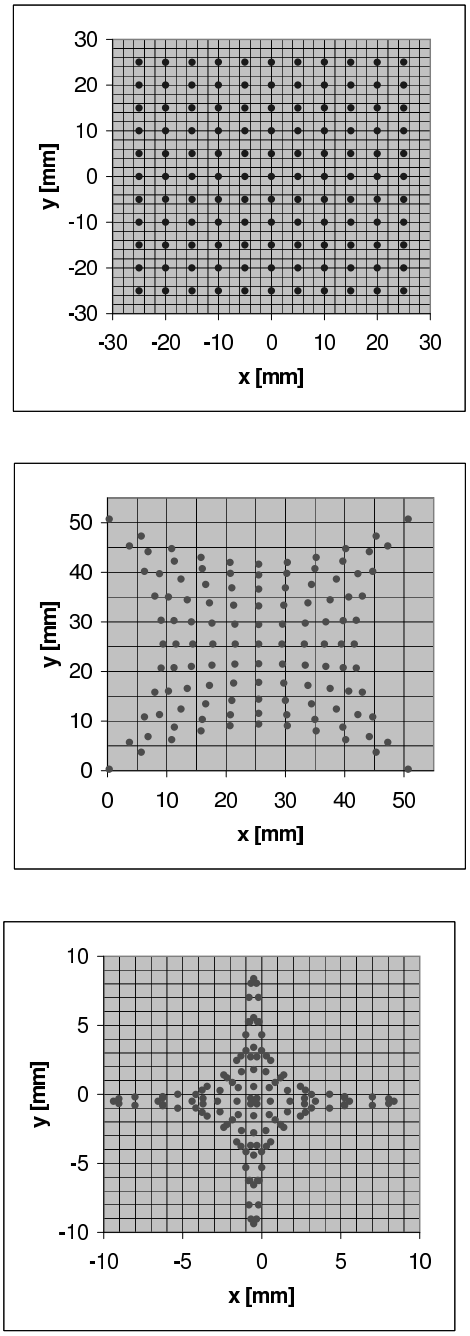

Figure 4.21: Theoretical position patterns calculated so that (top panel) corresponds to an active area (50×50 mm^2) of a CATE(Si) module, (middle panel) reproduces the experimental 'pin-cushion' position pattern, and (bottom panel) corrects the experimental distorted position value. This pattern is determined by taking the difference between the above two patterns for each of the 11×11 theoretical data points.

these two theoretical patterns for each of the 121 (X,Y) data points, one obtains the theoretical position correction pattern displayed in Figure 4.21 (*bottom panel*).

A correspondence between the calculated 'pin-cushion' position and the experimental 'pin-cushion' position is established on an event-by-event basis by determining the minimum distance from an incident position (extracted from eqs. 4.4) to all of the 121 (X,Y) points of the theoretical 'pin-cushion' pattern. Hence, the measured position is corrected event by event with the corresponding theoretical position correction. The results of a such procedure are shown in Figure 4.20.

Electronics

The block diagram of the pulse signal processing for the beam experiment is shown in Figure 4.22. Positive voltage for a reversed bias was applied to the energy (back) electrode of the CATE(Si) detector module. The applied voltage was 30 V. Four position contacts on the front surface of the silicon detector and the back electrode were connected to charge sensitive preamplifiers. Pulses formed by the preamplifier were fed to the main shaping spectroscopy amplifier (C.A.E.N.) with 2 μs shaping time. Output signals from the main amplifiers were fed to a 32-channel analog-to-digital converter (C.A.E.N./V785). The energy signal was also fed to fast timing amplifier (TU-Darmstadt/TFA99) which generates timing pulses fed as 'stop' signals into 32-channel time-to-digital converter (C.A.E.N./V878). The timing signal of the TOF scintillator (SCI2) was used as the gate input of the ADC as well as 'start' signal for the TDC. Five analog signals from each of the nine CATE(Si) detector modules were digitized by the ADC and stored in the computer through a VME controller.

4.6.2 CATE(CsI)–E_{res} detectors

The CsI(Tl) detectors provided by the company SCIONIX (model: V502P25/18-E2-Cs-X SSX848) are mounted 4 cm behind the Si detectors. Each of the nine detectors has a flat front face of 54 × 54 mm^2 size and a trapezoidal back shape corresponding to a thickness of 10 mm to 20 mm sufficient to stop heavy ions with Z ≥ 7 at 100 A·MeV. The detectors are mounted in an aluminium frame of 4 mm thickness between each two neighbours thus yielding the same geometrical efficiency of 92 % as the Si array (Figure 4.23).

The scintillation light of each crystal is collected by a photodiode of 18 × 18 mm^2 size mounted on the trapezoidal backside of the crystal. The signal of the PIN diode yields the residual energy of the fragments after passing through the Si detectors. Several tests performed with different heavy ion species (as primary beams) at energies between 100 A·MeV and 400 A·MeV revealed an intrinsic energy resolution for the CsI(Tl)–E_{res} detectors of 0.5 % taking into account the energy spread of the detected heavy ion beams and after applying a position correction which accounts for the position dependence of the scintillation light collected in the pin diodes.

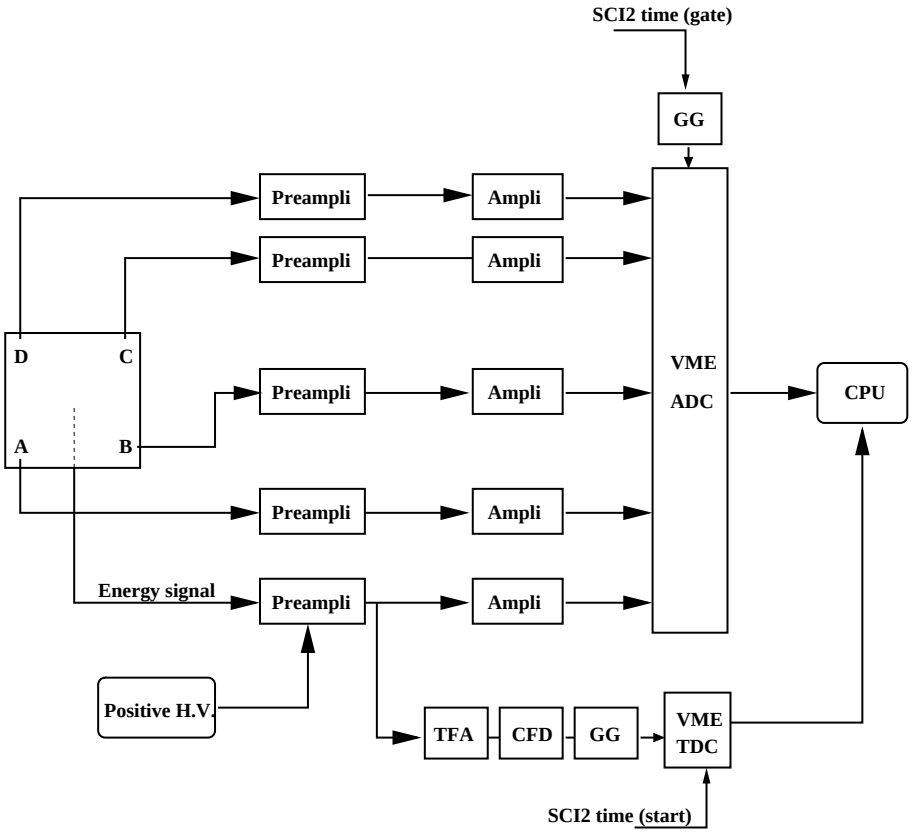

Figure 4.22: Block diagram showing the electronics used for CATE(Si) detector array. Preampli: charge sensitive preamplifier, Ampli: Spectroscopy amplifier, TFA: timing filter amplifier, CFD: constant fraction discriminator, GG: gate generator, A(T)DC: analog(time)-to-digital converter.

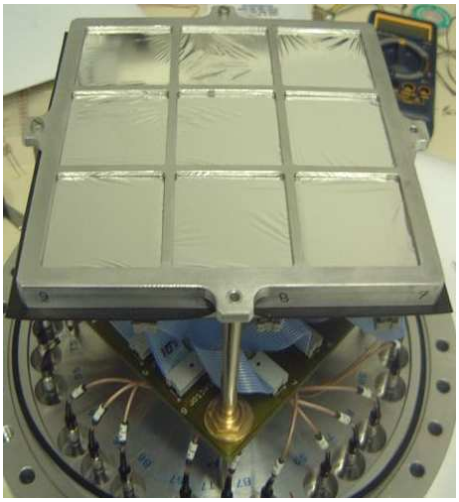

Figure 4.23: The CATE (CsI) detector array readout by a set of nine photodiodes mounted correspondingly on the backside of the detector array.

4.6.3 ΔE–E_{res} correlation (Z determination)

In any scattering experiment it is necessary to identify the particle of interest before and after the reaction target.
Figure 4.24 represents a $\Delta E - E_{res}$ correlation plot in the case of the reaction ^{197}Au(^{112}Sn,^{112}Sn*)^{197}Au. In this plot one can see not only the inelastic Coulomb scattering channel but also the fragmentation channels. However, the scattering channel dominates.

According to Bethe-Bloch formula introduced in a previous section, the following expression for the energy loss is inferred

$$\Delta E \approx \frac{mZ^2}{\Delta E + E_{res}}.$$

From this expression one can interpret the identification plot ΔE–E_{res} as a superposition of hyperboles described by the equation $mZ^2 = const$, where each of them corresponds to a certain isotopic chain of fragments, hence the atomic element Z can be determined. The inset in Figure 4.24 shows the Z distribution which is equivalent to an extracted Z resolution of 0.8 (FWHM) for the system ^{112}Sn on the ^{197}Au target.

According to the above mathematical expression, combined information of the energies detected in the Si and CsI(Tl) detectors is needed to extract the mass number A from the total kinetic energy $\Delta E + E_{res}$, thereby assuming the same velocity for all reaction products with a given charge Z.

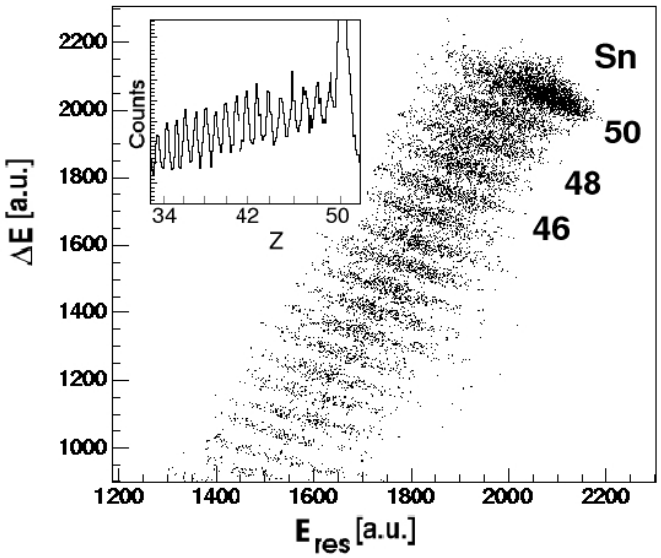

Figure 4.24: Two dimensional ΔE–E_{res} histogram corresponding to the reaction ^{197}Au(^{112}Sn,^{112}Sn*)^{197}Au. The inset shows the extracted Z distribution. (Courtesy R. Lozeva)

It has been found [Loz2005] that several effects are affecting the energy measurement, such as position of the interaction in the detectors, velocity distribution of the projectile fragments, beam intensity as well as the spill structure, and last but not least the fragmentation reaction in the target (see Section 4.2). Therefore, one has to correct these effects in order to extract the information on the total kinetic energy. However, the effect of fragmentation reaction cannot be corrected with our set-up. In the case of RISING two-step fragmentation and Coulomb excitation experiments typical mass resolution values have been obtained in the order of 2-3% and 2%, respectively [Loz2005].

4.7 High-resolution γ-ray detection with Ge-detectors

In this section the Germanium detectors employed in the RISING experiments for γ-ray detection are described taking into account the experimental requirements specific to the relativistic energy regime at which the measurements occurred.

4.7.1 Doppler effects at relativistic energies

The RISING γ-detection device is designed to perform high-resolution γ-ray spectroscopy on excited projectile residues moving at velocities of 0.43c. This corresponds to 100 A·MeV secondary beam energies. At these relativistic energies, the projectile residues emit γ rays affected by large Doppler shifts:

$$\Delta E_\gamma = |E_\gamma - E_{\gamma_0}| \quad \text{with} \quad E_\gamma = E_{\gamma_0}\frac{\sqrt{1-\beta^2}}{1-\beta\cos\vartheta_\gamma},$$

where E_γ is the measured γ-ray energy Doppler shifted relative to the γ-ray transition energy E_{γ_0}. The angle ϑ_γ is measured in the laboratory-coordinate system as the angle between the direction of the moving projectile residue and the direction of the photon emission.
The plot in Figure 4.25 illustrates the magnitude of the relativistic effects in discussion.

Under relativistic conditions one deals with Doppler broadening due to the finite opening angle of the γ-detector ($\Delta\vartheta_\gamma$) and the velocity spread ($\Delta\beta$) at the moment of γ emission:

$$\frac{\Delta E_{\gamma 0}}{E_{\gamma 0}} = \frac{\beta\sin\vartheta_\gamma}{1-\beta\cos\vartheta_\gamma}\cdot\Delta\vartheta_\gamma \quad \text{and} \quad \frac{\Delta E_{\gamma 0}}{E_{\gamma 0}} = \frac{\beta-\cos\vartheta_\gamma}{(1-\beta^2)(1-\beta\cos\vartheta_\gamma)}\cdot\Delta\beta.$$

The opening angle of the RISING Ge-detectors is estimated as

$$\Delta\vartheta_\gamma = 0.622\arctan\Big(\frac{d}{R+30}\Big),$$

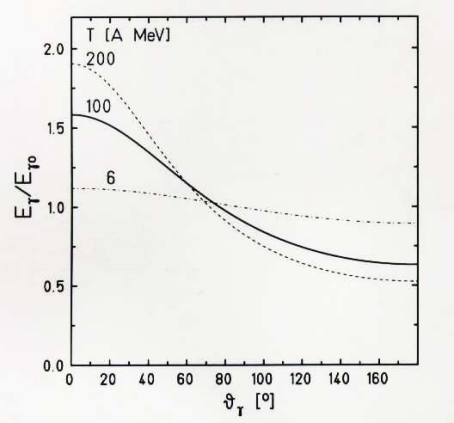

Figure 4.25: Ratio of the photon energy E_γ measured in the laboratory frame to the photon energy $E_{\gamma 0}$ in the rest frame of the projectile versus the laboratory angle ϑ_γ at bombarding energies of 6, 100 and 200 A·MeV.

where $d[mm]$ is the diameter of a Ge crystal, $R[mm]$ is the distance to the target, and 30 mm is assumed to be interaction depth in a crystal. This leads in our case, for a distance to the target of 700 mm (see next section), to a crystal opening angle $\Delta\vartheta_\gamma = 3°$.

The expected γ-ray energy resolution $\Delta E/E_{\gamma 0}$ as a function of the laboratory angle ϑ_γ at bombarding energies of 11, 100 and 200 A·MeV is shown in the Figure 4.26, where for Doppler broadening the RISING crystal opening angle ($\Delta\vartheta_\gamma = 3°$) is considered.

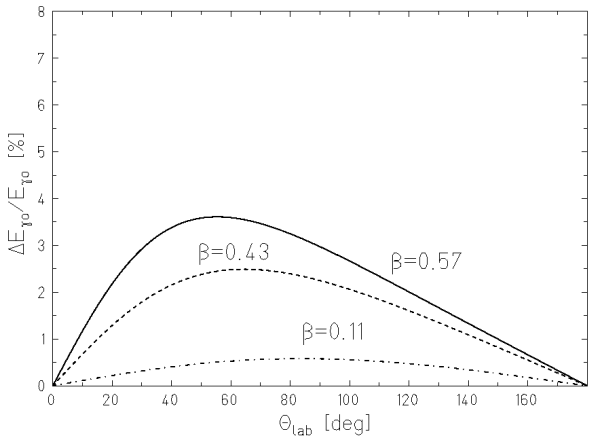

Figure 4.26: Expected γ-ray energy resolution $\Delta E_{\gamma 0}/E_{\gamma 0}$ as a function of the laboratory angle ϑ_γ. An opening angle $\Delta\vartheta_\gamma = 3°$, like in RISING, is considered.

It is clear from this plot that forward or backward angles are the most favourable

to minimize the Doppler broadening effect. In order to find the optimal positions

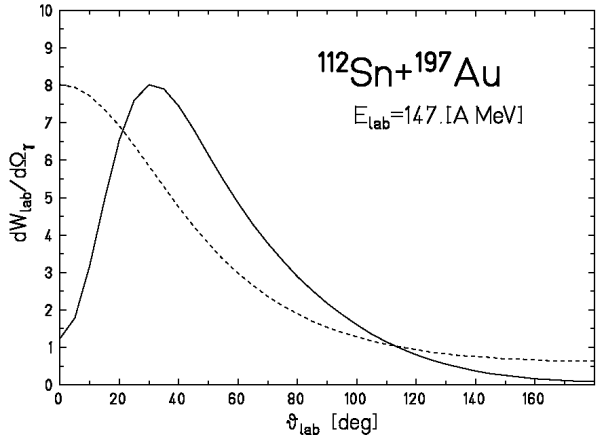

Figure 4.27: Gamma angular distribution calculated [Ald1966] in the laboratory reference for the system (^{112}Sn, ^{197}Au) corresponding to the transition $2_1^+ \rightarrow 0^+$. Dashed line stands for an isotropic distribution, while the solid line for the actual distribution.

for the γ-detectors, besides Doppler broadening, one should also take into account the angular distribution of the γ-rays.

In the case of ^{108,112}Sn measurements, both fragments have $\beta \simeq 0.50$ (after the target). In Figure 4.27 is plotted the γ-angular distribution for the system (^{112}Sn, ^{197}Au) corresponding to the transition $2_1^+ \rightarrow 0^+$. The dashed line stands for an isotropic distribution and the solid line represents the actual distribution. In both cases, the angular distribution of γ-rays in the laboratory system is peaked at forward angles. Therefore, it was this angle configuration the RISING γ-detection system was optimized for. More precisely, ϑ_γ angles of 16°, 33° and 36° were chosen (see next section).

Coming back to ^{108,112}Sn experiment, the opening angle contribution to the γ-ray energy uncertainty is dominant since the spread in velocity after the target is less than 1% (see Chapter 5). A special attention has to be drawn to very short-lived ($<$ 1 ps) 2_1^+-excited Sn isotopes since they may decay within the thick (386 mg/cm^2) gold target, hence leading to large β uncertainties ($\approx 4\%$). However, the calculations show that only 10% of the decays occur within the target, which is a small fraction to be considered.

Another relativistic effect to be discussed here is the Lorentz boost. Following basic knowledge related to the Lorentz transformation formalism are introduced.

The Lorentz transformation for γ rays : In the rest-coordinate system a photon is characterized by the polar and azimuthal angles θ_γ and ϕ_γ respectively.

In the laboratory system, the photon has a propagation direction $\Omega_{lab} \equiv (\vartheta_\gamma, \varphi_\gamma)$, where ϑ_γ and φ_γ are the corresponding polar and azimuthal angles. The relations of ϑ_γ and φ_γ to the corresponding quantities in the rest-coordinate system depend on the laboratory velocity factor β of the excited nucleus at the moment of its decay. Since in both laboratory and rest frames the z-axis is in the beam direction, the Lorentz transformation yields (see [Pel1982]:

$$\phi_\gamma = \varphi_\gamma,$$

$$\cos\theta_\gamma = \frac{\cos\vartheta_\gamma - \beta}{1 - \beta\cos\vartheta_\gamma},$$

$$d\Omega_{rest} = \frac{1-\beta^2}{(1-\beta\cos\vartheta_\gamma)^2} d\Omega_{lab},$$

where the solid-angle elements $d\Omega_{rest}$ and $d\Omega_{lab}$ are defined by $d\Omega_{rest} = \sin\theta_\gamma d\theta_\gamma d\phi_\gamma$ and $d\Omega_{lab} = \sin\vartheta_\gamma d\vartheta_\gamma d\varphi_\gamma$.

One should note the relation between the solid-angles in the two coordinate systems:

$$\frac{d\Omega_{rest}}{d\Omega_{lab}} = \frac{1-\beta^2}{(1-\beta\cos\vartheta_\gamma)^2} = \left(\frac{E_\gamma}{E_{\gamma 0}}\right)^2 = \left(1 + \frac{\Delta E_\gamma}{E_{\gamma 0}}\right)^2,$$

which corresponds to the square of the Doppler shift.

At relativistic energies, the Lorentz boost plays a major role in increasing detection efficiency of γ rays emitted at forward angles.

4.7.2 Cluster array for experiments at relativistic energies

The γ-ray detectors used in the experiment are the 15 Ge-Cluster detectors which were part of the former EUROBALL [Sim1997] spectrometer. The photograph of the set-up is shown in the Figure 4.28.

Each Ge-Cluster detector comprises seven individually encapsulated hexagonal Ge crystals [Ebe1996] housed in a common cryostat. In this way it is very easy to build different subarrays in a common cryostat or to replace one capsule if damaged. This flexibility is one of the foremost qualities of the Cluster detectors. Another advantage, typical for composite detectors, is their high granularity enabling a reduction of the Doppler broadening. The efficiency of an array of Cluster detectors depends not only on the individual absolute efficiencies, but also on the capability of the detector to be operated in the so called "add-back" mode. This technique allows in the case of a Compton-scattered γ ray in one crystal to restore its full energy partially deposed in a neighbouring crystal. Due to the possibility to add back the energies measured in neighbouring crystals, a high full energy efficiency is maintained up to γ-ray energies of several MeV [Wil1996]. Therefore, the Ge-Cluster detectors are ideally suited for the fast beam RISING experiments, where the γ-ray energies are strongly Doppler shifted to higher energies. For experiments

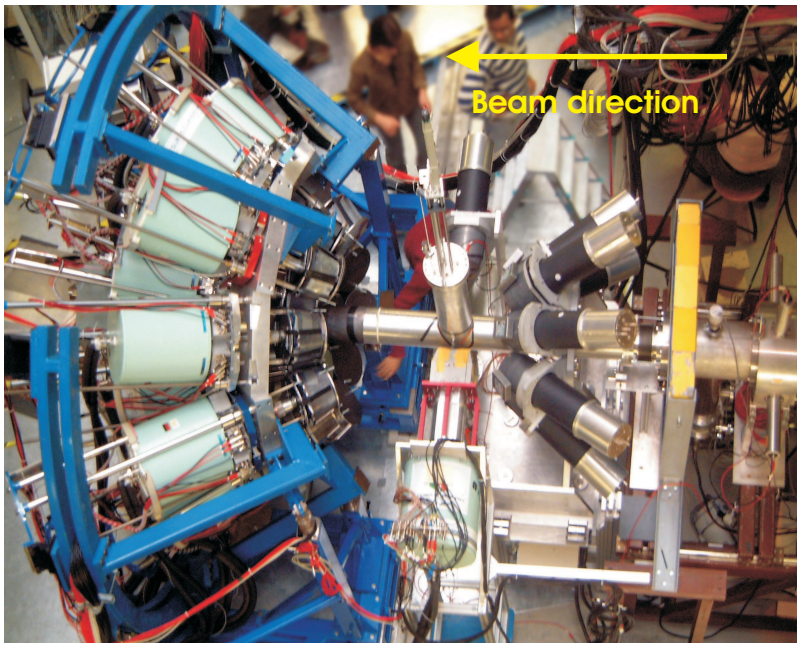

Figure 4.28: The RISING Ge cluster detectors located downstream from the secondary target.

with beam energies around 100 A·MeV the Ge-Clusters have to be positioned at forward angles in order to maximize the effective solid angle affected by the Lorentz boost, and to minimize the Doppler broadening effect, as it was discussed in the previous section.

A design goal for the array was to obtain about 1% energy resolution for a γ transition emitted from a nucleus moving at $\beta = 0.43$. It was this criterion that defined the distance to the target and the angular geometrical configuration. According to several design calculations [Sim2002], in order to achieve this goal the Cluster detectors without BGO shields (as normally operated in EUROBALL set-ups) should be arranged in 3 rings around the beam line with the axis of the central detectors in each ring positioned at 16°, 33° and 36° (see Figure 4.29).

In this respect, Table 4.1 shows the calculated performance of the RISING array (2003 campaign) assuming a 1.3 MeV γ ray emitted from a nucleus moving at $\beta = 0.43$. In these calculations the velocity spread in the target is ignored.

The resolution of the detectors in the 2^{nd} and 3^{rd} rings at a distance of 700 mm are worse than 1%. Therefore, the array was designed such that these detectors could be positioned at a variable distance from the target from 700 mm to 1400 mm obtaining thus the desirable 1% energy resolution. However, the detector configuration to be chosen depends on the relative importance of efficiency to energy resolution to achieve the physics goal of a particular experiment.
In the case of ^{108,112}Sn experiment, all Ge-Clusters were positioned at 700 mm distance from the target.

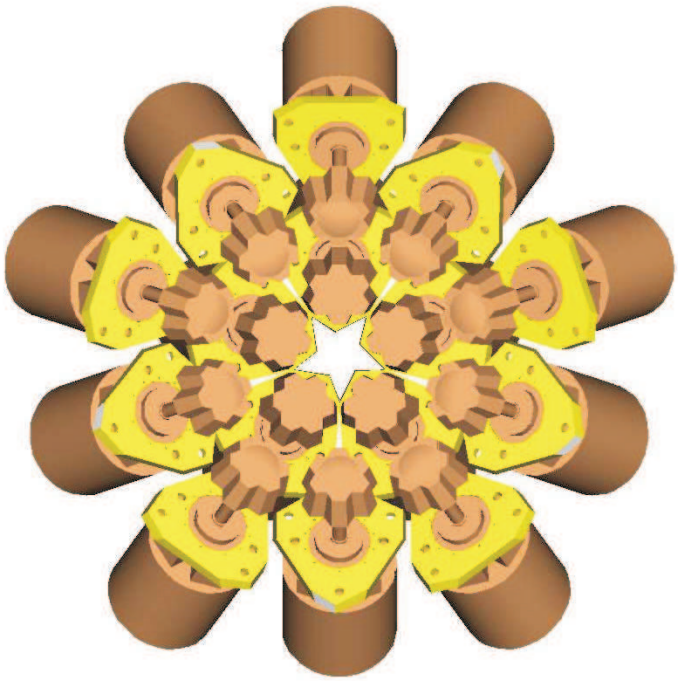

Figure 4.29: Configuration of the 15 Ge-Cluster detectors for experiments with relativistic beams of 100 A·MeV.

Table 4.1: Performance of an array of Ge detectors at the closest position and at a position optimized for energy resolution of 1%.

Ring	distance [mm]	energy resolution (calculated) [%]	efficiency (calculated) [%]
1	700	1.00	1.00
2	700	1.82	0.91
3	700	1.93	0.89
Total Clusters		**1.56**	**2.81**
1	700	1.00	1.00
2	1295	1.01	0.28
3	1372	1.01	0.24
Total Clusters		**1.00**	**1.52**

To reduce the contribution from environmental radiation and the atomic background radiation from the target, each Cluster detector was surrounded on the side by lead sheet of 2 mm thickness, and shielded in the front a combination of Pb (1 mm), Sn (2 mm) and Al (2 mm) absorbers.

4.7.3 Electronics

Ge detector read-out electronics: As it was described in the previous section the γ-ray detection system in RISING consists of 15 Ge-Cluster detectors. Each Ge-Cluster is readout by a VXI EUROBALL card which permits the implementation of both analogue (amplifiers, ADCs) and logical (TFAs, CFDs, TACs) electronics in the same chassis. Detailed information about the EUROBALL electronic system can be found in [Laz1992].
In Figure 4.30, it is schematically drawn the configuration of the VXI readout hardware implemented for the ^{108,112}Sn experiment. Two VXI crates were used during the measurement. In the first crate 5 VXI EUROBALL cards were engaged, while in the second crate the other 10 EUROBALL cards.

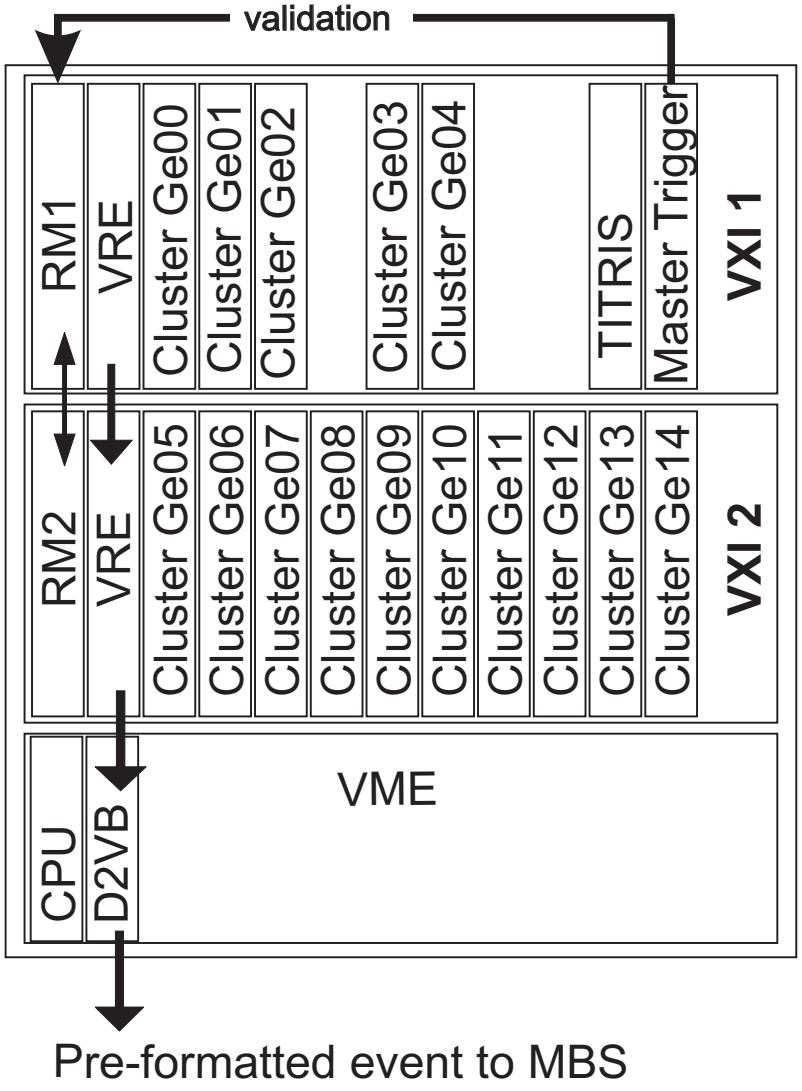

Figure 4.30: VXI readout hardware configuration used during the ^{108,112}Sn experiment.

In a single crate, up to 13 VXI cards can be located: two of these cards are "infrastructure" cards [Laz1992] – the Slot 0 controller (Resource Manager) and the crate readout card (VXI Readout Engine - VRE), the remaining 11 slots are usable for detector electronics although 1 slot in one crate must be allocated to the system Master Trigger card.

The Resource Manager card contains a VME CPU which connects to a network (e.g., ethernet) to give the software access to each VXI crate. This CPU runs the VXI crate configuration software when the VXI crate is initialized, and has access via the RM/Slot 0 controller to all VXI signals. The Master Trigger card generates the system trigger pulse and distributes system control signals (stop/go, inhibit, read scalers,...) to each VXI crate. The Cluster Ge card is designed to instrument 7 Ge channels plus 1 spare. As aforementioned, such a card provides whole the signal processing necessary to generate energy and timing data using the Ge-Cluster preamplifier signals as inputs.

Each VXI crate reads data in parallel and writes it into the buffered crate readout card (VRE) where it is stored. All crate readout cards are linked into a daisy chain configuration and perform hardware event building by assembling all fragments[4] of an event before writing validated data by the trigger pulse into a single event collector VME buffer memory (D2VB in Figure 4.30).
Afterwards, the γ event is formatted so that is accepted by the GSI standard data acquisition system MBS (see next section).

All important parameters related to the Ge signals are computer controlled within the VXI cards by using the MIDAS software packet [Puc1995].

The TITRIS-clock module is used for time stamping every Ge event for every valid trigger signal sent to the TITRIS module.

4.8 Data Acquisition and Trigger

Data acquisition and control system

RISING is a combination of three independent detector systems: the EUROBALL Ge-Cluster detectors, the HECTOR[5] array and the FRS detectors including the CATE detector array. Each of these systems has an individual data acquisition (DAQ) producing independent events. To assemble them in a common event stream, a time stamping technique for event synchronization, was developed in

[4] In our case, the two sub-events corresponding to each of the two VXI crates.

[5] Eight large volume BaF_2 scintillators (part of the HECTOR array [Maj1994]) are placed in the RISING set-up, exploiting their good time resolution ($\approx 1ns$) and high detection efficiency, complementing thus the Ge-Cluster detectors. This γ-detection array was not substantially used during the experiment studied by this work.

the framework of the GSI standard DAQ system, MBS [Ess1996]. Each of the three subsystems is equipped with a newly developed VME time stamp module, TITRIS [Hof2002], which produces a single buffered 48 bit time stamp with 20 ns granularity per bit on each external trigger signal. The design of the time stamp system allows for an integration of up to 16 TITRIS modules in a system, among all one TITRIS module is arbitrarily chosen to be a master, while all the other are slaves. The master module sends regularly synchronization pulses to all slave modules, keeping thus all modules on the same time base.
Thanks to this approach it is possible to keep most of original components of the RISING subsystems in operation; they still run independently and are fully operational DAQ systems with individual trigger sources and produce their local dead times.

Collecting and sorting the data from all three subsystems is done by an additional MBS system, which does manly, connecting to the subsystems data output via TCP sockets, sorting all events according to their time stamps, and formatting all events into the output buffer for data logging and online monitoring purposes. It is the task of the data analysis to pick out the time sorted sub-events and combine them into a real physical event using an appropriate synchronization criterion.

The Ge-Cluster detector signals are processed by the VXI Ge-Cluster cards providing 4 MeV and 20 MeV energy ranges and γ-ray time with respect to the VXI trigger. As mentioned in the previous section, the cards are readout by the VXI Readout Engine (VRE) and sent to a VME processor on which a new program developed for RISING sends event data in large data blocks via TCP sockets to an MBS event-builder PC. This event-builder receives the data, converts it into the MBS format and provides it for further processing like data logging, online monitoring and most importantly as a data source for the RISING master event-builder.
The DAQ system for FRS/CATE and HECTOR are structurally identical MBS systems. A VME crate contains a RIO3 readout processor, a GSI trigger module, the TITRIS time stamping module and digitizers, QDCs, ADCs, TDCs, scaler.
All this are depicted in the schematic diagram of the RISING DAQ system shown in Figure 4.31.

In order to check online the event synchronization among the three data streams aforementioned, an analog signal with 8 amplitudes was produced by feeding Time Calibrator (ORTEC 462, period = $0.16\mu s$, range = $1.28\mu s$) signals into a TAC (time-to-amplitude converter). The analog signal was further fed into 3 ADCs, each belonging to one of the three branches (VXI-branch, FRS-branch and HECTOR-branch). The 'gate' signal for reading out ADC data was determined by one of the Time Calibrator signals, which was used as a trigger for each of the three data acquisition branches. All this are schematically presented in Figure 4.32.

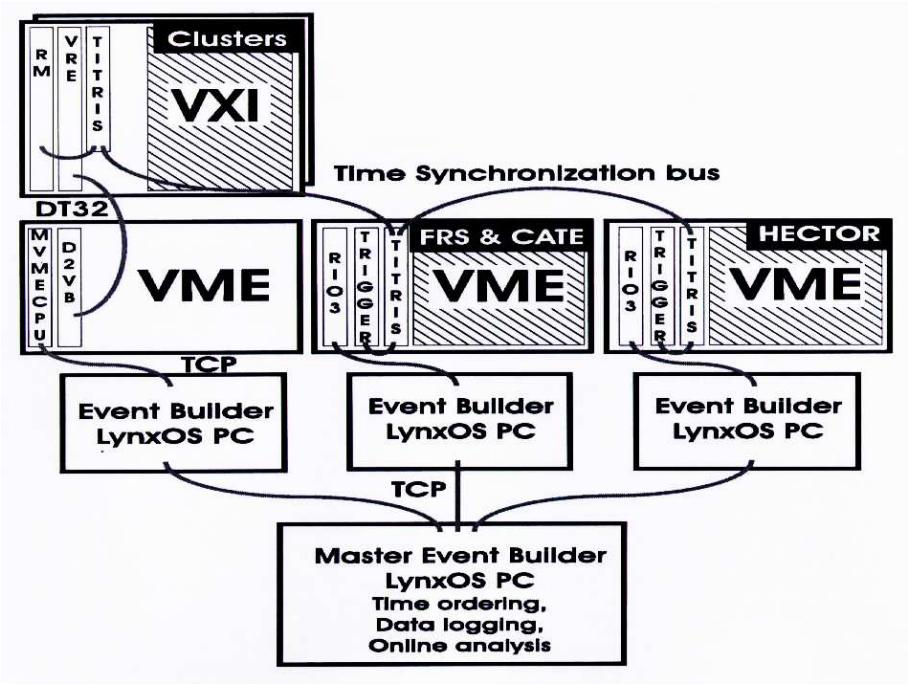

Figure 4.31: Block diagram of the RISING DAQ system.

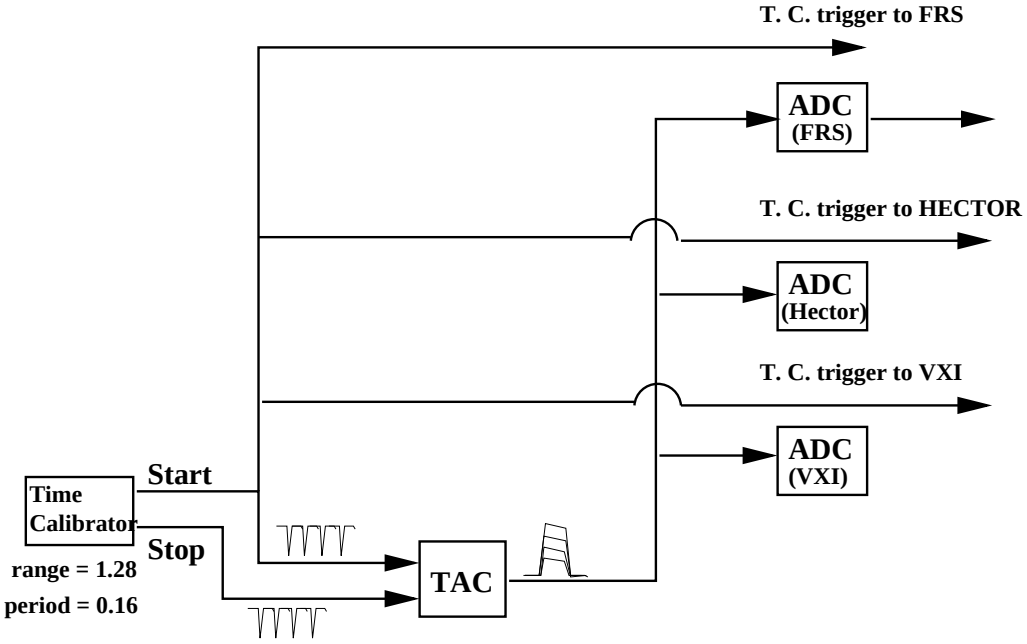

Figure 4.32: Time calibrator trigger (electronic scheme): T.C. - Time Calibrator.

Standard histograms used for the online event synchronization are two-dimensional spectra plotting the ADC (TAC) information in one branch versus the ADC (TAC) information in the other branch. Thus there are three such plots in the case of correlating data from three branches. The 2D-histograms show a pattern of points on a diagonal line symmetric with respect to the coordinate axes since the same

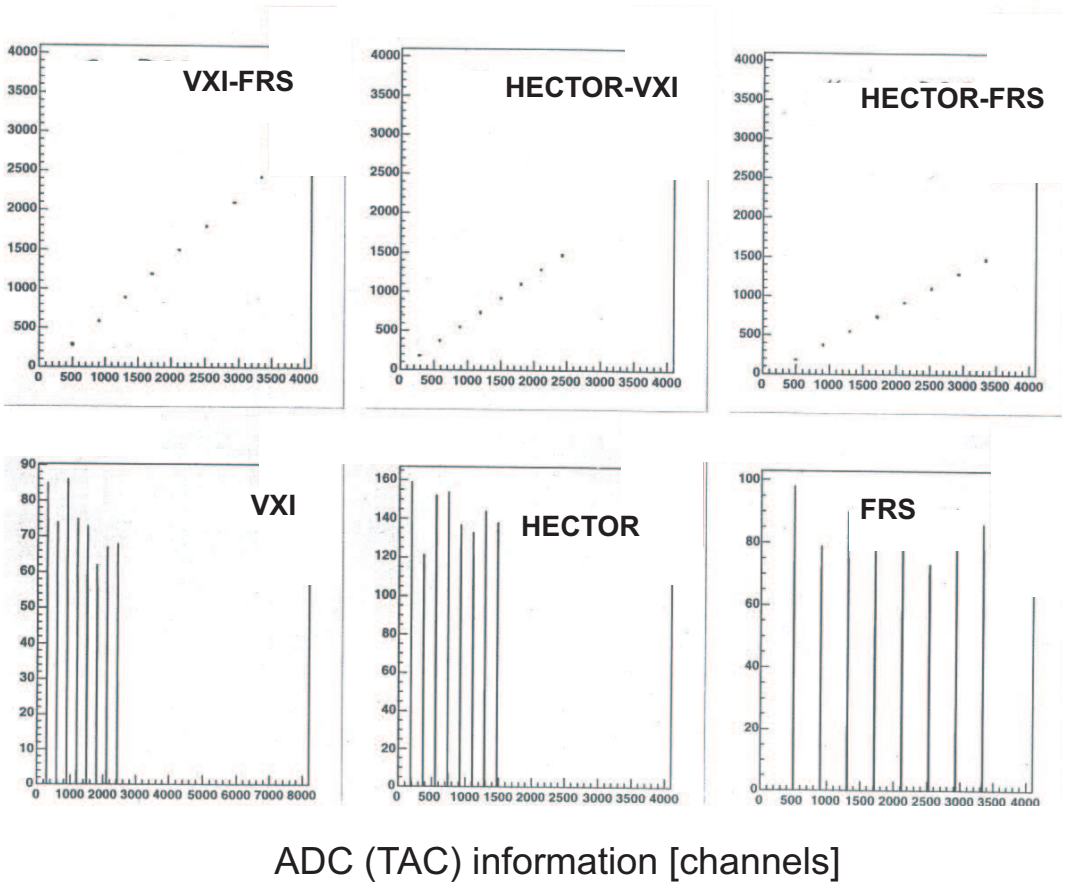

Figure 4.33: Online even synchronization spectra (upper panel). Time Calibrator ADC/TAC spectra for the three branches (FRS, VXI, HECTOR). The eight peaks correspond to a period of 0.16 μs and a range of 1.28 μs for the Time Calibrator settings.

information is plotted basically on both axes. The frequency of the chain of points on the diagonal line is determined by the period of the Time Calibrator. An indication of synchronization lost is given in this case by the distortion of the diagonal pattern. In Figure 4.33 the three correlation plots of the three data streams are shown in the upper panel, while the analog signal generated by the combination between Time Calibrator and TAC is shown in the lower panel. Here the eight peaks correspond to aforementioned period and range of the Time Calibrator.

Trigger

Three types of physics triggers were implemented with the SCI2[6] timing signal:

- SCI2 and at least one γ ray in any Ge crystal in coincidence, triggering both VXI and FRS/CATE data acquisition systems – **particle-γ trigger**;

[6]Time-of-flight detector at the final focal plane of the FRS (see Section 4.3).

- SCI2 and at least one γ ray in the HECTOR array, triggering both FRS/CATE and HECTOR data acquisitions – **particle-γ trigger**;
- Scaled down SCI2, so-called "FRS reduced trigger" used to count the number of incoming beam particles – **scaled down particle-singles trigger**.

During the FRS detector calibration runs, the SCI2 timing signal (without being scaled down) is used as trigger. In the case of Ge detector energy calibration and for control purposes, γ-singles trigger[7] is used.

In addition, as discussed in the last section, for online event synchronization monitoring, a low frequency pulser (Time Calibrator) was superimposed on the physical triggers in each of the three data acquisition systems (VXI, FRS/CATE and HECTOR) in RISING.

Figure 4.34 shows schematically the concept of the electronic scheme[8] for the RISING triggers. See [Sai2003] for more information.

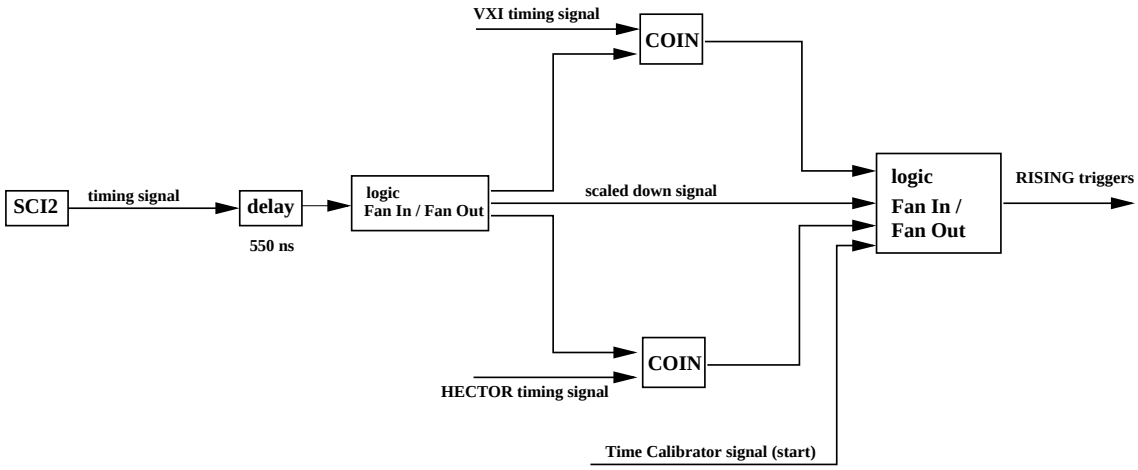

Figure 4.34: The concept of the RISING trigger scheme.

4.9 Data summary

The experimental conditions for the measurements on ^{108,112}Sn are summarized in Table 4.2.

[7]Internal VXI trigger related to the time of the first Ge crystal fired, unlike the VXI trigger related to an external signal (SCI2 timing signal) as used in RISING production runs.

[8]This scheme was valid for the experiments performed in October 2003.

Table 4.2: Experimental parameters for the Coulomb excitation measurements on ^{108,112}Sn

Primary beam	^{124}Xe	^{124}Xe
SIS energy (A·MeV)	700	700
Primary beam intensity (s^{-1})	$\approx 6\times10^{7}$	$\approx 6\times10^{7}$
Secondary beam of interest	^{112}Sn	^{108}Sn
Secondary beam of interest abundance (%)	≈ 60	≈ 62
Secondary beam of interest intensity (s^{-1}) (at the reaction target)	2400	2480
Secondary beam of interest energy (A·MeV) (at the reaction target)	147	142
γ ray of interest (keV) ($2_1^+ \rightarrow 0^+$)	1257	1206
Data collection time (h)	33	58

Note that the two intermediate-energy Coulomb excitation measurements on ^{108}Sn and ^{112}Sn are performed under similar experimental conditions. Hence, it justifies to determine unknown B(E2) value in ^{108}Sn relative to the known value in ^{112}Sn.

Chapter 5

Analysis and Results

This chapter is structured so that the data analysis procedure describing the most important steps taken in the analysis is presented first, leaving the presentation of the experimental results at the end.

5.1 Analysis procedure

The basic concept of the data analysis can be described as follows:

- isotope selection before the target by FRS;
- isotope selection behind the target by CATE;
- prompt gamma time 'window' condition;
- gamma multiplicity $M_\gamma = 1$;
- scattering angle condition.

In the following, the items of the analysis procedure are discussed in detail.

5.1.1 Isotope selection

As a necessary requirement for tagging a Coulomb scattering reaction, the incident reaction channel must be identical with the final reaction channel.

In our case we are interested to select the isotopes ^{108}Sn and ^{112}Sn, which undergo a Coulomb excitation reaction on a gold target.

Before the target the two tin isotopes are uniquely identified in mass number A and nuclear charge Z by the FRS detectors. Typical identification plots are shown in the Figure 5.1.

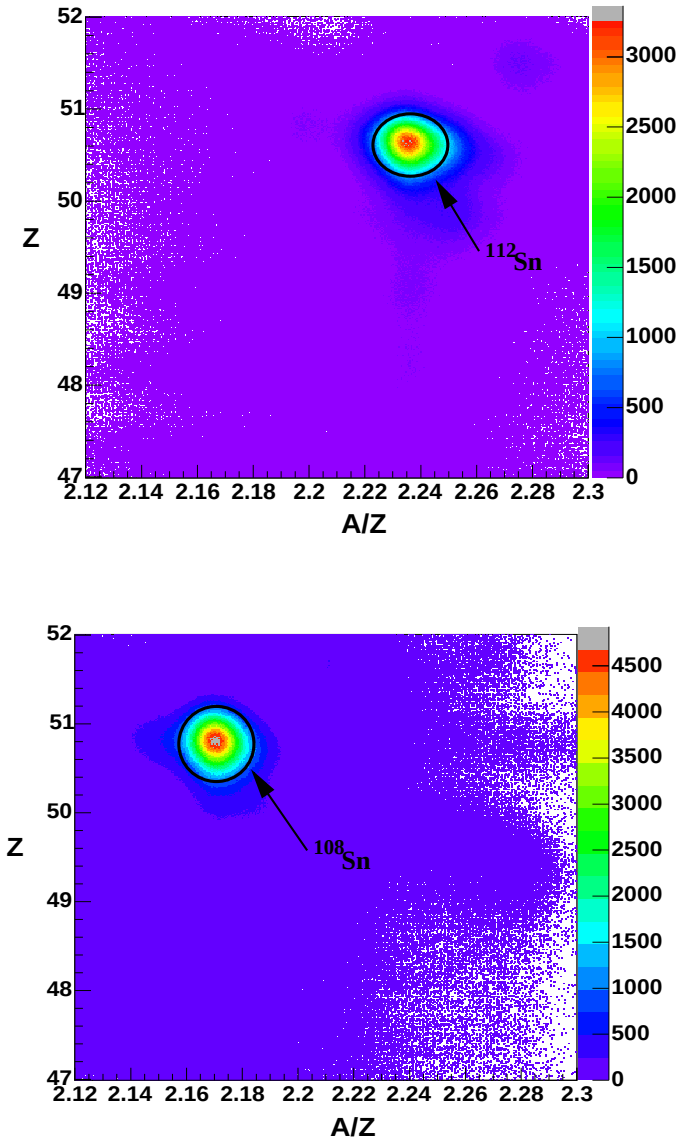

Figure 5.1: Identification of ^{112}Sn (upper plot) and ^{108}Sn (lower plot) before the reaction target.

After the target, the isotope identification is based on information provided by the calorimeter telescope CATE which has a good resolution in nuclear charge Z. With respect to mass, resolution is more difficult to be achieved for the reasons mentioned in Section 4.6. Figure 5.2 shows the identification plot in the case of ^{112}Sn measurement. The identification plot is similar for the measurement on ^{108}Sn.

By using selection 'gates' like the ones illustrated in Figure 5.2, one does not exclude reaction channels as for example - 1n, 2n knock-out. However, the probability for such processes to occur is far smaller than the Coulomb excitation probability that

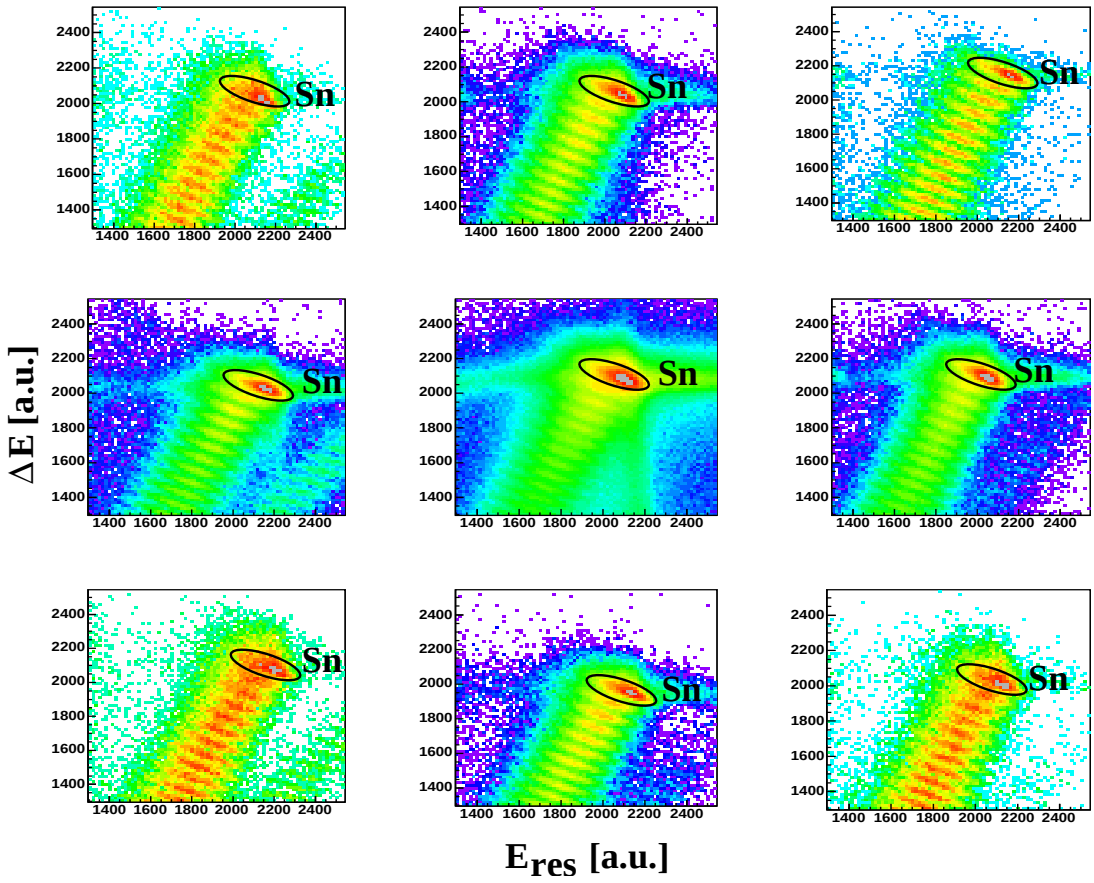

Figure 5.2: Typical identification plot behind the reaction target using CATE. Here $E_{res} - \Delta E$ histograms correspond to ^{112}Sn case. Similar results are obtained for ^{108}Sn.

one can neglect them. Therefore, the isotope selection only by Z is sufficient in this case. This has been also proven in the analysis by narrowing the size of the $E_{res}-\Delta E$ gates to correspond only to the most intense distribution of the Sn isotopes. The obtained results remained the same within experimental uncertainties.

5.1.2 Gamma ray analysis

Detector calibrations

The Ge-Cluster detectors were calibrated in energy by using a ^{152}Eu γ-ray source. An add-back procedure (applied to all 7 crystal within a Ge-Cluster) as well as Doppler-shift correction were performed event by event. By the add-back procedure a factor of $\approx$ 17 % was gained in the gamma detection for the $\simeq$ 1.2 MeV energy of the first excited 2^+ state in ^{108,112}Sn.

Doppler shift correction

One of the variables that enters in the Doppler shift correction formula is the velocity factor β. As discussed in Chapter 4, in the case of fragment beams the velocity distributions are rather broad mainly due to the fragmentation mechanism itself or processes like angular straggling in matter. In order to minimize the experimental uncertainties, an accurate measurement of the fragment velocity, on a event-by-event basis, is necessary.

Velocity factor determination: In Section 4.3 it was mentioned that for a given flight path, the fragment velocity measurement is actually a time-of-flight measurement. However, this method has a certain limitation which comes from the fact that there is matter in between the two TOF detectors, respectively, an Al wedge energy degrader, two multiwire proportional chambers and the ionization chamber MUSIC. The presence of these detectors, of course, alters the accuracy of the velocity determination. A way out to this problem is to take into consideration the energy loss in the associated FRS detectors. When the fragments pass through the FRS there is no loss of energy, the velocity being accurately measured by knowing the $B\rho$ settings of the last two dipole magnets. To determine the energy loss in the detectors placed before the target, one may use the code ATIMA [Sch1998a], which calculates various physical quantities characterizing the slowing-down of heavy ions in matter. The input parameters for the ATIMA code are the charge Z and mass A of the fragment of interest, its initial kinetic energy, and the thickness of the matter for which the energy loss is to be calculated. The code returns the fragment kinetic energy after passing that matter, and furthermore, the corresponding velocity. However, the calculated value corresponds only to the centroid of the Gaussian-like fragment velocity distribution. In order to determine the velocity on an event-by-event basis, ideally it would be to couple the ATIMA code to the data analysis. Thus, for each event the velocity after the FRS magnets is taken as an input parameter to ATIMA, which in turn would calculate the fragment velocity before the target taking into account the energy losses in the associated FRS detectors. Since this is not so trivial to be implemented, a much simpler solution was found in our case.

Figure 5.3 shows the velocity distribution of the ^{112}Sn fragments after the FRS magnets[1], calculated event by event as follows:

$$\beta\gamma = (B\rho)_2 \frac{Z}{A}\frac{1}{uc}, \text{ with } A = 112 \text{ and } Z = 50,$$

$(B\rho)_2$ being the average rigidity in the second half of the FRS. Hence, the velocity of the ^{112}Sn fragments after the FRS magnets is deduced, event by event, with the help of the expression:

$$\beta_{after\ FRS\ magnets} = \frac{\beta\gamma}{\sqrt{1+(\beta\gamma)^2}}.$$

[1]The fragment velocity after the last quadrupole magnet at the exit of the FRS spectrometer.

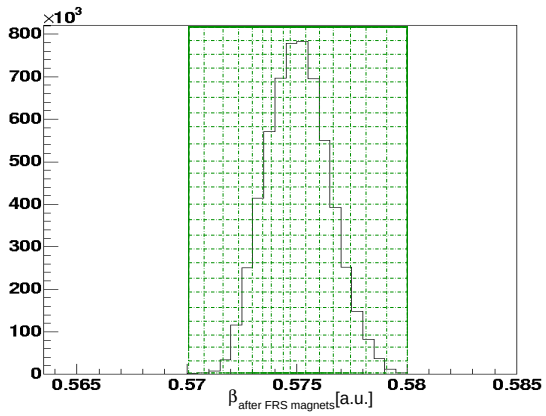

Figure 5.3: Fragment velocity distribution after the FRS magnets for the ^{112}Sn case. The hatched area was used as input velocity range for ATIMA calculations.

The hatched area in Figure 5.3 corresponds to the range of fragment velocities used as input parameters to ATIMA code in order to perform iterative calculations for the velocity losses. As a result, a theoretical relationship was determined between the fragment velocity at the exit of the FRS and the velocity lost by the fragments in the detectors placed before the reaction target.

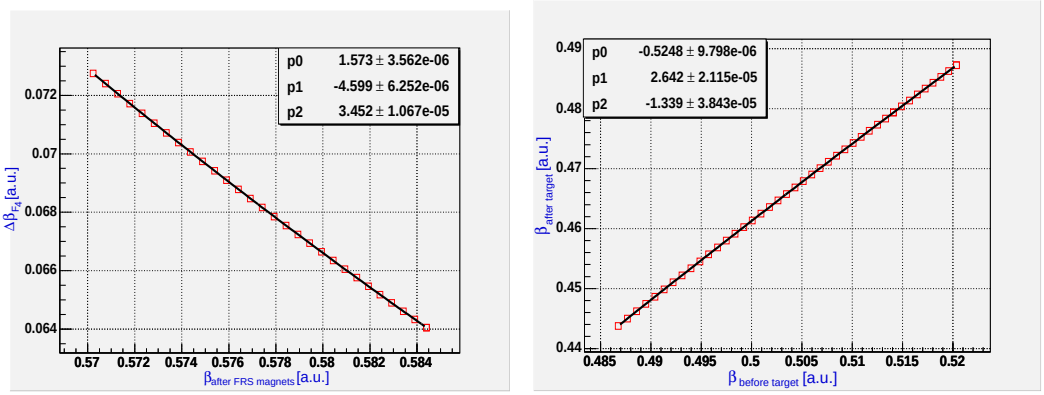

Figure 5.4: A fit of the dependence between the fragment velocity at the exit of the FRS and the velocity loss of the fragments in the FRS detectors before the target (left). A fit between the fragment velocity before and after the target (right).

By fitting the distribution in Figure 5.4 (left) with a polynomial function of second order, the following relationship is obtained:

$$\Delta\beta_{F_4} = 1.57 - 4.60 \cdot \beta_{after\ FRS\ magnets} + 3.45 \cdot \beta^2_{after\ FRS\ magnets}.$$

This expression is used further to determine event by event the fragment velocity before the target as the difference between the velocity at the exit of the FRS and the velocity loss:

$$\beta_{before\ target} = \beta_{after\ FRS\ magnets} - \Delta\beta_{F_4}.$$

A similar procedure is applied to determine on an event-by-event basis the fragment velocity after the target (the velocity used in the Doppler-shift correction formula). The following relationship was obtained after fitting the velocity distribution plotted in Figure 5.4 (right):

$$\beta_{after\ target} = -0.53 + 2.64 \cdot \beta_{before\ target} - 1.34 \cdot \beta^2_{before\ target}.$$

The histograms of the velocity distributions before and after the target are shown in Figure 5.5. Because the velocity after the target enters as a direct parameter in the Doppler shift correction formula (see Section 4.7), the measured velocity resolution is an important number contributing to the energy resolution of the γ-ray energies of interest.

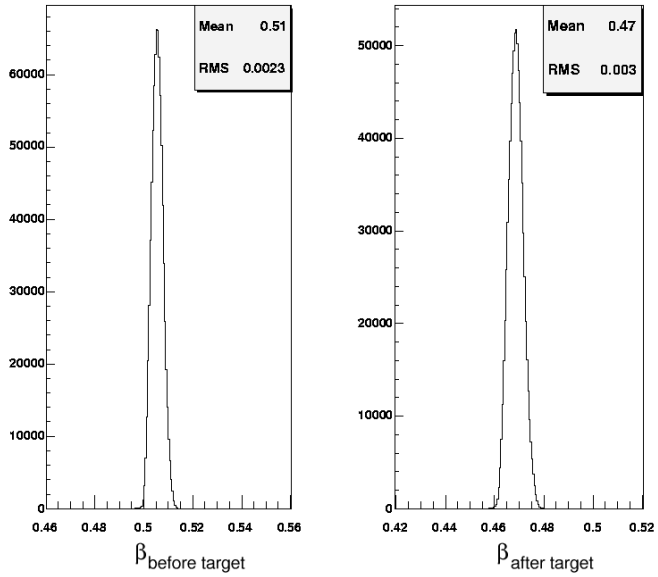

Figure 5.5: Velocity distributions before (left) and after (right) the target, in the case of ^{112}Sn. The corresponding velocity resolutions (RMS) are approximately 0.5% and 0.6%, respectively.

Gamma analysis conditions

There are two important conditions applied in the data analysis in order to observe the γ-ray lines of interest, otherwise dominated by huge atomic background radiation and "chance coincidences" γ events[2]. These conditions are the following:

- Prompt gamma radiation time condition;
- Gamma hit multiplicity.

[2]This is radiation originating from atomic processes.

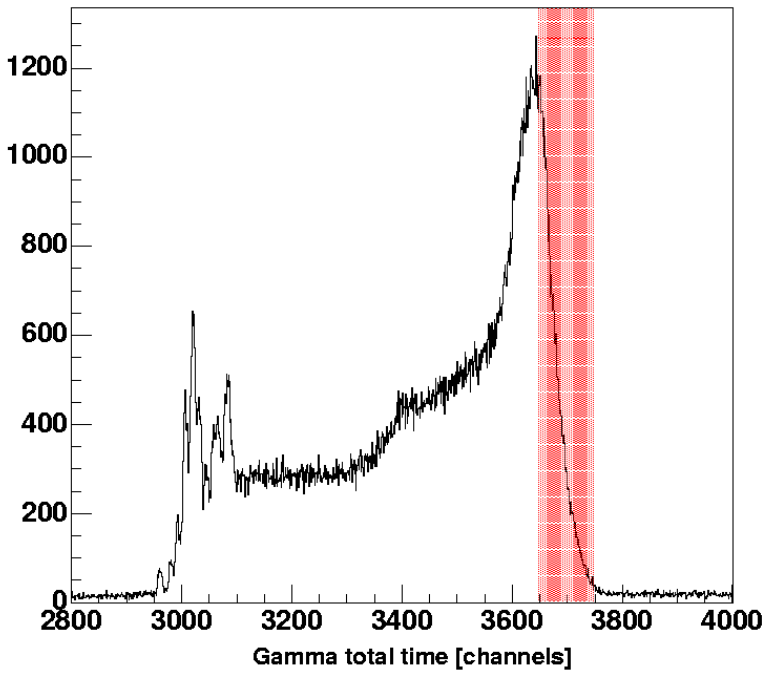

Figure 5.6: Ge-Cluster sum time spectrum. The hatched area corresponds to the prompt gamma radiation emitted mainly from the target.

Following it is explained the prompt gamma radiation time condition corresponding to the hatched area in Figure 5.6 which shows the histogram of the Ge-Cluster sum time spectrum. For simplicity, the explanation refers to the ^{112}Sn data but it was found to hold for ^{108}Sn data, too.
The strong peak in the time distribution was initially interpreted as corresponding to prompt gamma radiation emitted mainly from the target. Detailed analysis discussed below showed that this very wide time peak corresponds also to radiation originated from detectors upstream from the target. Since applying a wide time gate in the analysis of the gamma energy spectra it would lead to a poor peak-to-background ratio, it was investigated what would be the proper time range corresponding to prompt γ rays emitted merely from the target.

Figures 5.7 and 5.8 show the effect of several time conditions on the γ-ray energy peak corresponding to the transition $2_1^+ \rightarrow 0^+$ in the Coulomb excited ^{112}Sn isotope.

Each of the experimental data points plotted in the Figure 5.7 represents the Coulomb excitation photon yield corresponding to the energy peak at 1257 keV. The time conditions shown were varied by narrowing the time window in steps of 10 channels, beginning with the widest channel interval initially thought to correspond to prompt γ rays emitted from the target.

The Doppler-shift corrected gamma energy spectra displayed in the Figure 5.8 are obtained by applying the same time conditions as shown in Figure 5.7.

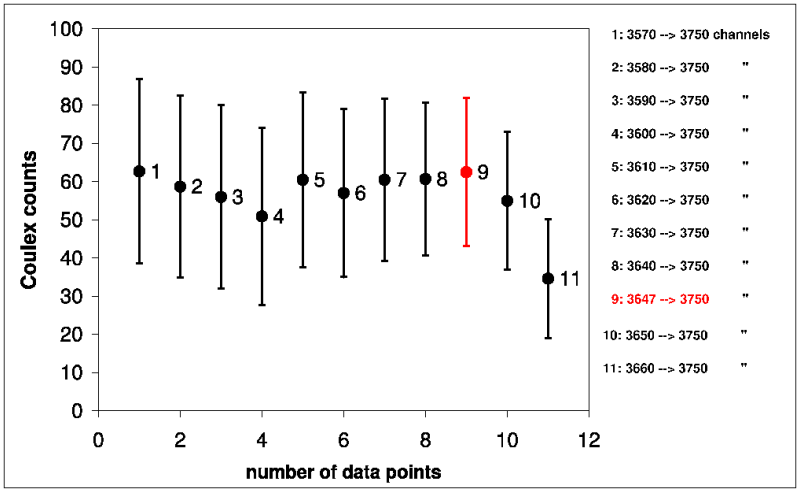

Figure 5.7: Systematics of Coulomb excitation peak area integral for several prompt gamma radiation time conditions corresponding to the Ge-Cluster sum time spectrum. The time condition plotted in red was the one finally used in the data analysis.

The idea behind this analysis was to investigate how the peak-to-background ratio changes with the time condition while the integral of the Coulomb excitation peak remains constant. Hence, it was found that by narrowing the time condition the peak-to-background ratio is improved systematically. However, for a gamma time window corresponding to *the time condition 11* (see Figure 5.7), the Coulomb excitation photon yield is reduced with respect to the photon yields corresponding to the other time conditions.
Finally, *the condition 9: 3647→3750* – plotted in red in the Figure 5.7, shows the optimum peak-to-background ratio (see Figure 5.8). It was this *prompt gamma radiation time condition* that was used in the data analyses of both ^{112,108}Sn isotopes, as illustrated by the hatched area in Figure 5.6. Taking into account the time calibration factor of 0.25 ns/channel [Bed2003], the condition corresponds to a time range of approximatively 26 ns.

The other gamma analysis condition is the *Gamma hit multiplicity* condition, which here refers to how many Ge-Cluster detectors are fired within one accepted particle-gamma event. Roughly speaking, the Coulomb interaction time in a relativistic heavy-ion collision is so short that one expects that at most one virtual photon can be exchanged. Thus, considering that the intermediate-energy Coulomb excitation is predominantly an *one-step process*, it implies a γ-hit multiplicity equal to one. However, there is a large probability that a de-excitation event is accompanied via chance coincidences by radiation originating from atomic processes. Therefore, for an appropriate Coulomb excitation event selection, it has to be required in the analysis that the condition of single γ-hit cluster multiplicity[3] is satisfied only for prompt γ rays at energies in excess of 500 keV (in laboratory frame). This excludes non-suppressed atomic background radiation produced at the used beam energy.

[3]Here it is taken into consideration that add-backing procedure is applied.

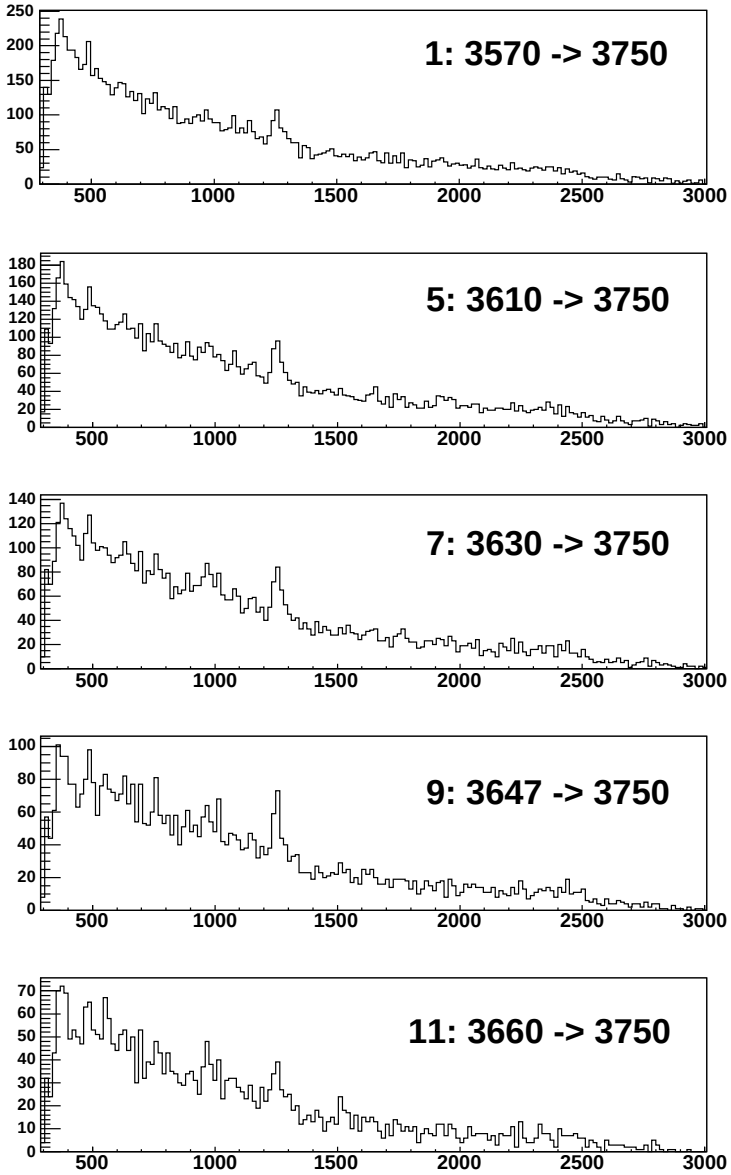

Figure 5.8: Doppler-shift corrected gamma energy spectra corresponding to different prompt gamma time conditions. Note that the peak-to-background ration improves by narrowing the range of the time conditions.

5.1.3 Scattering angle condition

As discussed at the beginning in Section 3.3, in tagging an intermediate-energy Coulomb excitation event, the condition that the same reaction channel is selected before and after the target is a necessary condition however not sufficient. In Figure 5.9 are shown several Doppler-shift corrected gamma energy spectra created under different scattering angle[4] conditions. To be consistent with previous presentations, the discussion here refers to ^{112}Sn, too. In Section 4.5, it was discussed that

[4]The scattering angle is calculated in the laboratory frame.

in RISING one cannot measure the projectile residue scattering angle better than 0.5° due to angular straggling in the target amounting to 8 mrad. This is the reason why the scattering angle conditions in Figure 5.9 are varied in steps of 0.5°. The first two spectra show only a weak indication of the 1257 keV γ ray de-exciting the first excited 2^+ state, the corresponding scattering angle intervals being dominated by the elastic scattering and atomic excitation processes. However, above 1° the Coulomb excitation peak shows up, being yet weakened for scattering angles larger than 2° when the nuclear excitation contribution becomes dominant.
Hence, the requested scattering angle condition in the analysis was between 1°–2°. Above this range one expects nuclear interactions to contribute, while below the elastic channel dominates resulting in increased atomic background.

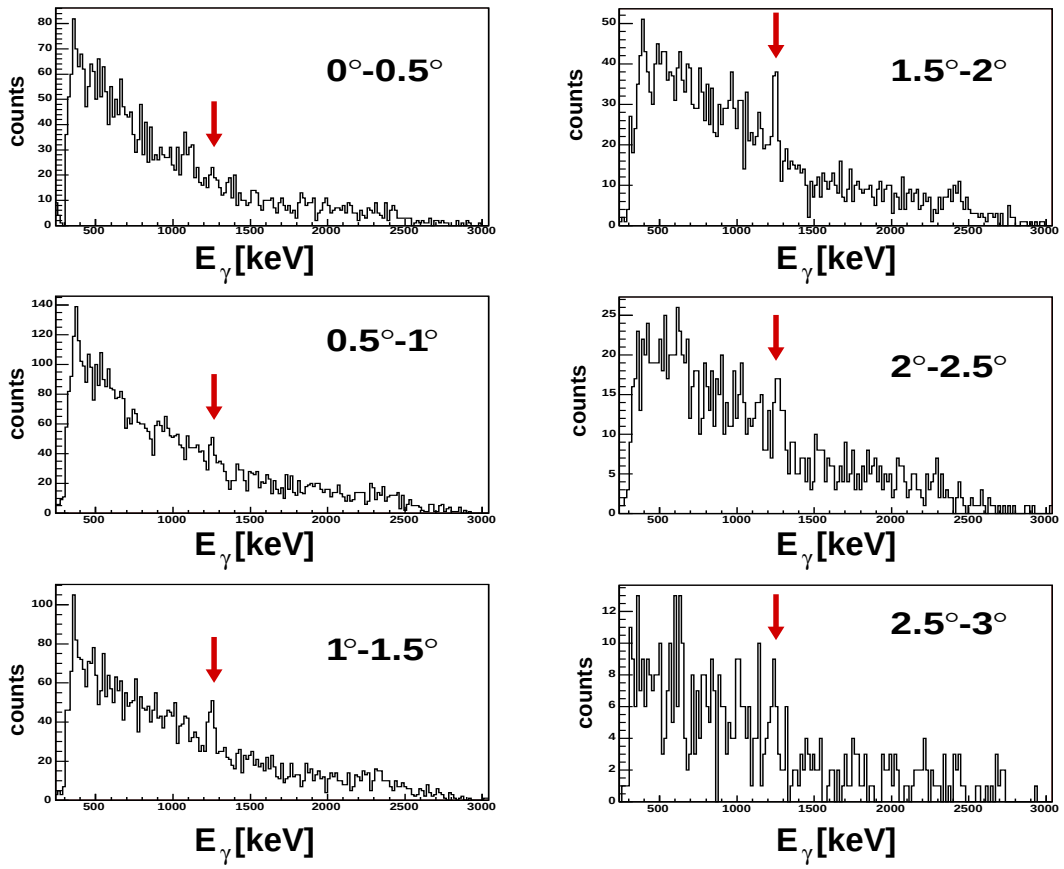

Figure 5.9: Doppler-shift corrected gamma energy spectra created under different scattering angle conditions, for the case of ^{112}Sn .

The same scattering angle condition was applied for ^{108}Sn case in order to facilitate its $B(E2)$ value measurement by normalization to ^{112}Sn.

"Crate-wise" data analysis

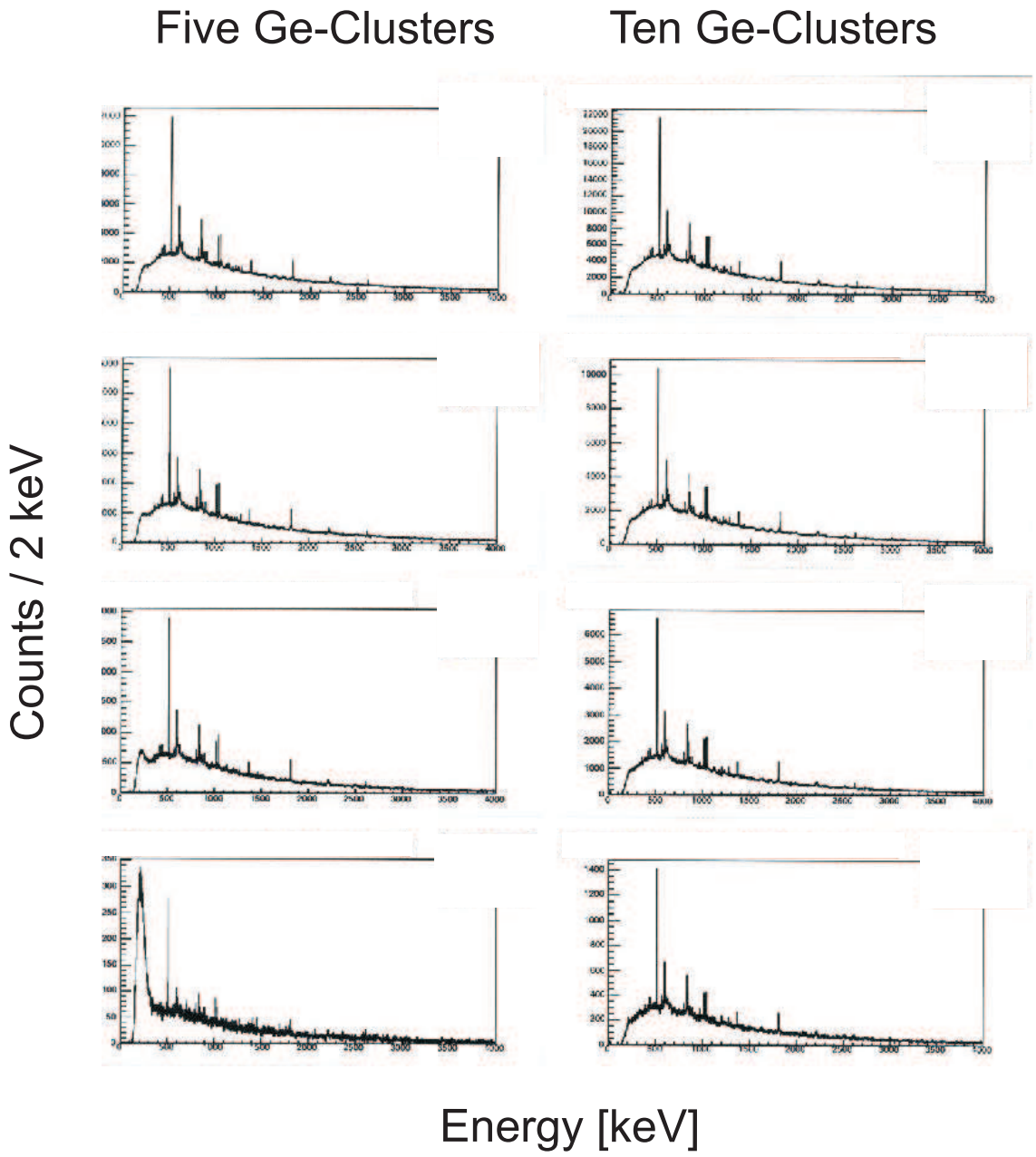

Figure 5.10: "Crate-wise" data analysis results for the case of ^{112}Sn. On the left-hand side are shown non-Doppler corrected gamma energy spectra corresponding to 5 Ge-Clusters data, while on the right-hand side the corresponding spectra for 10 Ge-Cluster data. These spectra are created under different particle conditions applied successively – first no particle conditions, followed by isotope selection before the target, particle detection in CATE(Si), and isotope selection behind the target.

Here by "crate-wise" analysis one should understand that the gamma analysis was done separately for the 5 Ge-Cluster data corresponding to the Cluster Ge cards cards engaged in the first VXI crate and for the 10 Ge-Cluster data corresponding to the Cluster Ge cards in the second VXI crate (see Section 4.7). The reason behind

performing a "crate-wise" analysis is related to the fact that initially no Coulomb excitation γ-energy peaks were observed neither in ^{112}Sn measurement nor in ^{108}Sn. In the following, Figure 5.10 is explained: On the left-hand side are shown the data analysis results of the 5 Ge-Cluster detector data while on the right-hand side the corresponding results of the 10 Ge-Cluster data. The displayed gamma energy spectra are only calibrated but not Doppler-shift corrected. A prompt gamma radiation time condition is applied to all of them. The time condition here corresponds to the range of the strong time peak of the Ge-Cluster sum time spectrum presented in Figure 5.6. The histograms shown on top are created under the time condition only. In the following histograms, particle conditions are sequentially applied. At first only the $A/Z - Z$ isotope selection condition is requested, followed in the next histograms by an additional condition that particles are detected in the CATE(Si) detector array. At last in the histograms shown at the bottom, the $E_{res} - \Delta E$ isotope selection condition is applied, too.

The results of the "crate-wise" analysis show clearly that there was a problem with the 10 Ge-Cluster data. At first when no particle conditions are requested (histograms on top), both 5 and 10 Ge-Cluster energy spectra look similar, the spectra being dominated by "chance-coincidences" γ events. Unlike the histograms corresponding to the 5 Ge-Clusters, the histograms on the right-hand side exhibit no changes after applying several particle conditions. Only for the 5 Ge-Cluster data, the "chance-coincidences" are reduced considerably (histograms at the bottom), the strong energy peak at low energies corresponding to bremsstrahlung atomic radiation becoming thus visible.

Once this problem was encountered for both ^{112}Sn and ^{108}Sn runs, the data analyses were performed only for the 5 Ge-Cluster detector data . Therefore, throughout this chapter any reference to the gamma detection concerns only 5 RISING Ge-Cluster detectors out of fifteen as they are in total.

It is not understood yet what has caused the problem of the second VXI crate with 10 Cluster Ge cards, which clearly indicates that there is no particle-γ correlation between the two data streams, FRS and VXI. Although the synchronization between the three RISING data streams is monitored online during data taking, as explained earlier in the chapter, this problem could not be detected since the ADC channel used for checking the synchronization belonged to one of the Cluster Ge card engaged in the first VXI crate. Since then, the synchronization between gamma readout (VXI) and particle readout (FRS) was constantly monitored for both VXI crates by using an additional ADC channel.

5.2 Experimental results

In this section the data analysis results of the intermediate-energy Coulomb excitation measurements performed on ^{112}Sn and ^{108}Sn are presented.

From the observation of the Doppler corrected γ line corresponding to the $0^+_{\text{g.s.}} \rightarrow 2^+_1$ transition in ^{108}Sn, the Coulomb excitation cross section can be extracted, which is directly proportional to the B(E2) value [Win1979]. As discussed already in Section 3.3, an absolute Coulomb excitation cross section measurement is not feasible in our case. Therefore, following is presented the experimental result of a relative measurement of the $B(E2; 0^+_{\text{g.s.}} \rightarrow 2^+_1)$ value in ^{108}Sn. The known $B(E2; 0^+_{\text{g.s.}} \rightarrow 2^+_1)$ = 0.240 (14) e^2b^2 [Ram2001] was used as normalization.

The top panel in Figure 5.11 shows the Doppler corrected gamma energy spectrum of the excited ^{112}Sn, with the γ-ray line of interest at 1257 keV. The bottom panel shows the corresponding spectrum for ^{108}Sn with the γ-ray line at 1206 keV.

5.2.1 $B(E2; 0^+_{\text{g.s.}} \rightarrow 2^+_1)$ value in ^{108}Sn

The following mathematical expressions describe the relationship between the Coulomb excitation cross sections and the B(E2) values in ^{112}Sn and ^{108}Sn:

$$\begin{cases} \sigma^{108}_{E2} = f(b^{108}_{min}) \times [B(E2; 0^+ \rightarrow 2^+_1)]_{108} \\ \\ \sigma^{112}_{E2} = f(b^{112}_{min}) \times [B(E2; 0^+ \rightarrow 2^+_1)]_{112} \end{cases}$$

Hence, the B(E2)-value in ^{108}Sn can be determined as follows:

$$[B(E2; 0^+ \rightarrow 2^+_1)]_{108} = [B(E2; 0^+ \rightarrow 2^+_1)]_{112} \times \frac{\sigma^{108}_{E2}}{\sigma^{112}_{E2}} \times \frac{f(b^{112}_{min})}{f(b^{108}_{min})},$$

where the proportionality factor $f(b^{projectile}_{min})$ depends on projectile impact parameter as [Win1979]

$$f(b^{projectile}_{min}) = \frac{16\pi^2}{75}\Big(\frac{Z_{target}e^2}{\hbar c}\Big)^2\Big(\frac{1}{e \cdot b^{projectile}_{min}}\Big)^2.$$

Ratio $\sigma^{108}_{E2}/\sigma^{112}_{E2}$ determination

Experimentally, the Coulomb excitation cross section σ^{exp}_{E2} is defined as the ratio between the number of $0^+ \rightarrow 2^+_1$ excitations N_{E2} and the number of incoming beam particles N_p multiplied by the number of target nuclei per unit area N_t

$$\sigma^{exp}_{E2} = \frac{N_{E2}}{N_p \times N_t},$$

where the total number of Coulomb excitations N_{E2} is determined by dividing the number of detected photos N_γ by the total detection efficiency ϵ_{tot}

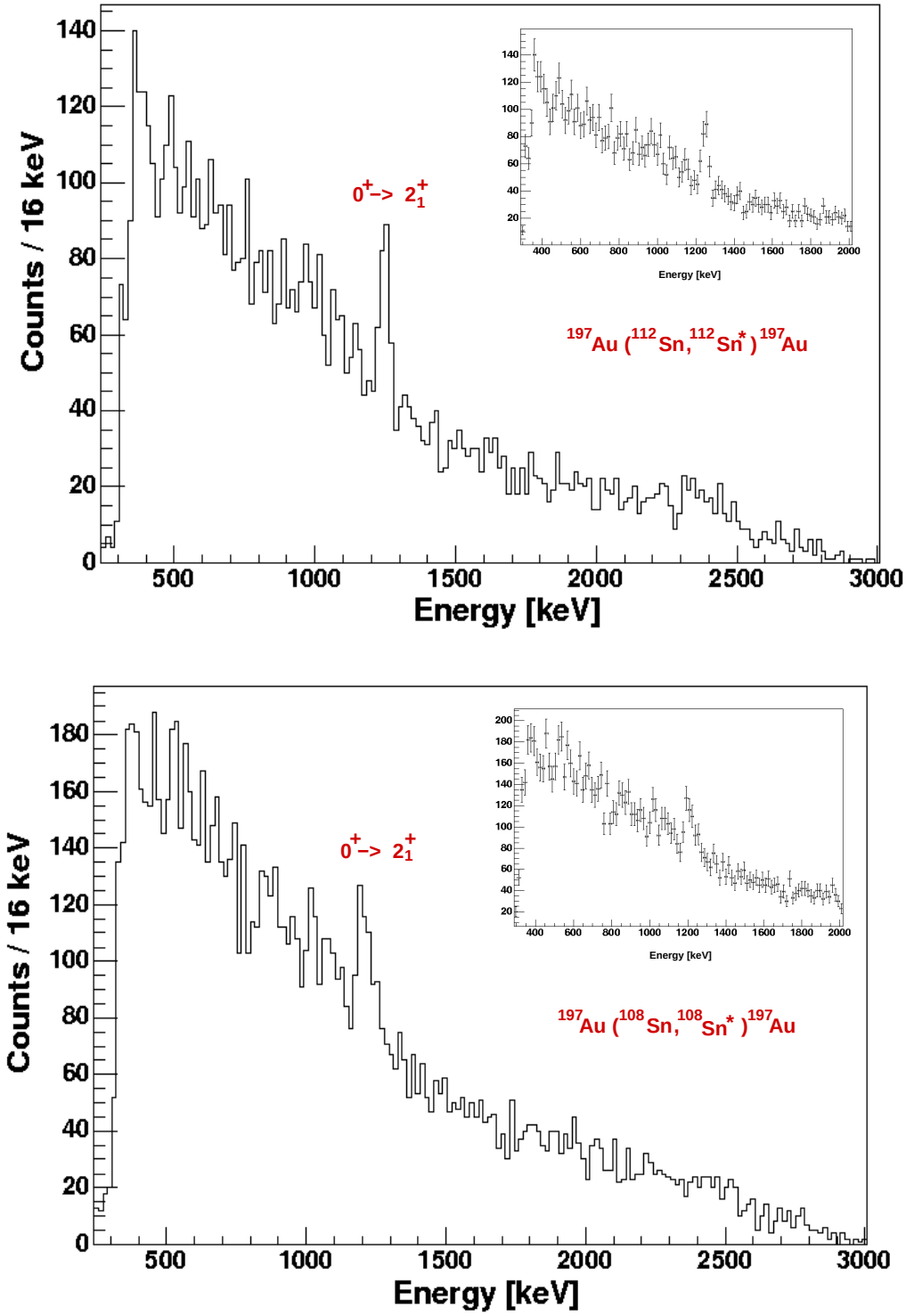

Figure 5.11: De-excitation γ-ray lines following $0^+_{\text{g.s.}} \rightarrow 2^+_1$ Coulomb excitation of the ^{112,108}Sn isotopes, respectively. The insets show the Coulomb excitation peaks including the error bars.

$$N_{E2} = \frac{N_\gamma}{\epsilon_{tot}}.$$

The ratio $\sigma_{E2}^{108}/\sigma_{E2}^{112}$ can be thus determined as

$$\frac{\sigma_{E2}^{108}}{\sigma_{E2}^{112}} = \Big[\frac{N_\gamma}{\epsilon_{tot} N_p N_t}\Big]_{108} \times \Big[\frac{\epsilon_{tot} N_p N_t}{N_\gamma}\Big]_{112}.$$

By taking into consideration that the same target is used in both measurements, one can assume $N_t^{108} \approx N_t^{112}$. In addition, because the 2_1^+ exited states in ^{108,112}Sn lie close in energy, the same γ-ray efficiency can be considered in both cases.

The final expression of the cross section ratio reduces then to the following formula

$$\frac{\sigma_{E2}^{108}}{\sigma_{E2}^{112}} = \frac{N_\gamma^{108}}{N_\gamma^{112}} \times \frac{N_p^{112}}{N_p^{108}}.$$

Next, the photon yield N_γ and the number of incoming particles interacting with the target N_p will be determined for the two cases.

Photon yield determination

To determine the photon yield of a gamma energy peak, one has to evaluate the total area of the peak including the associated background and the background area. The photon yield is then determined by taking the difference of the two areas. To determine these two areas, one has several possibilities. A common method, which was also applied here, is to determine the background under the peak area by averaging it with two background regions at the left- and right-hand side of the peak. If one denotes the left-hand side background region as "A", the peak region as "B", and the right-hand side background region as "C", with corresponding widths w_A, w_B, and w_C, respectively, the photon yield in the peak integral, denoted B_{net}, is calculated as

$$B_{net} = B - \frac{w_B}{w_A + w_C}(A + C).$$

Its statistical error is evaluated by applying the error propagation method as

$$\sigma_{B_{net}} = \sqrt{B + \Big(\frac{w_B}{w_A + w_C}\Big)^2 (A + C)}.$$

The continuous background in the Doppler corrected gamma energy spectra is primarily due to Compton scattering. However, at relativistic beam energies used in the experiment the theoretical shape of this background is complicated. In order to make the background estimation simple yet statistically convincing we take average values for different widths of "A"- and "C"-regions, which is shown in Figure 5.12

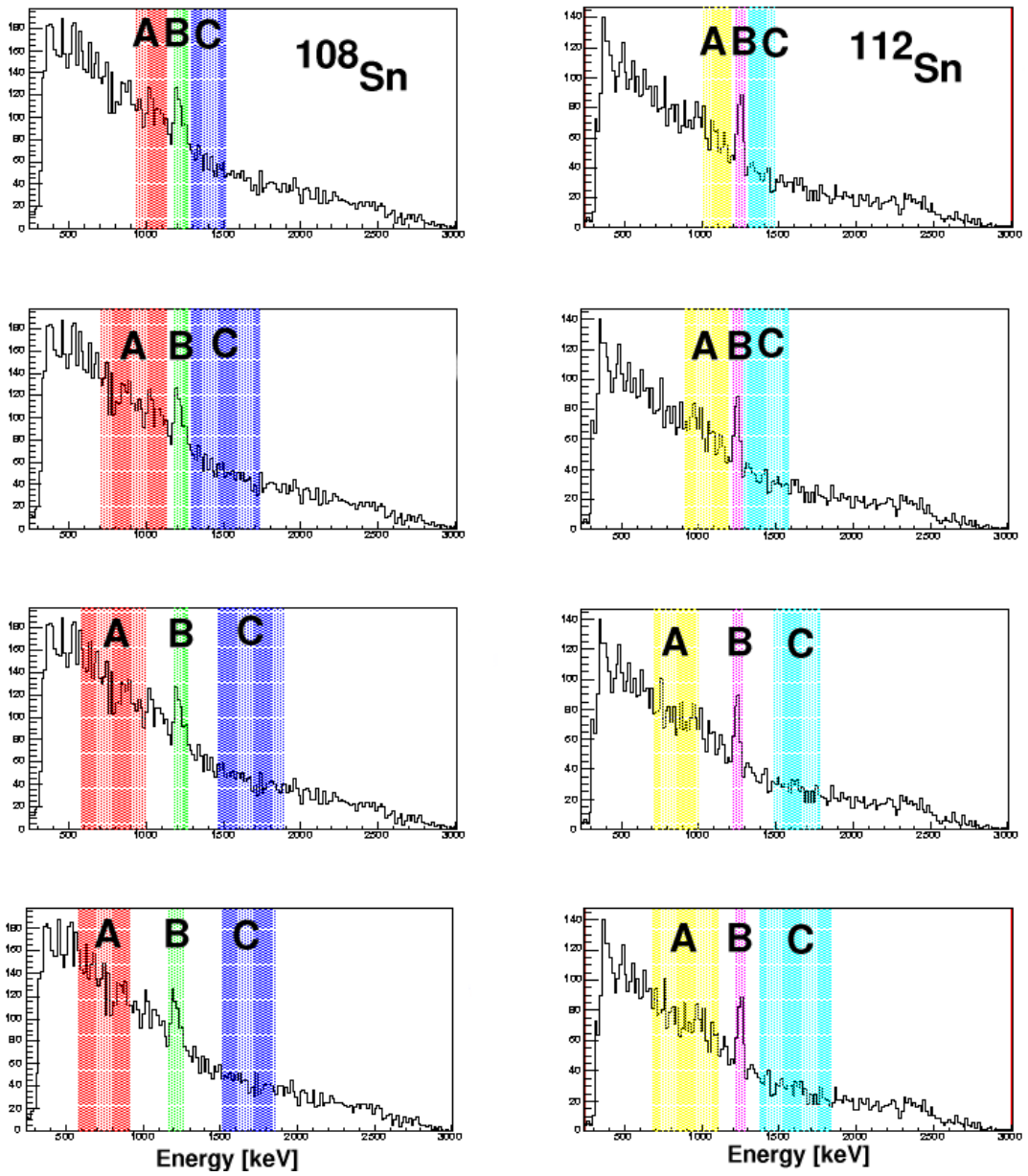

Figure 5.12: Four cases of background selection to determine the Coulomb excitation photon yield in ^{108}Sn (left) and ^{112}Sn (right).

for four such cases. The results on the photon yields in the four cases are tabulated in Table 5.1.

The final numbers of the photon yields N_γ^{108} and N_γ^{112} are determined by the arithmetic average over the four tabulated values:

Table 5.1: Determination of the Coulomb excitation photon yields in ^{108}Sn (top) and ^{112}Sn (bottom) for four cases of background selection

No.	A	B	C	$B_{background}$	B_{net}	$\sigma_{B_{net}}$
1	1268.0	612.0	726.0	438.7	173.3	26.6
2	2554.0	612.0	1167.0	409.3	202.7	25.6
3	3086.0	612.0	988.0	448.1	163.9	25.7
4	4467.0	612.0	1510.0	454.3	157.8	25.4
1	776.0	371.0	421.0	263.3	107.7	20.7
2	1213.0	371.0	628.0	257.7	113.3	20.2
3	1439.0	371.0	511.0	273.0	98.0	20.0
4	2008.0	371.0	827.0	266.5	104.5	19.9

$$\begin{cases} N_{\gamma}^{108} = \frac{B_{net}^{108}(1)+B_{net}^{108}(2)+B_{net}^{108}(3)+B_{net}^{108}(4)}{4} = 174.41 \\ N_{\gamma}^{112} = \frac{B_{net}^{112}(1)+B_{net}^{112}(2)+B_{net}^{112}(3)+B_{net}^{112}(4)}{4} = 105.86 \end{cases}$$

The same operation was applied to their corresponding statistical errors:

$$\begin{cases} \sigma_{N_{\gamma}^{108}} = \frac{\sigma_{B_{net}^{108}}(1)+\sigma_{B_{net}^{108}}(2)+\sigma_{B_{net}^{108}}(3)+\sigma_{B_{net}^{108}}(4)}{4} = 25.85 \\ \sigma_{N_{\gamma}^{112}} = \frac{\sigma_{B_{net}^{112}}(1)+\sigma_{B_{net}^{112}}(2)+\sigma_{B_{net}^{112}}(3)+\sigma_{B_{net}^{112}(4)}}{4} = 20.20 \end{cases}$$

Incoming particle flux determination

During data taking the incoming particle flux was recorded with a scaled down factor using the FRS reduced trigger (see Section 4.8). Hence the total number of incoming particles is equal to the number of scaled down particle-singles events multiplied by the scaled down factor. In the case of ^{112}Sn run the down-scale factor was always 256. For ^{108}Sn run, at the beginning was set to 16 later being changed again to 256 and kept so until the end of the measurement.

In Figure 5.13 are shown scattering angle spectra of both isotopes ^{112}Sn and ^{108}Sn recorded with scaled down particle-singles trigger. The number of counts in these

spectra multiplied by the corresponding scaled down factor, displayed on each spectrum, is equal to the total number of incoming particles interacting with the target.

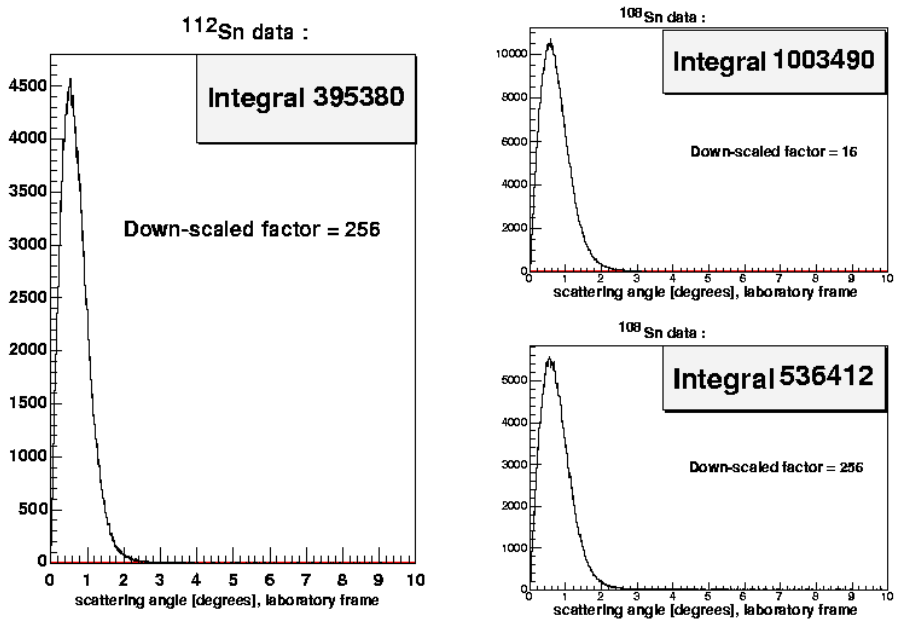

Figure 5.13: Down-scaled scattering angle spectra used to calculate the incoming beam particle flux. See text for details.

The following numbers of incoming beam particles were thus obtained:

$$\begin{cases} N_p^{108} = 1003490 \times 16 + 536412 \times 256 = 153\ 377\ 312. \\ \\ N_p^{112} = 395380 \times 256 = 101\ 217\ 280. \end{cases}$$

with $\sigma_{N_p^{108,112}} = \sqrt{N_p^{108,112}}$, respectively.

By having determined for both ^{108}Sn and ^{112}Sn the photon yield and the number of incoming particle interacting with the target, the cross section[5] ratio $\sigma_{E2}^{108}/\sigma_{E2}^{112}$ can now be determined too. However to determine further the B(E2)-value in ^{108}Sn, there is one more step left. We need to determine the ratio of the proportionality factors between the excitation cross section and the reduced transition probability for ^{112}Sn and ^{108}Sn.

Ratio $f(b_{min}^{112})/f(b_{min}^{108})$ determination

[5]To be more precise here, what you determine experimentally is not exactly cross sections but rather yields since there is set a selection of the scattering angle between 1° and 2°. However one can considered that the measured yield is almost equal to the cross section since the Coulomb excitation probability outside the selected scattering angle range is negligible.

To calculate the ratio of the proportionality factors the code DWEIKO [Ber2003] standard for nuclear scattering at intermediate and high energies (T $\geq$ 50 A·MeV), can be used. For that the minimum impact parameter (b_{min}) and the value of the transition matrix element ($|\langle 0^+|\mathcal{M}(E2)|2_1^+\rangle|$), which for a $0^+_{\text{g.s.}} \rightarrow 2_1^+$ transition is equal to $\sqrt{B(E2\uparrow)}$, need to be known as input parameters for the numerical code. Besides the two mentioned parameters the code also needs the optical potential for the system (projectile, target) in order to perform cross section calculations. In our case since we are interested to calculate only the ratio of Coulomb excitation cross sections for almost two identical (projectile, target) systems, we do not need to know precisely the optical potential which at the end cancels out no matter what are the values set in the code.

Based on the proportionality relationship $\sigma_{E2} = f(b_{min}^{projectile})B(E2)$, the ratio $f(b_{min}^{112})/f(b_{min}^{108})$ can be calculated by setting the same values for the matrix elements ($|\langle 0^+|\mathcal{M}(E2)|2_1^+\rangle|$) of ^{112}Sn and ^{108}Sn. Thus the ratio of the proportionality factors becomes equal to the ratio of the cross sections. With the input parameters fixed, DWEIKO code is run for each of the two isotopes separately, calculating the corresponding cross section. Here we take into account the scattering angle condition applied in the data analysis so that what the code calculates not the absolute cross section but the corresponding yield between 1° and 2°. By using the known B(E2)↑ value in ^{112}Sn and the minimum impact parameters calculated in the straight-line approximation for scattering angle of 1° and 2°, the DWEIKO code returned yields of 233 mb and 264 mb for ^{112}Sn and ^{108}Sn, respectively. Hence, the ratio of the calculated yields leads to a value of 0.88, which is also the value of the $f(b_{min}^{112})/f(b_{min}^{108})$ ratio we needed to determine.

With this last calculation done, the reduced transition probability $B(E2; 0^+ \rightarrow 2_1^+)$ in the ^{108}Sn isotope is determined yielding

$$B(E2; 0^+ \rightarrow 2_1^+) = 0.230\ (57)\ \text{e}^2\text{b}^2,$$

where the error in the brackets is statistical error calculated by standard error propagation [Bev1992].

Chapter 6

Discussion

In the following the measured reduced transition probability in ^{108}Sn is compared to two independent large-scale shell model calculations, and the systematics for the full isotopic chain of tin nuclei between the magic numbers 50 and 82 is discussed within a generalized seniority scheme.

The first set of shell-model calculations was performed by the Oslo group for the all tin isotopes $^{102-130}$Sn, following the prescription outlined in [HJ1995] and using the CD-Bonn potential for the bare nucleon-nucleon interaction [Mac1996]. Three sets of closed shell core were chosen for these calculations – ^{88}Sr, ^{100}Sn and ^{132}Sn. The model space for neutrons comprises in all cases of the $1d_{5/2}$, $0g_{7/2}$, $1d_{3/2}$, $2s_{1/2}$, and $0h_{11/2}$ orbitals, and for ^{88}Sr it includes also protons in the $1p_{1/2}$ and $0g_{9/2}$ orbits. In the discussion here we focus on the results obtained with ^{100}Sn as closed shell core. A harmonic-oscillator basis was chosen for the single particle wave functions, with an oscillator energy $\hbar\omega = 45A^{-1/3}$ - $25A^{-2/3}$ = 8.5 MeV, A = 100 being the mass number. The single-particle energies of the chosen model space orbits are set, relative to the $1d_{5/2}$ orbital ($\epsilon_{1d_{5/2}} = 0.0$ MeV), as follows: $\epsilon_{0g_{7/2}} = 0.08$ MeV, $\epsilon_{1d_{3/2}} = 1.66$ MeV, $\epsilon_{2s_{1/2}} = 1.55$ MeV, $\epsilon_{0h_{11/2}} = 3.55$ MeV. The neutron effective charge was set to 1.0 e. The results of the calculations for the energies of the 2_1^+ excited stated and B(E2;$0^+_{\text{g.s.}} \rightarrow 2_1^+$) values for neutron-deficient tin isotopes are presented in the Table 6.1.

In a second approach, large-scale shell model calculations were performed which allow proton core excitations. The starting point is the realistic interaction (CD-Bonn potential) of the Oslo group, phenomenologically adjusted to the spectroscopy of Sn isotopes and N = 82 isotones [Gni2005]. The differences consist in choosing ^{80}Zr as closed shell core, and consequently a different model space for protons, namely $0g_{9/2}$, $0g_{7/2}$, $1d_{5/2}$, $1d_{3/2}$ and $2s_{1/2}$, and for neutrons the same gds-shell plus the $0h_{11/2}$ orbital. The calculations allow only up to 3p-3h core excitations, and the effective charges are set to 1.55 e and 0.72 e for protons and neutrons, respectively. Since the chosen model space is rather large, the coupled-scheme code NATHAN is used [Cau2002]. In addition, a seniority truncation is applied. Results close to

Table 6.1: Lowest-lying excited state energies and E2 transitions in $^{102-130}$Sn. [1]From Ref. [Ram2001], [2]large-scale shell model calculations performed with ^{100}Sn as closed shell core, [3]this work, [4]from Ref. [Rad2004].

Isotope	$E_{2_1^+}$ [keV]		B(E2↑) [e^2b^2]	
	Exp.[1]	SM[2]	Exp.	SM[2]
^{102}Sn	1472.0 (2)	1646.6		0.043
^{104}Sn	1260.1 (3)	1343.4		0.094
^{106}Sn	1207.7 (5)	1230.9		0.137
^{108}Sn	1206.1 (1)	1243.4	0.230 (57)[3]	0.171
^{110}Sn	1211.9 (2)	1259.2		0.192
^{112}Sn	1256.9 (7)	1236.8	0.240 (14)[1]	0.203
^{114}Sn	1299.9 (7)	1208.3	0.24 (5)[1]	0.209
^{116}Sn	1293.6 (8)	1135.2	0.209 (6)[1]	0.210
^{118}Sn	1229.7 (2)	1068.2	0.209 (8)[1]	0.208
^{120}Sn	1171.3 (2)	1043.8	0.202 (4)[1]	0.201
^{122}Sn	1140.6 (3)	1076.3	0.192 (4)[1]	0.184
^{124}Sn	1131.7 (2)	1118.1	0.166 (4)[1]	0.156
^{126}Sn	1141.2 (4)	1214.1	0.10 (3)[4]	0.118
^{128}Sn	1168.8 (4)	1232.6	0.073 (6)[4]	0.079
^{130}Sn	1121.3 (5)	1190.7	0.023 (5)[4]	0.042

convergence are obtained for seniority equal to 8, for which a B(E2↑) value of 0.176 e^2b^2 is deduced for ^{108}Sn, which is in excellent agreement with the results of the Oslo group (see Table 6.1).

These kind of calculations stress the importance of the core excitations for E2 transitions as origin of the increased effective charge in pure neutron valence space calculations. This conclusion is strengthened by the two additional sets of shell-model calculations, with ^{88}Sr and ^{132}Sn as closed shell cores. For the chain of Sn isotopes with ^{132}Sn and neutron holes, the experimental B(E2;$0^+_{\text{g.s.}} \rightarrow 2^+_1$) values were reproduced with effective charges between 0.7 - 0.8 e for all isotopes from ^{120}Sn to ^{130}Sn [Hol1998]. For ^{108,112}Sn one needs however an effective charge of the order of 1.0 e in order to reproduce the experimental values starting with ^{132}Sn as closed shell core. For ^{88}Sr as closed shell core, the results are similar as for ^{100}Sn as closed shell core, with an effective charge of 1.0 e. This indicates clearly that the effective charges for the lighter tin isotopes show a stronger renormalization effect, unless one allows for core excitations in the model space. It should also be noted that the spectra for $^{102-114}$Sn are in better agreement with the experiment in the case that ^{100}Sn is used as closed shell than if ^{132}Sn is used. Similarly, the excitation spectra for the heavier Sn isotopes $^{114-130}$Sn are better described with a ^{132}Sn core. This may eventually imply the need of different effective charges below and above ^{114}Sn, indicating different character of core excitations at the $N = Z$ and $N \gg Z$ margins of the Sn isotopic chain.

The almost constant energy spacing between the ground state and the first excited 2^+ state, which is so characteristic for the Sn isotopes, is well reproduced by the calculations. Moreover, The B(E2↑) value calculated for the ^{108}Sn case is in good agreement with the measured value. However, for a conclusive interpretation of the results more information is needed.
In Fig 6.1 the systematics of the B(E2↑) values in the Sn isotopes ranging from neutron number $N = 50$ to $N = 82$ is shown. Here the neutrons are filling the subshells between the magic numbers 50 and 82 offering thus an unique opportunity for examining how well the Z = 50 proton-shell closure is holding up as valence neutrons are being added. The data used in the systematics in Fig 6.1 are from the calculations using ^{100}Sn as closed shell core an effective charge 1.0 e. The theoretical results yield a parabola-like trend. For comparison the experimental data measured recently for unstable heavy ^{126,128,130}Sn Sn isotopes [Rad2004], for unstable light ^{108}Sn (this work) and the adopted values for the stables isotopes $^{112-124}$Sn [Ram2001] are shown.

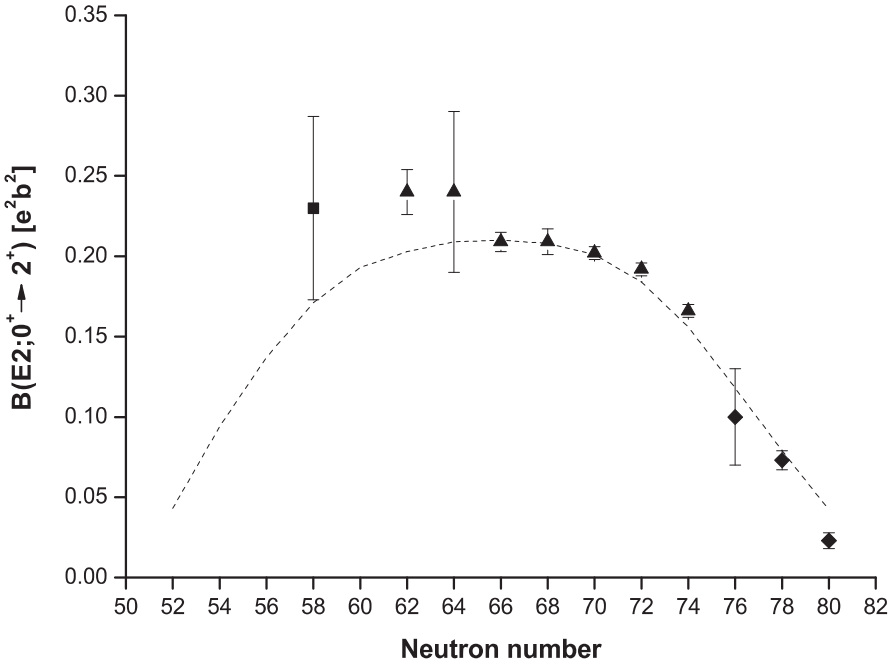

Figure 6.1: Comparison of measured $B(E2; 0^+_{\text{g.s.}} \rightarrow 2^+_1)$ values with theoretical predictions (see text for details).

The parabola-like trend of the B(E2) systematics resembles the typical behavior of a one-body even tensor operator across a shell in the seniority scheme [Cas2000], which for a seniority changing transition $(\Delta\upsilon) = 2$) at first increases, then flattens out, peaking at the midshell, and falling off thereafter. In a non-unique j shell with many interacting orbitals this can be generalized to $B(E2; 0^+_{\text{g.s.}} \rightarrow 2^+_1) \approx$ f(1-f) with f = (N - 50)/32 being the filling factor of the shell, where N denotes the neutron number. If we use ^{132}Sn as closed shell core, as mentioned before, two sets of effective charges may be needed, $e_{\text{eff}} \approx$ 0.7 - 0.8 e for ^{114}Sn to ^{130}Sn and $e_{\text{eff}} \approx$

1.0 e for ^{108}Sn and ^{112}Sn, indicating in this case that a two-parabola fit assuming a subshell closure around N = 64 might be more appropriate. A closer inspection of the experimental data seems to suggest this as well. This can be described microscopically in a paring approach [Kis1960].

The overall agreement between the experimental and theoretical B(E2) values across the N = 50 - 82 neutron shell underlines the success of a generalized seniority scheme in describing the properties of the even Sn nuclei. The tendency of larger B(E2) values in the lighter isotopes can be traced back to two effects, **(i)** enhanced core excitation towards N=Z as supported by the shell-model calculation [Gni2005] and/or **(ii)** the blocking of 1p1h neutron excitation from the g, d, s orbits to the odd-parity $h_{11/2}$ orbit for N $\gtrsim$ 64, which can not contribute to the E2 transition. The trend is exhibited more clearly in the Ni isotopes one major shell lower [Sor2002], which show a distinct minimum in the B(E2) at N = 40.

In conclusion, we have measured for the first time the $B(E2; 0^+_{\text{g.s.}} \rightarrow 2^+_1)$ value in the unstable ^{108}Sn isotope with intermediate-energy Coulomb excitation. This is the highest-Z nucleus studied with this method.

The comparison with two different but complementary large-scale shell model calculations shows agreement and proves that a combination of core excitation and valence particles is substantial for a correct description of the lowest 2^+ collective state.

The successful B(E2) measurement in ^{108}Sn opens at GSI the research line via the experimental technique of intermediate-energy Coulomb excitation towards perhaps the most interesting nucleus ever experimentally synthesized, the proton drip line heaviest doubly-magic nucleus ^{100}Sn.

Appendix A

Coulomb excitation cross section – Excitation amplitude

Excitation amplitude determination

In the following it is assumed that the target nucleus is at rest and the projectile moves on a straight-line trajectory of impact parameter ρ, which is also the distance of closest approach between the centers of mass of the two nuclei at collision time $t = 0$. It is considered that ρ is larger than the sum of the two nuclear radii, R, such that the charge distributions of the two nuclei do not overlap. Furthermore, a coordinate system with the origin in the center of mass of the target and with the z-axis along the constant velocity $\mathbf{v}_p$ of the projectile in used (see Figure A.1). In this coordinate system the electromagnetic field from the projectile nucleus is given

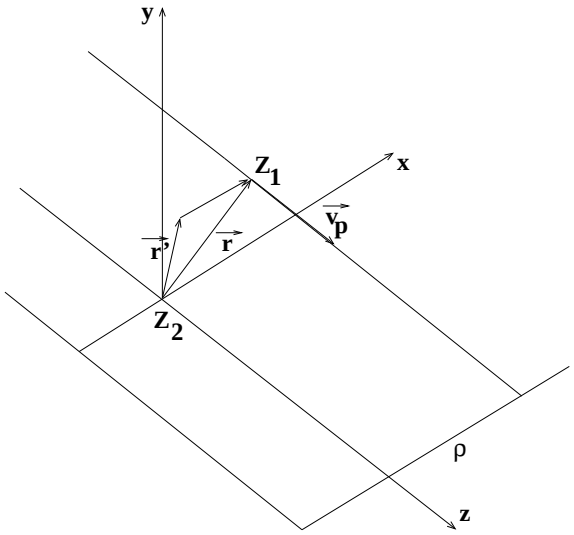

Figure A.1: The straight-line trajectory of the projectile Z_1 with an impact parameter ρ and a velocity v_p. The coordinate system with the origin in the target nucleus Z_2 is indicated.

by the Lienard-Wiechert expression [Pan1955]

$$\phi(\mathbf{r\prime},t)=\frac{Z_1e\gamma}{[(\rho-x\prime)^2+y\prime^2+\gamma^2(z\prime-v_pt)^2]^{\frac{1}{2}}},$$

$$\mathbf{A}(\mathbf{r\prime},t)=\frac{v_p}{c}\phi(\mathbf{r\prime},t).$$

It has been chosen the x-axis in the plane of the trajectory such that the x-component of the center of mass of the target is equal to ρ.
The Fourier components of the field are given by

$$\phi(\mathbf{r\prime},\omega)=\int_{-\infty}^{\infty}\phi(\mathbf{r\prime},t)e^{i\omega t}dt=\frac{2Z_1e}{v_p}e^{i(\omega/v_p)z\prime}K_0\Big(\frac{\omega}{v_p}q\Big),$$

where K_0 is a modified Bessel function and q is given by

$$q^2=\frac{1}{\gamma^2}[(\rho-x\prime)^2+y\prime^2].$$

The multipole component expansion of the above Fourier components of the field has the following expression:

$$\phi(\mathbf{r\prime},\omega)=\sum_{\lambda\mu}W_{\lambda\mu}(r\prime,\omega)Y^*_{\lambda\mu}(\hat{\mathbf{r}}\prime),$$

with

$$W_{\lambda\mu}(r\prime,\omega)=\int d\Omega\prime\phi(\mathbf{r\prime},\omega)Y_{\lambda\mu}(\hat{\mathbf{r}}\prime)$$

$$=\frac{2Z_1e}{v_p}\int_0^{\pi}e^{i(\omega/v_p)\mathbf{r}\prime\cos\vartheta\prime}Y_{\lambda\mu}(\vartheta\prime,0)d\cos\vartheta\prime\int_0^{2\pi}e^{i\mu\varphi\prime}K_0\Big(\frac{\omega}{v_p}q\Big)d\varphi\prime.$$

Hence one can calculate the excitation amplitude of the state $|f\rangle$ in first order time-dependent perturbation theory as a function of the above coefficients in the multipole expansion,

$$a_{i\to f}=\frac{1}{i\hbar}\sum_{\lambda\mu}\langle I_fM_f|\int d^3r\prime\Big(\rho_2(\mathbf{r\prime})-\frac{\mathbf{v}_p\cdot\mathbf{j}_2(\mathbf{r\prime})}{c^2}\Big)W_{\lambda\mu}(r\prime,\omega_{fi})Y_{\lambda\mu}(\hat{\mathbf{r}}\prime)|I_iM_i\rangle,$$

where $\rho_2(\mathbf{r})$, $\mathbf{j}_2(\mathbf{r})$ are the charge respective the current density in the target nucleus.

Taking into consideration the usual expression for the electric multipole matrix elements

$$M_2(E\lambda\mu)=\frac{(2\lambda+1)!!}{k^{\lambda+1}c(\lambda+1)}\int\mathbf{j}_2(\mathbf{r\prime})\cdot\bigtriangledown\times\mathbf{L}(j_\lambda(kr\prime)Y_{\lambda\mu}(\hat{\mathbf{r}}\prime))d^3r\prime,$$

the excitation amplitude with respect to electric excitation may be written in the form

$$a_{i\to f} = -i\frac{Z_1 e^2}{\hbar v_p \gamma}\sum_{\lambda\mu} G_{\lambda\mu}\Big(\frac{c}{v_p}\Big)(-1)^\mu K_\mu(\xi(\rho))\sqrt{2\lambda+1}k^\lambda\langle I_f M_f|M_2(\lambda-\mu)|I_i M_i\rangle/e,$$

where for $\mu \geqslant 0$

$$G_{\lambda\mu}\Big(\frac{c}{v_p}\Big) = i^{\lambda+\mu}\frac{\sqrt{16\pi}}{\lambda(2\lambda+1)!!}\Big(\frac{(\lambda-\mu)!}{(\lambda+\mu)!}\Big)^{\frac{1}{2}}\Big(\Big(\frac{c}{v_p}-1\Big)^2\Big)^{-\frac{1}{2}}$$
$$\times\Big(\frac{(\lambda+1)(\lambda+\mu)}{2\lambda+1}P^\mu_{\lambda-1}\Big(\frac{c}{v_p}\Big) - \frac{\lambda(\lambda-\mu+1)}{2\lambda+1}P^\mu_{\lambda+1}\Big(\frac{c}{v_p}\Big)\Big).$$

In this expression $P^\mu_\lambda(x)$ is the associated Legendre function.

The quantity $\xi(\rho)$ which enters in the above expression of the excitation amplitude is the adiabaticity parameter for an impact parameter ρ introduced earlier.
It has been found [Win1979] that because of the fact that the actual distance of closest approach is increased due to the Coulomb repulsion, the impact parameter ρ should be substituted by $\rho + \frac{1}{2}\pi a$, a being half the distance of closest approach in a head-on collision ($\rho = 0$). Since the relativistic expression for the increase in relative distance at the collision time $t = 0$ is given by a/γ, one obtains an improved expression for the Coulomb excitation amplitude by using for $\xi(\rho)$ in the above expression the definition

$$\xi(\rho) = \frac{\omega}{v_p\gamma}\Big(\rho + \frac{\pi}{2}\frac{Z_1 Z_2 e^2}{m_0 v_p^2\gamma}\Big),$$

where m_0 is the reduced mass of the two nuclei.

Appendix B

Background measurement in Λ-hypernuclei production at GSI

In this appendix it is described a feasibility test experiment performed at GSI in connection with the High-Resolution Hypernuclear γ-spectroscopy investigations, which the author of this doctoral thesis has been also contributed to during the time of her doctoral studies.

Introductory remarks

A hypernucleus is a characteristic bound system of an ordinary nucleus and a few hyperons; a Λ-hypernucleus consists of nucleons and only one Λ hyperon.
Λ-hypernuclear spectroscopy can provide us with information concerning the behavior of a baryon deep inside a nucleus. In an ordinary nucleus, if a deep-hole state is created, it immediately decays by emitting nucleons but its width becomes too broad to provide clear spectroscopic information. On the other hand, a Λ hyperon (characterized by a strangeness quantum number) implanted in a nucleus can freely move within the nucleus since it is free from the Pauli blocking by nucleons, and narrow hypernuclear states can be formed.
A Λ hypernucleus is thus a good tool to investigate the two-body $\Lambda - N$ interaction. For an unified understanding of the baryon-baryon interaction in terms of meson exchange forces and, ultimately in terms of the quark picture, it is very important to understand the $\Lambda - N$ interaction as well as the $N - N$ interaction.

In 1980, the (π^+, K^+) reaction was proposed to be an effective tool for spectroscopy studies [Thi1980, Dov1980]. The usefulness of the reaction was demonstrated in the experiments at KEK and BNL. At KEK, high-resolution γ-spectroscopy with the Ge-detector array HYPERBALL has been successfully performed for ${}^{7}_{\Lambda}$Li in a ^{7}Li$(\pi^+, K^+){}^{7}_{\Lambda}$Li reaction at 1.05 GeV/c [Tam2000].
At GSI, Λ-hypernuclei can be produced via the (π^+, K^+) reaction. Thus, a similar experiment for medium heavy nuclei with $A \sim 90$ has been proposed [Ger1999].
Gamma-ray spectroscopy with Ge detectors is difficult because of high energy particle background causing large dead time to the Ge detectors due to the saturation

of the preamplifiers, as observed in one of our feasibility tests (Figure B.1).

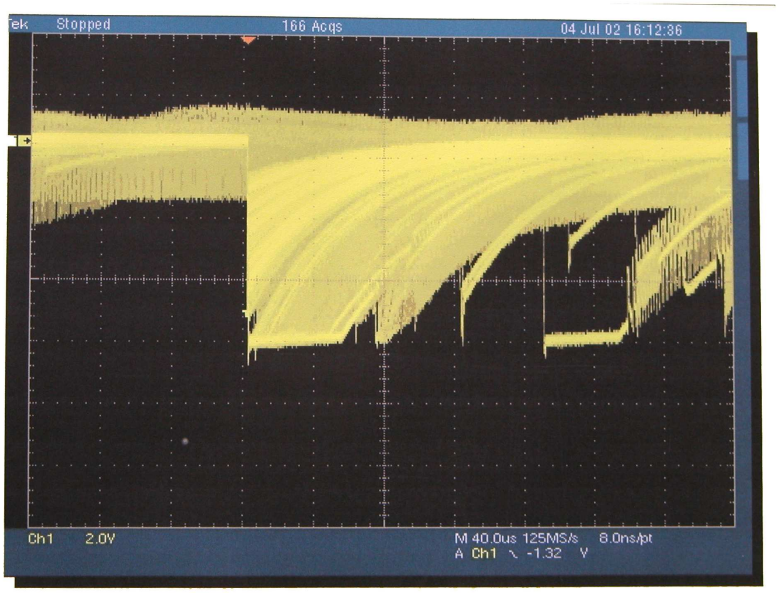

Figure B.1: Saturated Ge preamplifier signal by π^+-induced particle background.

The problem was solved by HYPERBALL collaboration by using transistor-reset preamplifiers. However, the nature of the background has not been well understood.

The background measurement

In the following is described a background measurement carried out at GSI, as part of those initial efforts of understanding the nature of the hadronic background resulted in the production of the Λ-hypernuclei via $(\pi^+), K^+$ reaction, and moreover of quantitatively characterizing it.

At the pion beam facility at GSI, we produced a secondary π^+ beam from a primary ^{12}C beams at 2 GeV/u on a Be production target. Secondary π^+ beams at 0.93 GeV/c and 1.12 GeV/c were transferred to Cave C. Two different experimental targets, ^{89}Y and ^{12}C, were used at each of the aforementioned momenta. Since there is no separator in the beam line, other secondary particles in particular $^{1-3}$H, ^{3}He were also impinging on the experimental targets. In Figure B.2 the experimental set-up is illustrated schematically.

The time-of-flight was measured for the beam particles by using two plastic scintillators with 5 mm thickness separated by 2.2 m. Figure B.3 shows the separation among the beam particles at 1.12 GeV/c.

The beam profile was measured by a position-sensitive Si strip detector with 0.5 mm strip width to be $\sigma_x = 7.3$ mm and $\sigma_y = 8.9$ mm. Particles produced in the experimental targets, ^{89}Y and ^{12}C, were measured by a BaF_2 detector at 90° surrounded by six NaI detectors. A plastic scintillator with 9 mm thickness was placed in front of the BaF_2 detector. The distance of the BaF_2 detector to the target

center was 15 cm. Particle identification was performed by pulse shape analyses combined with information from the plastic scintillator and NaI detectors, as shown in Figure B.4.

Spectra of π^+, protons, high energy γ-rays from π^0 decay, high energy neutrons, electrons, heavy ions, and low energy neutral particles (mainly low energy γ-rays and neutrons (E $<$ 30 MeV)) originating from the target were obtained for each kind of projectile particle by using cuts in time-of-flight spectrum and beam position. Table B.1 shows results for the yield of background particles produced by the interaction of π^+ and proton beams with the ^{89}Y target with more than 10 MeV energy loss in BaF_2 normalized to the beam intensity at the target for 1.12 GeV/c momentum.

We have observed significant particle background with the π^+ beam hitting the ^{89}Y target and we preliminary conclude that the rate of produced particle background can be explained by nucleon resonances. For proton beams, as shown in the table, we have observed less background, and we have observed no background at all with the other beam particles composing the primary beam.

The results of the measurement show that the proposed hypernuclear γ-spectroscopy experiment at GSI with two VEGA Ge detectors at 3 cm from the target could be performed with a necessary π^+ beam intensity of 5×10^5 per second.

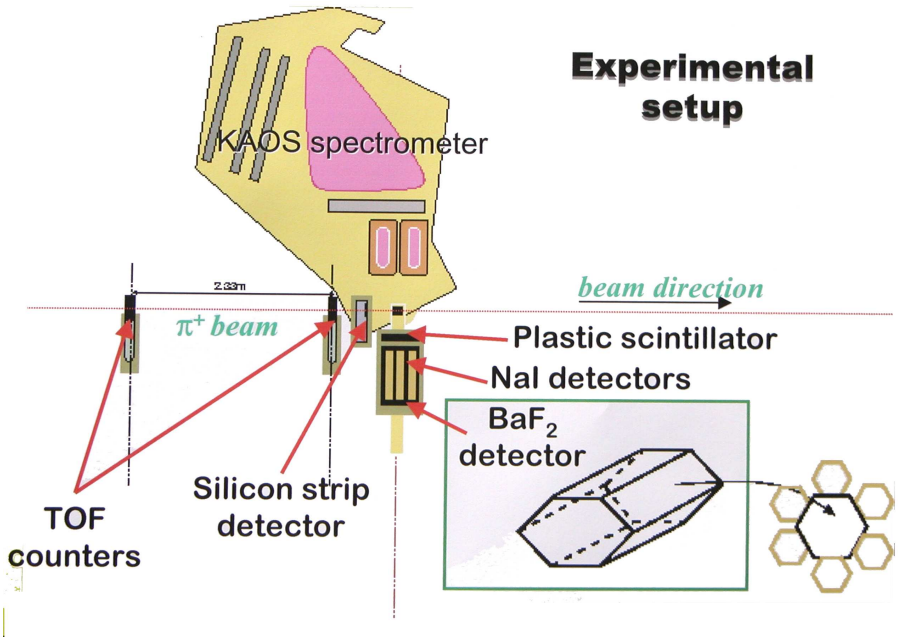

Figure B.2: Schematic layout of the experimental set-up.

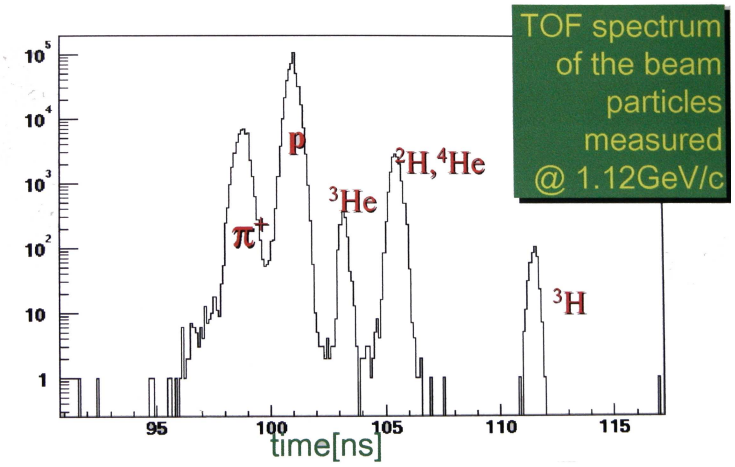

Figure B.3: Time-of-flight separation for beam particles measured at 1.12 GeV/c momentum.

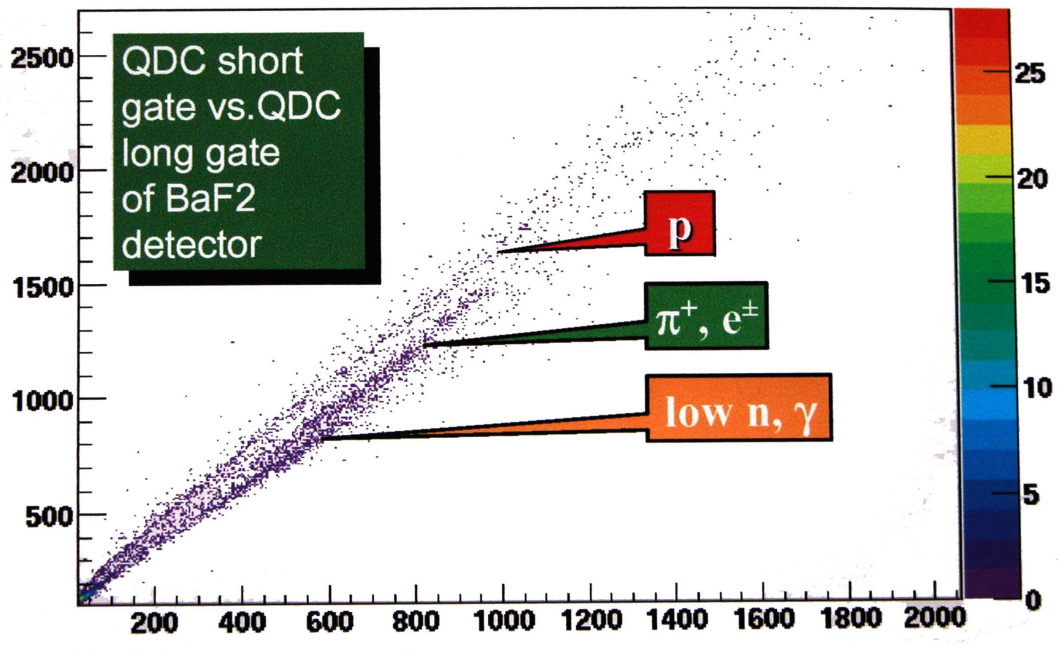

Figure B.4: Background particle identification by using BaF_2 pulse shape analysis.

Table B.1: Background particle measurement for energy deposit > 10 MeV in BaF_2 as a result of interaction between π^+ and proton beams at 1.12 GeV/c on the ^{89}Y target. The particle yields are normalized to the total intensity of the beams hitting the target

Particles	π^+ beam	Proton beam
π^+	$4(3)\times10^{-4}$	$< 2\times10^{-6}$
Proton	$10(4)\times10^{-4}$	$8(1)\times10^{-4}$
High energy γ-ray	$4(3)\times10^{-4}$	$5(3)\times10^{-5}$
Electron	$1(1)\times10^{-4}$	$3(2)\times10^{-5}$
Low energy neutral particles (E < 30 MeV)	$7(3)\times10^{-4}$	$16(5)\times10^{-5}$

List of Figures

List of Tables

Bibliography

[Ald1966] Kurt Alder and Aage Winther. *Coulomb Excitation*. Academic Press, New York (1966).

[Ald1975] Kurt Alder and Aage Winther. *Electromagnetic excitation theory of Coulomb excitation with heavy ions*. North-Holland Publishing Company, Amsterdam (1975).

[Ale1989] A.N.F. Aleixo and C.A. Bertulani. *Coulomb excitation in intermediate-energy collisions*. Nucl. Phys. **A505**, 448–470 (1989).

[Anh1986] R. Anholt et al. *Atomic collisions with relativistic heavy ions. VI. Radiative processes*. Phys. Rev. **A33**, 2270–2280 (1986).

[Aum1995] T. Aumann et al. (1995), GSI preprint GSI-95-19.

[Ban2004] A. Banu and F. Becker (2004), private communications.

[Bed2003] P. Bednarczyk (2003), private communications.

[Ben1989] C.J. Benesh, B.C. Cook, and J.P. Vary. *Single nucleon removal in relativistic nuclear collisions*. Phys. Rev. **C40**, 1198–1206 (1989).

[Ben1998] J. Benlliure, A. R. Junghans, and K.-H. Schmidt. *Production of medium-weight isotopes by fragmentation in 750 $A{\cdot}MeV$ ^{238}U on ^{208}Pb collisions*. Eur. Phys. J. **A2**, 193–198 (1998).

[Ben2002] J. Benlliure, A. R. Junghans, and K.-H. Schmidt. *Shell effects and pairing correlations in fission investigated with radioactive beams*. Eur. Phys. J. **A13**, 93–98 (2002).

[Ber1988] C.A. Bertulani and G. Baur. *Electromagnetic processes in relativistic heavy ion collisions*. Phys. Rep. **163**, 299–408 (1988).

[Ber1994] M. Bernas et al. *Projectile fission at relativistic velocities: a novel and powerful source of neutron-rich isotopes well suited for in-flight isotopic separation*. Phys. Lett. **B331**, 19–24 (1994).

[Ber1997] M. Bernas et al. *Discovery and cross-section measurement of 58 new fission products in projectile-fission of 750 $A{\cdot}MeV$ ^{238}U*. Phys. Lett. **B415**, 111–116 (1997).

[Ber2003] C.A. Bertulani, C.M. Campbell, and T. Glasmacher. *A computer program for nuclear scattering at intermediate and high energies*. Computer Physics Communications **152**, 317–340 (2003).

[Bev1992] P.R. Bevington and D.K. Robinson. *Data Reduction and Error Analysis for the Physical Sciences*. WCB/McGraw-Hill (1992).

[Bie1965] L.C. Biedenharn and P.J. Brussaard. *Coulomb Excitation*. Clarendon Press, Oxford (1965).

[Bla2004] A. Blazhev et al. *Observation of a core-excited $E4$ isomer in ^{98}Cd*. Phys. Rev. **C69**, 064304(1–8) (2004).

[Boh1969] A. Bohr and B.R. Mottelson. *Nuclear Structure (Vol. I)*. W.A. Benjamin, Inc. (1969).

[Boh1975] A. Bohr and B.R. Mottelson. *Nuclear Structure (Vol. II)*. W.A. Benjamin, Inc. (1975).

[Cas2000] Richard F. Casten. *Nuclear Structure from a Simple Perspective*. Oxford University Press Inc., New York (2000).

[Cau2002] E. Caurier and G. Martínez-Pinedo. *Frontier of Shell Model Calculations*. Nucl. Phys. **A704**, 60c–68c (2002).

[Don1998] C. Donzaud et al. *Low-energy fission investigated in reactions of 750 $A{\cdot}MeV$ ^{238}U-ions on ^{208}Pb: Isotopic distributions*. Eur. Phys. J. **A1**, 407–426 (1998).

[Doo2003] P. Doornenbal. *Doppler-Shift korrigierte -Spektroskopie nach einem Coulomb-Anregungsexperiment*. Diploma thesis, Universität Frankfurt am Main (2003).

[Dov1980] C.B. Dover, L. Ludeking, and G.E. Walker (1980), Phys. Rec. C 22, pag. 2073.

[Ebe1996] J. Eberth et al. *Encapsulated Ge detectors:development and first tests*. Nucl. Instr. and Meth. **A369**, 135–140 (1996).

[Eng1995] Ch. Engelmann et al. *Production and identificationof heavy Ni isotopes: evidence for the doubly magic nucleus ^{78}Ni*. Z. Phys. **A352**, 351–352 (1995).

[Enq1999] T. Enqvist et al. *Systematic experimental survey on projectile fragmentation and fission induced in collisions of ^{238}U at 1 $A{\cdot}GeV$ with lead*. Nucl. Phys. **A658**, 47–66 (1999).

[Ess1996] H. G. Essel, J. Hoffmann, N. Kurz, R. S. Mayer, W. Ott, and D. Schall (1996), IEEE Transactions on Nuclear Science, Vol.43, No.1, p.132.

[FS1959] Jr. F.S. Stephens, R.M. Diamond, and I. Perlman. *Multiple Coulomb Excitation in Th^{232} and U^{238}*. Phys. Rev. Lett. **3**, 435–438 (1959).

[Gad1997] A. Gadea et al. *Magnetic rotation in the ^{105}Sn*. Phys. Rev. **C55**, R1–R4 (1997).

[Gai1991] J.-J. Gaimard and K.-H. Schmidt. *A reexamination of the abrasion-ablation model for the description of the nuclear fragmentation reaction*. Nucl. Phys. **A531**, 709–745 (1991).

[Gei1992] H. Geissel et al. *The GSI projectile fragment separator (FRS): a versatile magnetic system for relativistic heavy ions*. Nucl. Instr. and Meth. **B70**, 286–297 (1992).

[Gei1995] H. Geissel and G. Münzenberg. *Secondary exotic nuclear beams*. Ann. Rev. Nucl. Part. Sci. **45**, 163–203 (1995).

[Ger1999] J. Gerl et al. (1999), LOI of S234 experiment, GSI.

[Gla1998] T. Glasmacher. *Coulomb excitation at intermediate energies*. Annu. Rev. Nucl. Part. Sci. **48**, 1–31 (1998).

[Gni2005] A. Gniady (2005), private communications.

[Gol1974] A.S. Goldhaber. *Statistical models of fragmentation processes*. Phys. Lett. **B53**, 306–308 (1974).

[Gol1978] A. S. Goldhaber and H. H. Heckmann. *High energy interactions of nuclei*. Ann. Rev. Nucl. Part. Sci. **28**, 161–205 (1978).

[Gor1997] M. Gorska et al. *$^{98}_{48}Cd_{50}$: The two-proton-hole spectrum in $^{100}_{50}Sn_{50}$*. Phys. Rev. Lett. **79**, 2415–2418 (1997).

[Gor1998] M. Gorska et al. *Structure of high spin states in ^{104}Sn: $E2$ and $E3$ polarization of the ^{100}Sn core*. Phys. Rev. **C58**, 108–115 (1998).

[Gra2003] H. Grawe. *New vista of shell structure in neutron-rich exotic nuclei*. Acta Phys. Pol. B. **34**, 2267–2275 (2003).

[Han1990] E. Hanelt, J. Weckenmann, K.-H. Schmidt, H.-G. Clerc, and H. Folger. *The Universal Energy Degrader System for the Fragment Separator*. Scientific report, Geselleschaft für Schwerionenforschung (1990).

[HJ1995] M. Hjorth-Jensen et al. *Realistic effective interactions for nuclear systems*. Phys. Rep. **261**, 125–270 (1995).

[Hof2002] J. Hoffmann and N. Kurz (2002), GSI Scientific Report, p.224.

[Hol1998] A. Holt, T. Engeland, M. Hjorth-Jensen, and E. Osnes. *Effective interactions and shell model studies of heavy tin isotopes*. Nucl. Phys. **A634**, 41–56 (1998).

[Ign1979] A.V. Ignatyuk, K.K. Istekov, and G.N. Smirenkin. *The role of collective effects in the systematics of nuclear level densities.* Sov. J. Nucl. Phys. **29**, 450–454 (1979).

[Kis1960] L.S. Kisslinger and R.A. Soerensen (1960), Mat. Fys. Medd. Dan. Vid. Selsk.

[Laz1992] I. Lazarus, P. Coleman-Smith, N. Karkour, G. M. McPherson, A. Richard, and C. Ring (1992), IEEE Transactions on Nuclear Science, Vol.39, p.1352.

[Lew1994] M. Lewitowicz et al. *Identification of the doubly-magic nucleus ^{100}Sn in the reaction $^{112}Sn+^{nat}Ni$ at 63 MeV/nucleon.* Phys. Lett. **B332**, 20–24 (1994).

[Lip1998] M. Lipoglavšek et al. *E2 polarization charge in ^{102}Sn.* Phys. Lett. **B440**, 246–250 (1998).

[Loz2003] R. Lozeva et al. *Investigation of scintillation detectors for relativistic heavy ion calorimetry.* Nucl. Instr. and Meth. **B204**, 678–681 (2003).

[Loz2005] R. Lozeva. *A new developed calorimeter telescope for identification of relativistic heavy-ion reaction channels.* PhD thesis, Faculty of Physics, University of Sofia (2005).

[Mac1996] R. Machleidt, F. Sammarruca, and Y. Song. *Nonlocal nature of the nuclear force and its impact on nuclear structure.* Phys. Rev. **C53**, 1483–1487 (1996).

[Maj1994] A. Maj et al. *Angular distribution of photons from the delay of the GDR in hot and rotating light Yb nuclei from exclusive experiments.* Nucl. Phys. **A571**, 185–220 (1994).

[Mat1974] E. der Mateosion and A.W. Sunyar. *Tables of angular-distribution coefficients for gamma rays of mixed multipolarities emitted by aligned nuclei.* Atomic Data and Nucl. Data Tables **13**, 407–462 (1974).

[McC1953] C.I. McClelland and C. Goodman. *Excitation of Heavy Nuclei by Electric Field of Low-Energy Protons.* Phys. Rev. **91**, 760–761 (1953).

[Mün1992] G. Münzenberg. *The separation techniques for secondary beams.* Nucl. Instr. and Meth. **B70**, 265–275 (1992).

[Naz1995] W. Nazarewicz, J. Dobaczewski, and T.R. Werner. *Physics of exotic nuclear states.* Phys. Scrip. **T56**, 9–14 (1995).

[Ots2001] T. Otsuka, R. Fujimoto, Y. Utsuno, B.A. Brown, M. Honma, and T. Mizusaki. *Magic numbers in exotic nuclei and spin-isospin properties of the NN interaction.* Phys. Rev. Lett. **87**, 082502(1–4) (2001).

[Pan1955] W.K.H. Panofsky and M. Phillips. *Classical electricity and magnetism.* Addison-Wesley, Reading, Mass. (1955).

[Pel1982] D. Pelte and D. Schwalm. *In-beam gamma-ray spectroscopy with heavy ions.* R. Bock, Gesellschaft für Schwerionenforshung, Darmstadt, F. R. Germany (1982).

[Puc1995] V. Pucknell (1995), The MIDAS Multi Instance Data Acquisition System, http://npg.dl.ac.uk/MIDAS.

[Rad2004] D.C. Radford et al. *Nuclear structure studies with heavy neutron-rich RIBS at the HRIBS.* Nucl. Phys. **A746**, 83c–89c (2004).

[Ram2001] S. Raman, Jr. C. W. Nestor, and P. Tikkanen. *Transition Probability from the Ground to the First-Excited 2^+ State of Even-Even Nuclides.* Atomic Data and Nucl. Data Tables **78**, 1–129 (2001).

[Sai2003] T. Saitoh (2003), private communications.

[Sch1993] K. H. Schmidt et al. *Distribution of Ir and Pt isotopes produced as fragments of 1 $A{\cdot}GeV$ ^{197}Au projectiles: a thermometer for peripheral nuclear collisions.* Phys. Lett. **B300**, 313–316 (1993).

[Sch1994] R. Schneider. *Production and identification of ^{100}Sn.* Z. Phys. **A348**, 241–242 (1994).

[Sch1998a] C. Scheidenberger and H. Geissel. *Penetration of relativistic heavy ions through matter.* Nucl. Instr. and Meth. **B135**, 25–34 (1998).

[Sch1998b] W. Schwab et al. *Fission of highly excited fragments from collisions of 750 $A{\cdot}MeV$ ^{238}U-ions on ^{208}Pb.* Eur. Phys. J. **A2**, 179–191 (1998).

[Sha1963] Amos de Shalit and Igal Talmi. *Nuclear Shell Theory.* ACADEMIC PRESS, INC., New York (1963).

[Sim1997] J. Simpson. *The Euroball Spectrometer.* Z. Phys. **A358**, 139–143 (1997).

[Sim2002] J. Simpson, R. Griffiths, and K. Fayz (2002), RISING Designs Status for Steering Committee Meeting on 7/10/2002, Daresbury Laboratory.

[Sor2002] O. Sorlin et al. *$^{68}_{28}Ni_{40}$: Magicity versus Superfluidity.* Phys. Rev. Lett. **88**, (092501)1–5 (2002).

[Ste1991] H. Stelzer. *Multiwire chambers with a two-stage amplification.* Nucl. Instr. and Meth. **A310**, 103–106 (1991).

[Sto2000] A. Stolz and R. Schneider (2000), Technical Manual, Ionisation Chamber MUSIC80.

[Süm1990] K. Sümmerer, W. Brüchle, D. J. Morrissey, M. Schädel, B. Szweryn, and Y. Weifan. *Target fragmentation of Au and Th by 2.6 GeV protons*. Phys. Rev. **C42**, 2546–2561 (1990).

[Süm2000] K. Sümmerer and B. Blank. *Modified empirical parametrization of fragmentation cross sections*. Phys. Rev. **C61**, (034607)1–10 (2000).

[Tam2000] H. Tamura et al. (2000), Phys. Rev. Lett. 84, pag. 5963.

[Tan1999] I. Tanihata. *Reactions with Radioactive Ion Beams*. Nucl. Phys. **A654**, 235c–251c (1999).

[Tar2004] O. Tarasov. *Analysis of momentum distributions of projectile fragmentation products*. Nucl. Phys. **A734**, 536–540 (2004).

[Thi1980] H.A. Thiessen (1980), AGS proposal, 758.

[TM1952] K.A. Ter-Martirosyan (1952), J. Exptl. Theoret. Phys. (U.S.S.R.) 22, 284.

[Vos1989] B. Voss. *Entwicklung, Untersuchung und Anwendung eines positionsauflösenden Szintillationszählers zur Ortsbestimmung relativistischer schwerer Ionen*. Diploma thesis, Institut für Kernphysik der Technischen Hochschule Darmstadt (1989).

[Wil1996] M. Wilhelm and others. *The response of the Euroball Cluster detector to γ-radiation up to 10 MeV*. Nucl. Instr. and Meth. **A381**, 462–465 (1996).

[Win1979] A. Winther and K. Alder. *Relativistic Coulom excitation*. Nucl. Phys. **A319**, 518–532 (1979).

[Wol2005] H. J. Wollersheim et al. *Rare ISotope INvestigation at GSI (RISING) using Gamma-ray Spectroscopy at Relativistic Energies*. Nucl. Instr. and Meth. **A537**, 637–657 (2005).